
CASSEM

Document Name: Task 1.4: Identification of materials properties
(direct/inverse)
FP6-NMP3-CT-2005-013517 "CASSEM"

Document Date: **01/09/06**

Document Owner: **CASSEM CONSORTIUM**

Document Author/s: RTU, CRPHT, IST, ULB

Document prepared by: **RTU**

Task / Deliverable Number: **Tasks 1.4 / D3**

Version: **2**

Status: **Final**

Document Reference Number: **D3**

© COPYRIGHT 2005 CASSEM Consortium

This document may not be copied, reproduced, or modified in whole or in part for any purpose without written permission from the CASSEM Consortium. In addition, to such written permission to copy, acknowledgement of the authors of the document and all applicable portions of the copyright notice must be clearly referenced.

All rights reserved

CASSEM

DELIVERABLE 3

Doc. No. D3	Rev. No. 2	Final	Date	01.09.2006
Title: Task 1.4: Identification of materials properties (direct/inverse)				
Issued by: RTU, CRPHT, IST, ULB				
<p>Summary:</p> <p>Different identification techniques are developed, tested and applied to characterise advanced composite material properties: elastic, plastic, hysteretic, viscoelastic, piezoelectric and dielectric. These techniques are based on indentation and vibration tests, and computation of effective properties on a so-called representative volume element. Future research needs are discussed in addition.</p>				
Authors: RTU (4.2), CRPHT (2), IST (4.1), ULB (3)				
Verified by: RTU			Approved by: Consortium	
Key words: identification technique, advanced composite, material properties, elastic, plastic, hysteretic, viscoelastic, piezoelectric, dielectric.				
			Total number of pages, incl. figures, tables, appendices	109

CASSEM

DOCUMENT REVISION RECORD

Report title:

Task 1.4: Identification of materials properties (direct/inverse)

Issued by: RTU, CRPHT, IST, ULB

Doc. No. D3

Rev. No.	Date	Nature of revision	No. of pages
1	01/09/2006	Draft 1	109
2	29/09/2006	Final	109
3			
4			

Document revision record, 1st issue 2006

Contents

1.	Introduction	6
2.	Identification of mechanical material properties	7
2.1	Parameter identification from uniaxial testing	
	using numerical optimisation	7
	2.1.1 Introduction	7
	2.1.2 Error function	8
	2.1.3 Calculation of the gradient	9
	2.1.4 Implementation	12
	2.1.5 Assessment of the method	13
	2.1.6 Further steps	13
2.2	Material parameter identification from tensile testing	
	using neural networks	13
	2.2.1 Implementation	13
	2.2.2 Results	17
	2.2.3 Identification with the optimisation method	20
	2.2.4 Identification with the classical response surface analysis	24
	2.2.5 Conclusions	24
2.3	Material parameter identification for rigid indentation	
	using an optimisation method in finite element modelling	
	with co-rotational finite strain	25
	2.3.1 The material behaviour	25
	2.3.2 Stress update equations	26
	2.3.3 The equations for gradient calculation	27
	2.3.4 Determination of the Gradients of the kinematic variables	30
	2.3.5 Procedure for the gradient calculation	33
	2.3.6 Numerical example	35
	2.3.7 Annex	37
2.4	Implementation of rigid contact	40
	2.4.1 Contact modelling	41
	2.4.2 Spherical/cylindrical node-to-surface contact	42
	2.4.3 Conical/wedge-like node-to-surface contact	43
	2.4.4 Spherical/cylindrical surface-to-surface contact	44
	2.4.5 Implementation of adaptive descent	46
	2.4.6 Contact definition	46
	2.4.7 Adaptive descent	47
	2.4.8 Further changes	48
	2.4.9 Conclusions	48
2.5	Nanoindentation test	48
	2.5.1 Measurements	49
	2.5.2 Dynamic measurements	50
	2.5.3 Specifications	51
	2.5.4 Channels	51
	2.5.5 Formulas	52

3.	Identification of electro-mechanical material properties	53
3.1	Principle of the method	53
3.2	Mixing rules for piezo fibres used in d_{31} mode	54
3.3	Evolution of the homogenized properties as a function of the volume fraction of fibres	59
3.4	Homogenized properties of commercial MFC actuators	61
3.5	Validation on an experimental setup	64
4.	Inverse identification technique	65
4.1	Direct optimisation technique	65
4.1.1	Numerical model	66
4.1.2	Gradient based optimisation	71
4.1.3	Piezo/elastic applications	73
4.1.3.1	Simulations	73
4.1.3.2	Experimental verification	75
4.1.4	Viscoelastic applications	77
4.1.5	Conclusions	79
4.2	Non-direct optimisation technique	81
4.2.1	Identification procedure	81
4.2.2	Theoretical background	82
4.2.2.1	Experimental setup	82
4.2.2.2	Numerical model	83
4.2.2.3	Material identification procedure	86
4.2.3	Identification of material properties	89
4.2.3.1	Identification of isotropic material properties	89
4.2.3.2	Identification of orthotropic material properties	91
4.2.3.3	Identification of viscoelastic material properties	96
4.2.4	Conclusions	102
5.	General conclusions	103
	References	105

1 Introduction

Composites like investigated in the project are seen as an area of high growth in the world, due to their intrinsic benefits and critical role in different industrial sectors such as aerospace, land transport, marine and construction. Unfortunately, the material data provided by the manufacturers do not contain all necessary information to predict the behaviour of advanced composite structures with an active control using different analysis tools. This is a reason why the present task is focused on the development and validation of different identification technique to characterise advanced composite material properties: elastic, plastic, hysteretic, viscoelastic, piezoelectric and dielectric.

An identification technique and scientific and technical data developed in the project are intended for the research laboratories, composite fabrication industry and end-use markets like aerospace, land transport, marine and construction industries. Results of the project will contribute to more intensive application of advanced composites with an active control in different constructions leading by this way to reduction of their weight, noise and vibrations as well as increasing their life.

2 Identification of mechanical material properties

An identification procedure is developed to characterise mechanical material properties from indentation testing.

2.1 Parameter identification from uniaxial testing using numerical optimisation

As an intermediate stage for determining material parameters through indentation testing, the methods for parameter identification are developed for the case of uniaxial testing in tension and compression. In this case, the calculation of the stress-strain curves can be performed analytically, thus eliminating more time-consuming finite element calculations during this stage. In this report, parameter identification using a method based on numerical optimisation is treated.

2.1.1 Introduction

The material law under consideration is isotropic hypoelastic associative plasticity with non-linear kinematic and non-linear isotropic hardening with additive split of the strain tensor. The elastic part of the constitutive equation is governed by two material parameters: (i) the Young's modulus E and the (ii) the Poisson's ratio ν . The plastic part is governed by five material parameters: (i) the yield stress σ_0 , (ii) the isotropic hardening modulus R , (iii) the isotropic hardening exponent b , (iv) the kinematic hardening modulus H_{kin} and (v) the kinematic hardening exponent H_{nl} . The state variables are the stress σ_x , the back-stress α_x , the plastic strain $\epsilon_{p,x}$ and the plastic arc length s . The yield condition for the uniaxial case is

$$f = |\sigma_x - \alpha_x| - \sigma_0 - \frac{R}{b} [1 - \exp(-bs)] \quad (2.1)$$

As we are considering a displacement-driven formulation, the independent variable is the total strain $\epsilon_{t,x}$.

In case of elastic deformation, the state variables are updated as

$$\sigma_x^I = \sigma_x^0 + E(\epsilon_{t,x}^I - \epsilon_{t,x}^0) \quad (2.2)$$

$$\alpha_x^I = \alpha_x^0 \quad (2.3)$$

$$s^I = s^0 \quad (2.4)$$

$$\epsilon_{p,x}^I = \epsilon_{p,x}^0 \quad (2.5)$$

In case of plastic deformation, an Euler-backward time integration scheme is used. The update of the state variables is performed as

$$\alpha_x^I = \alpha_x^0 \exp\left(-\sqrt{\frac{3}{2}} H_{nl}(\Delta\lambda)\right) + \frac{H_{kin}}{H_{nl}} \left[1 - \exp\left(-\sqrt{\frac{3}{2}} H_{nl}(\Delta\lambda)\right)\right] N_x \quad (2.6)$$

$$s^I = s^0 + \Delta\lambda \quad (2.7)$$

$$\varepsilon_{p,x}^I = \varepsilon_{p,x}^0 + \sqrt{\frac{3}{2}} \Delta\lambda N_x \quad (2.8)$$

The normal vector N is defined as

$$N_x = \frac{\sqrt{\frac{2}{3}} \frac{\sigma_x^I - \alpha_x^I}{|\sigma_x^I - \alpha_x^I|}}{\sqrt{\frac{2}{3}} \frac{\sigma_x^{tr} - \frac{3}{2} x^0 \exp\left(-\sqrt{\frac{3}{2}} H_{nl}(\Delta\lambda)\right)}{\left|\sigma_x^{tr} - \frac{3}{2} x^0 \exp\left(-\sqrt{\frac{3}{2}} H_{nl}(\Delta\lambda)\right)\right|}} \quad (2.9)$$

and the trial stress σ_x^{tr} is defined as

$$\sigma_x^{tr} = \sigma_x^0 + E(\varepsilon_{t,x}^I - \varepsilon_{t,x}^0) \quad (2.10)$$

The consistency parameter $\Delta\lambda$ is calculated with a Newton-Raphson scheme using

$$f = \left| \sigma_x^{tr} - \frac{3}{2} x^0 \exp\left(-\sqrt{\frac{3}{2}} H_{nl}(\Delta\lambda)\right) \right| - E\Delta\lambda - \sqrt{\frac{3}{2}} \frac{H_{kin}}{H_{nl}} \left[1 - \exp\left(-\sqrt{\frac{3}{2}} H_{nl}(\Delta\lambda)\right) \right] - \sigma_0 - \frac{R}{b} \left[1 - \exp(-b(\varepsilon_{p,x}^0 + \Delta\lambda)) \right] = 0 \quad (2.11)$$

and

$$\frac{df}{d\Delta\lambda} = \frac{9}{4} N_x \alpha_x^0 H_{nl} \exp\left(-\sqrt{\frac{3}{2}} H_{nl}(\Delta\lambda)\right) - E - \frac{3}{2} H_{kin} \exp\left(-\sqrt{\frac{3}{2}} H_{nl}(\Delta\lambda)\right) - R \exp(-b(\varepsilon_{p,x}^0 + \Delta\lambda)) \quad (2.12)$$

2.1.2 Error function

An error function is defined as the sum of squared differences between experimental and computed data. Assuming that the experiment is displacement driven, the independent variable is the total strain. The error function Ξ is based on the stress.

$$\Xi = \sum_{k=1}^N \left[\bar{\sigma}(\varepsilon_t^k) - \sigma(\kappa_i, q(\kappa_i, \varepsilon_t^k), \varepsilon_t^k) \right]^2 \quad (2.13)$$

with the state variables

$$q = (\sigma_x, \alpha_x, \varepsilon_{p,x}, s) \quad (2.14)$$

and the material parameters

$$\kappa = (\sigma_0, R, b, H_{kin}, H_{nl}, E) \quad (2.15)$$

The gradient of the error function is given as

$$\frac{d\Xi}{d\kappa_i} = -2 \sum_{k=1}^N \left[\bar{\sigma}(\epsilon_t^k) - \sigma(\kappa_i, q(\kappa_i, \epsilon_t^k), \epsilon_t^k) \right] \frac{d\sigma(\kappa_i, q(\kappa_i, \epsilon_t^k), \epsilon_t^k)}{d\kappa_i} \quad (2.16)$$

Using the Gauss-Newton optimisation method, the Hessian matrix is required. Differentiation of Eq. (2.16) gives

$$\begin{aligned} \frac{d^2\Xi}{d\kappa_i d\kappa_j} = & -2 \sum_{k=1}^N \left[\bar{\sigma}(\epsilon_t^k) - \sigma(\kappa_i, q(\kappa_i, \epsilon_t^k), \epsilon_t^k) \right] \frac{d^2\sigma(\kappa_i, q(\kappa_i, \epsilon_t^k), \epsilon_t^k)}{d\kappa_i d\kappa_j} \\ & + 2 \sum_{k=1}^N \frac{d\sigma(\kappa_i, q(\kappa_i, \epsilon_t^k), \epsilon_t^k)}{d\kappa_i} \frac{d\sigma(\kappa_i, q(\kappa_i, \epsilon_t^k), \epsilon_t^k)}{d\kappa_j} \end{aligned} \quad (2.17)$$

This matrix is not necessarily positive definite. Neglecting the first term to avoid the perturbations caused by the direct approximation error of the stress, the Hessian is replaced by the matrix

$$\tilde{H}_{ij} = 2 \sum_{k=1}^N \frac{d\sigma(\kappa_i, q(\kappa_i, \epsilon_t^k), \epsilon_t^k)}{d\kappa_i} \frac{d\sigma(\kappa_i, q(\kappa_i, \epsilon_t^k), \epsilon_t^k)}{d\kappa_j} \quad (2.18)$$

From equations it can be seen that the gradient has to be evaluated at each available data point, i.e. for each value of total strain.

2.1.3 Calculation of the gradient

Plastic loading

According to [2.1-2.3], four constitutive equations are formed inserting Eq. (2.7) into Eqs. (2.6 and 2.8) together with Eq. (2.1):

$$G_1 = \sigma_x^l - \sigma_x^0 - E\epsilon_{t,x}^l + E\epsilon_{t,x}^0 + E\epsilon_{p,x}^l = 0 \quad (2.19)$$

$$G_2 = \epsilon_{p,x}^l - \epsilon_{p,x}^0 - \sqrt{\frac{3}{2}}(s^l - s^0)N_x = 0 \quad (2.20)$$

$$G_3 = \alpha_x^l - \alpha_x^0 \exp\left(-\sqrt{\frac{3}{2}}H_{nl}(s^l - s^0)\right) - \frac{H_{kin}}{H_{nl}} \left[1 - \exp\left(-\sqrt{\frac{3}{2}}H_{nl}(s^l - s^0)\right) \right] \quad (2.21)$$

$$G_4 = |\sigma_x^l - \alpha_x^l| - \sigma_0 - \frac{R}{b} [1 - \exp(-bs^l)] = 0 \quad (2.22)$$

The total derivatives of the constitutive equations is

$$\frac{dG_i}{d\kappa_j} = \frac{\partial G_i}{\partial \kappa_j} + \frac{\partial G_i}{\partial q_k^l} \frac{dq_k^l}{d\kappa_j} + \frac{\partial G_i}{\partial q_k^0} \frac{dq_k^0}{d\kappa_j} \quad (2.23)$$

As the constitutive equations G_i are by definition always zero, the total derivatives of G are also zero.

$$\frac{\partial G_i}{\partial \kappa_j} + \frac{\partial G_i}{\partial q_k^l} \frac{dq_k^l}{d\kappa_j} + \frac{\partial G_i}{\partial q_k^0} \frac{dq_k^0}{d\kappa_j} = 0 \quad (2.24)$$

Transformation of Eq. (2.24) yields a recursive equation for calculating the total derivative of the current state variables with respect to the material parameters

$$\frac{dq_r^l}{d\kappa_j} = - \left(\frac{\partial G_r}{\partial q_i^l} \right)^{-1} \left(\frac{\partial G_i}{\partial \kappa_j} + \frac{\partial G_i}{\partial q_k^0} \frac{dq_k^0}{d\kappa_j} \right) \quad (2.25)$$

The total derivative of the stress with respect to the material parameters is the first row of the matrix obtained from Eq. (2.25).

To solve Eq. (2.25), the partial derivatives of the constitutive equations have to be calculated. However, most elements are zero. For the partial derivative of the constitutive equations with respect to the current state variables, the non-zero elements are

$$\frac{\partial G_1}{\partial \sigma_x^l} = 1 \quad (2.26)$$

$$\frac{\partial G_1}{\partial \varepsilon_{p,x}^l} = E \quad (2.27)$$

$$\frac{\partial G_2}{\partial \varepsilon_{p,x}^l} = 1 \quad (2.28)$$

$$\frac{\partial G_2}{\partial s^l} = -\sqrt{\frac{3}{2}} N_x \quad (2.29)$$

$$\frac{\partial G_3}{\partial \alpha_x^l} = 1 \quad (2.30)$$

$$\frac{\partial G_3}{\partial s^l} = \left(\alpha_x^0 - \frac{H_{kin}}{H_{nl}} N_x \right) \sqrt{\frac{3}{2}} H_{nl} \exp \left(-\sqrt{\frac{3}{2}} H_{nl} (s^l - s^0) \right) \quad (2.31)$$

$$\frac{\partial G_4}{\partial \sigma_x^l} = \sqrt{\frac{3}{2}} N_x \quad (2.32)$$

$$\frac{\partial G_4}{\partial \alpha_x^l} = -\frac{3}{2} \sqrt{\frac{3}{2}} N_x \quad (2.33)$$

$$\frac{\partial G_4}{\partial s^l} = -R \exp(-bs^l) \quad (2.34)$$

For the partial derivative of the constitutive equations with respect to the state variables at the beginning of the increment, the non-zero elements are

$$\frac{\partial G_1}{\partial \sigma_x^0} = -1 \quad (2.35)$$

$$\frac{\partial G_2}{\partial \varepsilon_{p,x}^0} = -1 \quad (2.36)$$

$$\frac{\partial G_2}{\partial s^0} = \sqrt{\frac{3}{2}} N_x \quad (2.37)$$

$$\frac{\partial G_3}{\partial \alpha_x^0} = -\exp\left(-\sqrt{\frac{3}{2}} H_{nl} (s^1 - s^0)\right) \quad (2.38)$$

$$\frac{\partial G_3}{\partial s^0} = \left(\alpha_x^0 - \frac{H_{kin}}{H_{nl}} N_x\right) \sqrt{\frac{3}{2}} H_{nl} \exp\left(-\sqrt{\frac{3}{2}} H_{nl} (s^1 - s^0)\right) \quad (2.39)$$

For the partial derivative of the constitutive equations with respect to the material parameters, the non-zero elements are

$$\frac{\partial G_1}{\partial E} = -\varepsilon_{t,x}^1 + \varepsilon_{t,x}^0 + \varepsilon_{p,x}^0 \quad (2.40)$$

$$\frac{\partial G_3}{\partial H_{kin}} = -\frac{N_x}{H_{nl}} \left[1 - \exp\left(-\sqrt{\frac{3}{2}} H_{nl} (s^1 - s^0)\right)\right] \quad (2.41)$$

$$\begin{aligned} \frac{\partial G_3}{\partial H_{nl}} &= \sqrt{\frac{3}{2}} (s^1 - s^0) \alpha_x^0 \exp\left(-\sqrt{\frac{3}{2}} H_{nl} (s^1 - s^0)\right) \\ &+ \frac{H_{kin} N_x}{H_{nl}^2} \left[1 - \exp\left(-\sqrt{\frac{3}{2}} H_{nl} (s^1 - s^0)\right)\right] \left(1 + \sqrt{\frac{3}{2}} H_{nl} (s^1 - s^0)\right) \end{aligned} \quad (2.42)$$

$$\frac{\partial G_4}{\partial \sigma_0} = -1 \quad (2.43)$$

$$\frac{\partial G_4}{\partial R} = \frac{\exp(-bs^1) - 1}{b} \quad (2.44)$$

$$\frac{\partial G_4}{\partial b} = \frac{R}{b^2} \left[1 - (1 + bs^1) \exp(-bs^1)\right] \quad (2.45)$$

Elastic loading

Eqs. (2.2-2.5) are transformed to give the four constitutive equations

$$\sigma_x^1 - \sigma_x^0 - E\varepsilon_{t,x}^1 + E\varepsilon_{t,x}^0 = 0 \quad (2.46)$$

$$\alpha_x^1 - \alpha_x^0 = 0 \quad (2.47)$$

$$s^1 - s^0 = 0 \quad (2.48)$$

$$\varepsilon_{p,x}^1 - \varepsilon_{p,x}^0 = 0 \quad (2.49)$$

The partial derivative of the constitutive equations with respect to the current state variables is given as

$$\frac{\partial G_i}{\partial q_j^I} = I_{4 \times 4} \quad (2.50)$$

The partial derivative of the constitutive equations with respect to the state variables at the beginning of the increment is given as

$$\frac{\partial G_i}{\partial q_j^0} = -I_{4 \times 4} \quad (2.51)$$

All partial derivatives of the constitutive equations with respect to the material parameters are zero, except

$$\frac{\partial G_i}{\partial E} = -(\varepsilon_{t,x}^I - \varepsilon_{t,x}^0) \quad (2.52)$$

Eqs. (2.50 and 2.51), inserted into Eq. (2.25), give the recursive update for the total derivatives for elastic loading as

$$\frac{dq_i^I}{d\kappa_j} = \frac{dq_i^0}{d\kappa_j} - \frac{\partial G_i}{\partial \kappa_j} \quad (2.53)$$

2.1.4 Implementation

A subroutine was written to calculate the elasto-plastic stress-strain curves in an incremental way. This function calculates the error function, the gradient vector and the regularized Hessian matrix after each increment according to Eqs. (2.13, 2.16 and 2.18) respectively. The gradient and the Hessian are stored internally, and can be retrieved by functions required by the optimisation routine to provide the gradient and the Hessian, respectively. The optimisation is performed using the routine DBCOAH from the IMSL mathematical FORTRAN library. This routine performs an optimisation with bounded parameters using the function values, the gradient vector and the Hessian matrix [2.4]. For a better convergence the parameter vector κ in Eq. (2.15) is scaled with the scaling vector

$$\kappa = (\sigma_0, R, b, H_{kin}, H_{nl}, E) \quad (2.54)$$

For assessing the convergence properties, optimisations have been performed with the IMSL routines DBCONF, which requires only function values and calculates the gradient by a finite difference scheme, and DBCONG, which requires function values and gradient values [2.4].

These three IMSL optimisation routines are quasi-Newton or modified Newton methods. Boundary constraints are enforced using an active set strategy. The

iterative solutions are computed via an unspecified line-search algorithm, probably the Armijo line-search algorithm.

2.1.5 Assessment of the method

The implemented routine was tested performing a re-identification of material parameters. For a given set of material parameters, a stress-strain curve with tension and compression is calculated and serves as artificial experimental input data. The optimisation-based identification routine is then run on this set of experimental data with a different initial guess for the material parameters. The re-identification is successful if the input material parameters of the experimental data are recovered through the optimisation process.

Optimisation schemes relying on error function values only have not been considered because these methods have bad convergence characteristics. It was found that the recursive calculation of the gradient during the calculation of the stress-strain curves in the optimisation process saves a considerable amount of computing effort compared to a gradient calculated by a finite difference scheme. For a finite difference gradient, the calculation of the gradient requires a number of simulations equal to the number of material parameters. In addition to that, a finite difference gradient is less accurate than an analytical or semi-analytical gradient. It was found that an optimisation scheme relying only on the gradient is converging slowly. The best convergence rates were achieved by using a modified Hessian as stated in Eq. (2.18).

2.1.6 Further steps

In a next step, the optimisation-based routine is adapted in such a way that instead of analytical calculation of the stress-strain curves, a finite element calculation using the in-house finite element code is performed. Some changes in the calculation of the derivatives have to be implemented [2.1], because of an implicit influence of the material parameters on the total strains in the finite element method.

2.2 Material parameter identification from tensile testing using neural networks

According to Task 1.4 of the project CASSEM, a neural network-based parameter identification routine has been developed for a uniaxial tensile/compressive test. In the material model used, isotropic hypoelasticity is represented using two parameters, the Young's modulus and the Poisson's ratio. Plasticity incorporates nonlinear isotropic and nonlinear kinematic hardening, involving 5 parameters, the yield stress, the linear parameter for both kinematic and isotropic hardening, c and R , respectively, and the nonlinear parameter for both kinematic and isotropic hardening, b and β , respectively.

2.2.1 Implementation

It should be noted that the Poisson's ratio is not to be identified, because use is made of the stress and the axial specimen displacement only for input in the identification routine. This limits the number of free parameters to six.

$$E, \sigma^{y,0}, R, \beta, c, b \quad (2.55)$$

Based on [2.5], several neural networks have been developed for identifying the material parameters from the stress-strain curves. The implementation is based on MATLAB [2.6]. The networks were trained using a training set comprising 100 different stress strain curves. The parameter sets have been chosen in such a way to obtain a space-filling Latin Hypercube design according to Audze/Eglais [2.7]. The stress-strain curves have been calculated using a numerical implementation of the uniaxial test [2.8,2.9], with a loading cycle consisting of 10 increments and an unloading cycle of 20 increments. The stress-strain curve was modelled as a displacement controlled experiment, with nominal strain amplitude of +/- 2%. As a Bayesian rule-learning scheme was used for calculating the weights and offsets of the neural networks, no training or validation sets were required. However, a validation set of 20 stress-strain curves, also chosen from a space-filling hypercube design, with the parameter range reduced by 10 percent, was used to check the quality of the neural network approximation.

From the experiments, the axial stress and the total strain are used:

$$\sigma_i \text{ and } \varepsilon_i, \quad i = 1, 2, \dots, 30 \quad (2.56)$$

The networks are feed-forward networks made up of one input layer, one hidden layer with the logistics transfer function and an output layer with a proportional transfer function. The following networks were used

Network 1

Used for obtaining the Young's modulus. The network has a 10-4-1 topology.

Inputs

$$x_i^l = 2 \frac{\sigma_{i+10}}{\sigma_{10} - \sigma_{30}}, \quad i = 1, \dots, 10 \quad (2.57)$$

Outputs

$$y_l^l = \frac{\sigma_{10} - \sigma_{20}}{E(\varepsilon_{10} - \varepsilon_{30})} \quad (2.58)$$

After calculation of the Young's modulus, the plastic strain can be calculated as

$$\varepsilon_i^p = \varepsilon_i - \frac{\sigma_i}{E}, \quad i = 1, \dots, 30 \quad (2.59)$$

The equivalent plastic strain is calculated as

$$s_i = \sum_{j=1}^i |\varepsilon_i^p - \varepsilon_{i-1}^p|, \quad i = 1, \dots, 30, \quad \text{with } \varepsilon_0^p = 0 \quad (2.60)$$

From the plastic strains computed from Eq. (2.5), additional ordinates are calculated. For the ascending, loading branch, the are

$$\bar{\varepsilon}_i^{p,l} = \frac{i}{10} \varepsilon_{10}^p, \quad i = 1, \dots, 10 \quad (2.61)$$

whereas for the descending, unloading branch, they are

$$\bar{\varepsilon}_i^{p,u} = \varepsilon_{10}^p + \frac{i}{20} (\varepsilon_{30}^p - \varepsilon_{10}^p), \quad i = 1, \dots, 20 \quad (2.62)$$

For these values, the corresponding stress values are computed, for each segment separately, by linear interpolation, which gives the values

$$\bar{\sigma}_i, \quad i = 1, \dots, 30 \quad (2.63)$$

Network 2

Used for obtaining the yield stress. The network has a 11-5-1 topology.

Inputs

$$x_1^2 = \frac{\sigma_{10} - \sigma_{20}}{E(\varepsilon_{10} - \varepsilon_{30})} \quad (2.64)$$

$$x_i^2 = 2 \frac{\sigma_{i-1}}{\sigma_{10} - \sigma_{30}}, \quad i = 2, \dots, 11 \quad (2.65)$$

Outputs

$$y_1^2 = \frac{\sigma^{y,0}}{\sigma_{10} - \sigma_{20}} \quad (2.66)$$

Network 3

Used for obtaining the yield stress at the end of the tensile and compressive loading segment. The network has a 44-4-2 topology. For the training set, the following values are calculated:

$$k^1 = \sigma^{y,0} + \frac{R}{\beta} [1 - \exp(-\beta s_{10})] \quad (2.67)$$

$$k^2 = \sigma^{y,0} + \frac{R}{\beta} [1 - \exp(-\beta s_{30})] \quad (2.68)$$

Inputs

$$x_1^3 = \frac{\sigma_{10} - \sigma_{20}}{E(\varepsilon_{10} - \varepsilon_{30})} \quad (2.69)$$

$$x_2^3 = \frac{\sigma^{y,0}}{\sigma_{10} - \sigma_{20}} \quad (2.70)$$

$$x_i^3 = 2 \frac{\sigma_{i+7}}{\sigma_{10} - \sigma_{30}}, \quad i = 3, \dots, 23 \quad (2.71)$$

$$x_i^3 = \frac{\varepsilon_{i-23}^p}{\varepsilon_{10}}, \quad i = 24, \dots, 44 \quad (2.72)$$

Outputs

$$y_i^3 = \frac{k^i}{\sigma_{10} - \sigma_{30}}, \quad i = 1, 2 \quad (2.73)$$

Network 4

Used for obtaining the kinematic hardening parameters. The network has a 50-8-2 topology.

Inputs

$$x_1^4 = \frac{\sigma^{y,0}}{k^2} \quad (2.74)$$

$$x_2^4 = \frac{\sigma_{10} - \sigma_{30}}{\sigma_{30}} \quad (2.75)$$

$$x_3^4 = \frac{k^1}{k^2} \quad (2.76)$$

$$x_4^4 = \frac{\sigma_{30} + \sigma^{y,0}}{\sigma_{30}} \quad (2.77)$$

$$x_i^4 = \frac{\bar{\sigma}_{i-4} + \sigma^{y,0}}{\bar{\sigma}_{30} + \sigma^{y,0}}, \quad i = 5, \dots, 21 \quad (2.78)$$

$$x_i^4 = \frac{\bar{\sigma}_{i-21}}{\bar{\sigma}_{30}}, \quad i = 22, \dots, 50 \quad (2.79)$$

Outputs

$$y_1^4 = \frac{\left(\frac{3}{2} b - (c-1) \xi^2 \right)}{\sigma_{30} \varepsilon_{30}^p} \quad (2.80)$$

$$y_2^4 = -\frac{2}{3} \frac{\xi^2}{b\varepsilon_{10}^p} \quad (2.81)$$

The values of ξ are obtained through

$$\xi^2 = k^2 + \sigma_{30} \quad (2.82)$$

Network 5

Used for obtaining the isotropic hardening parameters. The network has a 44-8-2 topology.

Inputs

$$\dot{g} = \frac{(\Delta x_i^{AP} - gn_i) N^A \dot{x}_i^A}{\sqrt{\Delta x_m^{AP} n_m - \Delta x_m^{AP} \Delta x_m^{AP} + R^2}} - g \frac{\Delta x_i^{AP} \dot{n}_i}{\sqrt{\Delta x_m^{AP} n_m - \Delta x_m^{AP} \Delta x_m^{AP} + R^2}} \quad (2.83)$$

$$f_i^{C,A} = -K^C \sum_{B=1}^{N_{Nodes}} \int_{\partial\Omega} N^B gn_i d\partial\Omega \quad (2.84)$$

$$x_{39}^5 = \frac{\sigma^{y,0}}{\sigma_{10}} \quad (2.85)$$

$$x_{40}^5 = \frac{\sigma_{10} - \sigma^{y,0}}{\sigma_{10}} \quad (2.86)$$

$$x_{41}^5 = \frac{\varepsilon_{10}^p}{\varepsilon_{10}} \quad (2.87)$$

$$x_{42}^5 = \frac{k^l}{k^2} \quad (2.88)$$

$$x_{43}^5 = \frac{\sigma^{y,0}}{k^2} \quad (2.89)$$

$$x_{44}^5 = \frac{\sigma_{10} - \sigma_{20}}{E(\varepsilon_{10} - \varepsilon_{30})} \quad (2.90)$$

Outputs

$$y_1^5 = l - \frac{k^l - \sigma^{y,0}}{Rs^l} \quad (2.91)$$

$$y_2^5 = \frac{(k^l - \sigma^{y,0})\beta}{R} \quad (2.92)$$

2.2.2 Results

The efficiency of the method has been assessed using artificial stress-strain curves, obtained by finite element modelling, where the material parameters, which are obviously known, are shown in Table 2.1. The parameters identified from

Table 2.1 Material parameters of the test case.

Parameter	Original
E (MPa)	209342.1
$\sigma^{y,0}$ (MPa)	479.7079
R (MPa)	7434.211
β (-)	257.3158
c (MPa)	14539.47
b (-)	82,05

the stress-strain curves can then be compared to the true material parameters. Stress-strain curves with random experimental noise levels with a magnitude between 0 and 10% of the maximum stress have been used.

In a first test, the raw 'experimental' stress-strain curves have been used. In a second test, stress-strain curves with 300 experimental points have been modelled, a background noise superposed and the 30 experimental points required extracted after digital filtering with the function

$$y_k = 0.0073x_k + 0.0147x_{k-1} + 0.0073x_{k-2} + 1.7433y_{k-1} - 0.7727y_{k-2} \quad (2.93)$$

Filtering has been performed in MATLAB using the `filtfilt` routine [2.6], which processes the data series back and forth in order to compensate the out-of-phase shift caused by filtering.

In a third test, the same 300-point curve has been smoothed using a neural network. In this case, to avoid severe curve rounding, the curve has been split in two parts: the loading branch and the unloading branch. Both parts were smoothed individually using a 1-2-1 feed-forward neural network with Bayesian rule training. The training set consists of the all the stress values of one part of the curve. This way, the stress-strain curve can be approximated with a neural network, and because of the low number of neurones in the hidden layer, a smooth curve is obtained. In fact, this method is equivalent to a least squares fit, with the difference that here, no analytical function is fitted.

In Table 2.2, the material parameters obtained by using the raw, 30-increment stress-strain curve for input in the 4-5-4-8-8 neural network shows that meaningful results are obtained until an error level of one percent whereas for higher error levels, all identified parameters, except the Young's modulus, become meaningless. It should be noted that even for the case of no background noise, an error in the parameters between 5 to 10 % prevails. The error on the hardening exponents is significant. In order to check the generalization properties of the

Table 2.2 Curve modelled by 30 increments, noise superposed, 4-5-4-8-8 hidden layer neurons in the five networks.

error	0	0.001	0.005	0.01	0.05	0.1
E (MPa)	219520	220380	222920	212600	204800	218910
$\sigma^{y,0}$ (MPa)	459.868	459.4575	460.9331	488.5333	274.8332	1431.7
R (MPa)	9854.3	9981.2	5764.1	4794.8	9899.4	188710
β (-)	277.4153	296.6475	256.928	185.1063	2.8968	-521.714
c (MPa)	16498	15974	18102	12360	-17976	23409
b (-)	93.2912	103.073	128.367	43.352	345.5176	130.9392

Table 2.3 Curve modelled by 30 increments, noise superposed, 3-4-3-7-7 hidden layer neurons in the five networks.

error	0	0.001	0.005	0.01	0.05	0.1
E (MPa)	214810	215460	216500	212820	196930	251230
$\sigma^{y,0}$ (MPa)	466.7376	466.7991	432.5546	505.9373	288.0023	1345.5
R (MPa)	655.5358	159.8378	47199	-2897	13466	183920
β (-)	220.9931	235.5878	184.3513	156.2908	16.4787	-335.123
c (MPa)	20227	20165	25470	13512	-8568	2062.2
b (-)	59.8718	63.4923	7.4092	144.9049	662.3312	3216,5

network, the same inputs and training sets have been used with network including one neuron less in the hidden layer. As the identified parameters, included in Table 2.3, are worsening, it can be concluded that the error in the 4-5-4-8-8 identification routine does not stem from overtraining.

In Tables 2.4 and 2.5, the results for the stress-strain curves obtained from the 300-increment modelling after filtering or neural network-based smoothing respectively, are shown. The young's modulus and the yield stress are identified within an acceptable tolerance, whereas large errors occur for the hardening parameters, including physical meaningless results, like a negative kinematic hardening exponent, for example. These errors are probably due to a curve round-off at the onset of yielding, which is distorting the yielding behaviour. From a noise level of 5 % upwards, the hardening parameters are partially wrong by more than one order of magnitude.

Table 2.4 Curve modelled by 300 increments, noise superposed, filtered and 30-valued curve extracted, 4-5-4-8-8 hidden layer neurons in the five networks.

error	0	0.001	0.005	0.01	0.05	0.1
E (MPa)	217490	217390	217610	217100	210230	228690
$\sigma^{y,0}$ (MPa)	456.2112	458.0104	453.1781	441.7448	405.4893	572.8224
R (MPa)	19111	19475	22204	36621	3130.1	-25987
β (-)	442.7967	457.5069	502.9022	574.1694	2.8407	418.5277
c (MPa)	17685	17356	18918	18884	57101	16983
b (-)	70.6507	67.4233	64.614	66.4393	51.2799	120.0666

Table 2.5 Curve modelled by 300 increments, noise superposed, approximated by neural networks and 30-valued curve extracted, 4-5-4-8-8 hidden layer neurons in the five networks.

error	0	0.001	0.005	0.01	0.05	0.1
E (MPa)	195010	195100	194960	196790	181650	208700
$\sigma^{y,0}$ (MPa)	452.8609	452.7742	454.3716	456.4402	395.9961	506.7566
R (MPa)	43951	44372	47371	42041	19275	-39446
β (-)	401.8689	406.6028	441.437	415.8203	62.7769	-764.592
c (MPa)	16767	16729	16724	16310	32398	11576
b (-)	-64.5736	-63.6695	-66.5788	-47.5965	-148.308	-125.392

2.2.3 Identification with the optimisation method

The same three sets of curves have been used for the optimisation-based identification procedure, developed in Task 1.4 of the CASSEM strep project. In addition to that, the full 300-point curve has been used as experimental input. This has been possible because of the small computational effort required in homogeneous, uniaxial testing.

In Table 2.6, which represents the results for the raw 30-increment stress-strain curve, it can be seen that the optimisation method can identify the material parameters to good accuracy. However, like in the case of the neural network-based method, from 5 % noise on, some parameters can not be identified any more, in the present case the isotropic hardening parameters. It should be noted that the optimisation-based results depend strongly on the initial guess. As can be seen from Table 2.7, a small change in the isotropic hardening exponent leads to totally erroneous isotropic hardening parameters from 0.5 % noise on.

Table 2.6 Curve modelled by 30 increments, noise superposed, optimisation method.

error	0	0.001	0.005	0.01	0.05	0.1	Init. Guess
E (MPa)	209342.1	209262.7	209849.1	209530.08	205351.9	208300	140000
$\sigma^{y,0}$ (MPa)	479.7089	481.0749	483.3192	481,48	485.4553	457.9189	300
R (MPa)	7433.536	6841.516	5779.32	7153.6305	1000	1728.287	15000
β (-)	257.3007	252.6262	232.7458	238.16245	10	10	170
c (MPa)	14539.47	14587.81	14507.81	14290.074	14268.9	16213.65	20000
b (-)	82.0526	82.38818	81.23375	80.307374	83.2639	103.0184	120

Table 2.7 Curve modelled by 30 increments, noise superposed, optimisation method, alternative initial guess.

error	0	0.001	0.005	0.01	0.05	0.1	Init. Guess
E (MPa)	209342	209262.7	206823.9	209530.08	205351.9	208300	140000
$\sigma^{y,0}$ (MPa)	479.7095	481.0747	491.7466	481.47586	485.4553	457.9189	300
R (MPa)	7433.195	6841.622	1000	7153.635	1000	1728.287	15000
β (-)	257.2933	252.6287	10	238.16254	10	10	150
c (MPa)	14539.47	14587.81	13676.87	14290.074	14268.9	16213.65	20000
b (-)	82.05258	82.38819	79.71863	80.307374	83.26394	103.0184	120

In Table 2.8, the results for the filtered 300-increment modelled stress-strain curve are shown. It can be seen that acceptable material parameters can be identified up to the maximum noise level, with the exception of the isotropic hardening parameters, which cannot be identified. The curve rounding through filtering also influences the yield stress by several percent. In the case of the neural-network-based curve smoothing, Table 2.9, the situation is similar, with the exception that better values are found for the isotropic hardening parameter, which at least have the right order of magnitude up to a noise level of 0.1 %.

In the case of the raw 300-increment stress-strain curve, Table 2.10, the identification works well up to a noise level of 0.1 %. The accuracy is poorer than for the raw 30-increment curve.

The stability of the optimisation procedure has been assessed choosing the true material parameters for starting point. In case the final results is the same as with a different starting point, the results can be considered as being stable. However, it can never be proved that the results of the optimisation techniques yield the global minimum of the cost function. These results, shown below in Tables 2.11-2.14,

Table 2.8 Curve modelled by 300 increments, noise superposed, filtered and 30-valued curve extracted, optimisation method.

error	0	0.001	0.005	0.01	0.05	0.1	Init. Guess
E (MPa)	197259.6	197245.2	197098.7	199556.2	197543.2	203206.5	140000
$\sigma^{y,0}$ (MPa)	493.0778	493.1265	493.4042	498.0603	494.4649	476.1349	300
R (MPa)	1000	1000	1000	1000	1000	21433.82	15000
β (-)	10	10	10	72.76645	10	541.2669	170
c (MPa)	13388.35	13386.16	13373.72	14086.71	13290.17	13212.15	20000
b (-)	82.8055	82.81586	82.71166	83.7042	83.4719	69.12956	120

Table 2.9 Curve modelled by 300 increments, noise superposed, approximated by neural networks and 30-valued curve extracted, optimisation method.

error	0	0.001	0.005	0.01	0.05	0.1	Init. Guess
E (MPa)	210829.2	210828.1	210644.5	210462.5	206364.7	210214.4	140000
$\sigma^{y,0}$ (MPa)	487.4359	487.1762	487.3413	489.8591	497.7288	463.2701	300
R (MPa)	4311.94	4457.037	4618.569	4001.735	1000	33992.89	15000
β (-)	202.2453	205.8652	216.387	208.722	46.57558	712.018	170
c (MPa)	14498.46	14490.67	14521.02	14390.09	14192.28	14003.88	20000
b (-)	81.85078	81.80757	82.10117	80.97356	83.91341	74.65325	120

Table 2.10 Curve modelled by 300 increments, noise superposed, optimisation method.

error	0	0.001	0.005	0.01	0.05	0.1	Init. Guess
E (MPa)	209342.1	209318.7	209103.6	208866,4	207107.2	212111.1	140000
$\sigma^{y,0}$ (MPa)	479.7081	479.4754	478.6347	480,31	492.3265	460.4975	300
R (MPa)	7434.076	7614.397	8492.271	8253,45	1000	26240.89	15000
β (-)	257.3124	260.4211	283.3801	289,59	10	532.6251	170
c (MPa)	14539.47	14527.1	14553.06	14439,89	13826.11	14086.52	20000
b (-)	82.05263	81.99116	82.28247	81,33	82.24547	73.69858	120

Table 2.11 Curve modelled by 30 increments, noise superposed, optimisation method, true parameters used as initial guess.

error	0	0.001	0.005	0.01	0.05	0.1	Init. Guess
E (MPa)	209342.1	209262.7	209849.1	209530.09	207492.5	208300	209342.1
$\sigma^{y,0}$ (MPa)	479.7078	481.0717	483.3178	481.47525	472.6208	457.9189	479.7079
R (MPa)	7434.226	6843.496	5780.147	7153.9938	4003.893	1728.287	7434.211
β (-)	257.3157	252.6723	232.7672	238.17016	92.41481	10	257.3158
c (MPa)	14539.47	14587.82	14507.81	14290.077	14019.41	16213.64	14539.47
b (-)	82.05263	82.38828	81.23381	80.307399	78.52341	103.0183	82.05263

Table 2.12 Curve modelled by 300 increments, noise superposed, filtered and 30-valued curve extracted, optimisation method, true parameters used as initial guess.

error	0	0.001	0.005	0.01	0.05	0.1	Init. Guess
E (MPa)	199963.9	199937	199798.9	199567.2	199983.5	203206.5	209342.1
$\sigma^{y,0}$ (MPa)	497.4085	497.5079	497.843	498.0632	495.0588	476.1361	479.7079
R (MPa)	1000	1000	1000	1000	1000	21432.45	7434.211
β (-)	65.8445	66.79462	67.96372	72.82441	32.86828	541.2485	257.3158
c (MPa)	14136.65	14141.81	14137.72	14086.7	13958.65	13212.15	14539.47
b (-)	83.99645	84.04661	83.98693	83.69878	85.23407	69.12954	82.05263

Table 2.13 Curve modelled by 300 increments, noise superposed, approximated by neural networks and 30-valued curve extracted, optimisation method, true parameters used as initial guess.

error	0	0.001	0.005	0.01	0.05	0.1	Init. Guess
E (MPa)	210829.2	210828.1	210644.5	210462.5	211581.7	210214.4	209342.1
$\sigma^{y,0}$ (MPa)	487.4355	487.1757	487.3406	489.8582	491.4365	463.2692	479.7079
R (MPa)	4312.127	4457.278	4619.004	4002.203	2776.412	33994.13	7434.211
β (-)	202.2511	205.8726	216.4003	208.7381	132.5076	712.0302	257.3158
c (MPa)	14498.46	14490.67	14521.02	14390.09	14246.7	14033.88	14539.47
b (-)	81.8508	81.80758	82.1012	80.9736	81.62338	74.65325	82.05263

Table 2.14 Curve modelled by 300 increments, noise superposed, optimisation method, true parameters used as initial guess.

error	0	0.001	0.005	0.01	0.05	0.1	Init. Guess
E (MPa)	209342.1	209318.7	209103.6	208866,4	210320.6	212111.3	209342.1
$\sigma^{y,0}$ (MPa)	479.7079	479.4754	478.6348	480,31	484.5413	460.5168	479.7079
R (MPa)	7434.214	7614.403	8492.173	8253,7	4661.126	26209.56	7434.211
β (-)	257.3158	260.4212	283.3778	289,59	177.0258	532.1767	257.3158
c (MPa)	14539.47	14527.1	14553.06	14439,89	14446.23	14086.35	14539.47
b (-)	82.05263	81.99117	82.28247	81,33	82.51345	73.69748	82.05263

suggest that the identification works in quite a stable way for the present starting values. It should nevertheless be kept in mind that initial values further away from the solution can lead to convergence to a different local minimum, yielding totally different and erroneous material parameters. This is the more likely the higher the experimental noise is.

2.2.4 Identification with the classical response surface analysis

This analysis uses the stress-curves from the six parameter and 100 experiments Audze-Eglais design of experiments. With the artificial 'experimental' curve, the cost function, i.e. the sum of the squares of the difference between 'experimental' and modelled curve, is calculated for the 100 available experiments. The multidimensional response surface is constructed using either a quadratic or a cubic approximation, involving 28 and 84 coefficients, respectively. On this curve, the minimum of the approximated cost function is determined by optimisation algorithm. This method is available in the EDAOPT program, obtained from the Riga Technical University (RTU), Latvia.

It was found that the parameter identification through this simple response surface analysis is poor. Results could be possibly improved by performing a multiple response surface analysis (MARS). This technique consists of iterative response surface analyses, where after each response surface analysis, a new set of curves is modelled after reducing the size of the parameter range, centred at the minimum found at the previous step. However, the computational effort is much higher than in the optimisation-based technique. Therefore, investigations using this method have been discontinued.

2.2.5 Conclusions

It was found that in the case of the filtered data series, the material parameters identified are significantly influenced filtering or smoothing. This has to do with the rounding of the curve at the onset of plasticity, where the curve is, in the case of this constitutive law, non-smooth. In the case of filtering, some low-frequency oscillations can be introduced, which also influence the results. This is the reason why the results of this method are worse than those of the neural network-based

smoothing, where no such oscillations are introduced. It has to be concluded that in the present case, with a non-smooth constitutive law, filtering and smoothing is not suitable for material parameter identification.

From the material parameter identification by the numerical optimisation method and the neural network-based method, it can be concluded that for small background noise levels, both methods tend to give acceptable results. The Young's modulus and the yield stress are identified with good accuracy. However, it should be noted that these parameters can be extracted graphically from the stress-strain curve. For high levels of noise, the hardening parameters get more and more influenced. The optimisation method has the advantage that at very small levels of noise, the accuracy is very high, whereas with the neural network-based method, significant errors can occur even for small noise magnitudes. This is the reason why the optimisation method will be used throughout this project for parameter identification through nano-indentation testing.

2.3 Material parameter identification for rigid indentation using an optimisation method in finite element modelling with co-rotational finite strain

After the development of a program for material parameter identification from uniaxial tensile testing based on using an optimisation method with the gradient calculated from a semi-analytical solution of the elastoplastic tensile test [2.10], the same method is implemented using the in-house finite element code for solving general multiaxial load cases. This is required for the CASSEM project, as indentation testing produces multiaxial stress states. The gradient is calculated during the incremental solution of the boundary value problem through finite element modelling. The case of finite strains was included in the program by using a co-rotational formulation [2.11]. The material law in question is isotropic hypoelasticity with isotropic plasticity and non-linear isotropic and kinematic hardening [2.12].

2.3.1 The material behaviour

Isotropic J2-flow theory is used with the yield function f

$$f = \sqrt{\xi_{ij}\xi_{ij}} - K^y = \|\xi\| - K^y = 0 \quad (2.94)$$

where σ^y is the yield stress and ξ is defined through the stress deviator S and the back-stress α as

$$\xi_{ij} = S_{ij} - \alpha_{ij} \quad (2.95)$$

The stress deviator S is defined using the Cauchy stress σ_{ij} as

$$S_{ij} = \sigma_{ij} - \frac{\sigma_{kk}}{3}\delta_{ij} = P_{ijkl}\sigma_{kl} \quad (2.96)$$

using the projection operator P

$$P_{ijkl} = \frac{1}{2}(\delta_{ik}\delta_{jl} + \delta_{il}\delta_{jk}) - \frac{1}{3}\delta_{ij}\delta_{kl} = I_{ijkl} - \frac{1}{3}\delta_{ij}\delta_{kl} \quad (2.97)$$

The back-stress is a deviatoric quantity, i.e.

$$P_{ijkl}\alpha_{kl} = \alpha_{ij} \quad (2.98)$$

Isotropic hardening is given as

$$K^y = \sqrt{\frac{2}{3}} \left(\sigma^{y,0} + \frac{R}{\beta} \exp(-\beta s) \right) \quad (2.99)$$

where s is the plastic arc length. Kinematic hardening is treated using the Armstrong-Frederick law

$$\dot{\alpha}_{ij} = H_{kin} \dot{\epsilon}_{ij}^p - \sqrt{\frac{3}{2}} H_{nl} \dot{s} \alpha_{ij} \quad (2.100)$$

The hypoelastic material behaviour is described using Hooke's law, with the Lamé constants G and λ

$$\sigma_{ij} = (2GI_{ijkl} + \lambda\delta_{ij}\delta_{kl})\epsilon_{kl}^{el} = C_{ijkl}\epsilon_{kl}^{el} \quad (2.101)$$

2.3.2 Stress update equations

The state variables at the beginning of an increment are characterized by a superscript '0', whereas those at the end of the increment are characterized by a superscript '1'. The mid-step configuration is characterized by a superscript '1/2'. In the rotation-neutralized coordinate frame, the update of the plastic arc length, stress and plastic strain is performed using:

$$s^1 = s^0 + \sqrt{\frac{2}{3}} \Delta g \quad (2.102)$$

$$\hat{\sigma}_{ij}^1 = \hat{\sigma}_{ij}^0 + C_{ijkl} \Delta \hat{\epsilon}_{kl}^{1/2} - 2G \Delta g \hat{N}_{ij}^1 \quad (2.103)$$

$$\hat{\epsilon}_{p,ij}^1 = \hat{\epsilon}_{p,ij}^0 + \Delta g \hat{N}_{ij}^1 \quad (2.104)$$

Here, the normalized tensor is defined by:

$$\hat{N}_{ij}^1 = \frac{\hat{\xi}_{ij}^1}{\|\hat{\xi}^1\|} = \frac{\hat{S}_{ij}^1 - \hat{\alpha}_{ij}^1}{\|\hat{S}^1 - \hat{\alpha}^1\|} = \frac{\hat{S}_{ij}^1 - \hat{\alpha}_{ij}^1}{K^y} \quad (2.105)$$

The update of the back-stress is performed as

$$\hat{\alpha}_{ij}^1 = \hat{\alpha}_{ij}^0 \exp(-H_{nl} \Delta g) + [1 - \exp(-H_{nl} \Delta g)] \frac{H_{kin}}{H_{nl}} \hat{N}_{ij}^1 = Q \hat{\alpha}_{ij}^0 + (1-Q) \frac{H_{kin}}{H_{nl}} \hat{N}_{ij}^1 \quad (2.106)$$

with

$$Q = \exp(-H_{nl} \Delta g) \quad (2.107)$$

The yield function, Eq. (2.94), can be rewritten in terms of the state variables at the beginning of the increment

$$f_i^{C,A} = -K^C \int_{\partial\Omega_0} N^A g F_{ij}^{-T} N_j J d\partial\Omega_0 \quad (2.108)$$

The plastic consistency parameter Δg is calculated from the yield function, Eq.(2.108), using a local Newton-Raphson scheme. For the calculation of the gradients, Eq. (2.105) is introduced into Eqs. (2.103 and 2.106), which yields the three equations required

$$\hat{\sigma}_{ij}^1 = \hat{\sigma}_{ij}^0 + C_{ijk} \Delta \hat{\epsilon}_k^{1/2} - 2G \Delta g \frac{P_{ijk} \hat{\sigma}_k^1 - \hat{\alpha}_{ij}^1}{K^y} \quad (2.109)$$

$$\hat{\alpha}_{ij}^1 = Q \hat{\alpha}_{ij}^0 + (1-Q) \frac{H_{kin}}{H_{nl}} \frac{P_{ijk} \hat{\sigma}_k^1 - \hat{\alpha}_{ij}^1}{K^y} \quad (2.110)$$

$$s^I = s^0 + \sqrt{\frac{2}{3}} \Delta g \quad (2.111)$$

Eq. (2.110) can be transformed into

$$\hat{\alpha}_{ij}^1 = \frac{H_{nl} K^y Q}{H_{nl} K^y + H_{kin}(1-Q)} \hat{\alpha}_{ij}^0 + \frac{H_{kin}(1-Q)}{H_{nl} K^y + H_{kin}(1-Q)} P_{ijk} \hat{\sigma}_k^1 \quad (2.112)$$

Inserting Eq. (2.112) into Eq. (2.109) gives

$$\hat{\sigma}_{ij}^1 = \frac{1}{1+A} \left[\hat{\sigma}_{ij}^0 + \frac{A}{3} \delta_{ij} \hat{\sigma}_{mm}^0 + 2G \Delta \hat{\epsilon}_{ij}^{1/2} + \left(\lambda + \frac{A}{3} (2G + 3\lambda) \right) \delta_{ij} \Delta \hat{\epsilon}_{mm}^{1/2} + A Q \hat{\alpha}_{ij}^0 \right] \quad (2.113)$$

with

$$A = \frac{2G \Delta g_{nl}}{H_{nl} K^y + H_{kin}(1-Q)} \quad (2.114)$$

2.3.3 The equations for gradient calculation

From Eqs. (2.113, 2.114, 2.107 and 2.99) the following dependencies can be determined

$$\hat{\sigma}_{ij}^1 = \hat{\sigma}_{ij}^1(\hat{\sigma}_{ij}^0, \hat{\alpha}_{ij}^0, \Delta \hat{\epsilon}_{ij}^{1/2}, \mathbf{A}, \mathbf{Q}, \lambda, \mathbf{G}) \quad (2.115)$$

$$A = A(\Delta g, K^y, Q, G) \quad (2.116)$$

$$Q = Q(\Delta g) \quad (2.117)$$

$$K^y = K^y(\Delta g, s^0) \quad (2.118)$$

From Eqs. (2.115-2.118) the total derivatives can be determined

$$\dot{g} = \frac{(\Delta x_i^{AP} - g n_i) N^A \dot{x}_i^A}{\sqrt{\Delta x_m^{AP} n_m - \Delta x_m^{AP} \Delta x_m^{AP} + R^2}} - g \frac{\Delta x_i^{AP} \dot{n}_i}{\sqrt{\Delta x_m^{AP} n_m - \Delta x_m^{AP} \Delta x_m^{AP} + R^2}} \quad (2.119)$$

$$\frac{dA}{d\kappa} = \frac{\partial A}{\partial \kappa} + \frac{\partial A}{\partial \Delta g} \frac{d\Delta g}{d\kappa} + \frac{\partial A}{\partial K^y} \frac{dK^y}{d\kappa} + \frac{\partial A}{\partial Q} \frac{dQ}{d\kappa} + \frac{\partial A}{\partial G} \frac{dG}{d\kappa} \quad (2.120)$$

$$\frac{dQ}{d\kappa} = \frac{\partial Q}{\partial \kappa} + \frac{\partial Q}{\partial \Delta g} \frac{d\Delta g}{d\kappa} \quad (2.121)$$

$$\frac{dK^y}{d\kappa} = \frac{\partial K^y}{\partial \kappa} + \frac{\partial K^y}{\partial \Delta g} \frac{d\Delta g}{d\kappa} + \frac{\partial K^y}{\partial s^0} \frac{ds^0}{d\kappa} \quad (2.122)$$

For the determination of the derivative of the plastic consistency parameter Δg with respect to the material parameter, it has to be kept in mind that in the case of plasticity, the yield condition, Eq. (2.94), has to be fulfilled independently of the material parameters, i.e.

$$\frac{df}{d\kappa} = 0 \quad (2.123)$$

The yield function, Eq. (2.108), gives the following dependencies

$$f = f(\hat{\sigma}^0, \hat{\alpha}^0, \Delta \hat{\epsilon}^{1/2}, \Delta g, \mathbf{Q}, K^y, \mathbf{G}) \quad (2.124)$$

Using

$$n_i = \frac{x_i^P - x_i^A}{\|x_i^P - x_i^A\|} \quad (2.125)$$

together with the property of the normal tensor [2.13]

$$\hat{N}_{ij} = \frac{P_{ijkl} \hat{\sigma}_{kl}^0 + P_{ijkl} C_{klmn} \Delta \hat{\epsilon}_{mn}^{1/2} - Q \hat{\alpha}_{ij}^0}{\|P : \hat{\sigma}^0 + P : C : \Delta \hat{\epsilon}^{1/2} - Q \hat{\alpha}^0\|} = \frac{P_{ijkl} \hat{\sigma}_{kl}^0 + 2GP_{ijkl} \Delta \hat{\epsilon}_{kl}^{1/2} - Q \hat{\alpha}_{ij}^0}{\|P : \hat{\sigma}^0 + 2GP : \Delta \hat{\epsilon}^{1/2} - Q \hat{\alpha}^0\|} \quad (2.126)$$

it can be derived that

$$\begin{aligned}
\frac{df}{d\kappa} &= \frac{\partial f}{\partial \kappa} + \hat{N}_{ij} \frac{d\hat{\sigma}_{ij}^0}{d\kappa} + 2G \hat{N}_{ij} \frac{d\Delta \hat{\epsilon}_{ij}^{1/2}}{d\kappa} - Q \hat{N}_{ij} \frac{d\hat{\alpha}_{ij}^0}{d\kappa} + \left(2\hat{N}_{ij} \Delta \hat{\epsilon}_{ij}^{1/2} + \frac{\partial f}{\partial G} \right) \frac{dG}{d\kappa} \\
&\quad + \left(\frac{\partial f}{\partial Q} - \hat{N}_{ij} \hat{\alpha}_{ij}^0 \right) \frac{\partial Q}{\partial \kappa} + \frac{\partial f}{\partial K^y} \frac{\partial K^y}{\partial \kappa} + \frac{\partial f}{\partial K^y} \frac{\partial K^y}{\partial s^0} \frac{ds^0}{d\kappa} \\
&\quad + \left(\frac{\partial f}{\partial \Delta g} + \frac{\partial f}{\partial K^y} \frac{\partial K^y}{\partial \Delta g} + \frac{\partial f}{\partial Q} \frac{\partial Q}{\partial \Delta g} - \hat{N}_{ij} \hat{\alpha}_{ij}^0 \right) \frac{d\Delta g}{d\kappa} = 0
\end{aligned} \tag{2.127}$$

Solving for the total derivative of the plastic consistency parameter with respect to the material parameter yields

$$\frac{d\Delta g}{d\kappa} = \frac{1}{Z} \left(T^1 + 2G \hat{N}_{ij} \frac{d\Delta \hat{\epsilon}_{ij}^{1/2}}{d\kappa} \right) \tag{2.128}$$

with

$$\begin{aligned}
T^1 &= \frac{\partial f}{\partial \kappa} + \hat{N}_{ij} \frac{d\hat{\sigma}_{ij}^0}{d\kappa} - Q \hat{N}_{ij} \frac{d\hat{\alpha}_{ij}^0}{d\kappa} + \left(2\hat{N}_{ij} \Delta \hat{\epsilon}_{ij}^{1/2} + \frac{\partial f}{\partial G} \right) \frac{dG}{d\kappa} \\
&\quad + \left(\frac{\partial f}{\partial Q} - \hat{N}_{ij} \hat{\alpha}_{ij}^0 \right) \frac{\partial Q}{\partial \kappa} + \frac{\partial f}{\partial K^y} \frac{\partial K^y}{\partial \kappa} + \frac{\partial f}{\partial K^y} \frac{\partial K^y}{\partial s^0} \frac{ds^0}{d\kappa}
\end{aligned} \tag{2.129}$$

and

$$Z = - \left(\frac{\partial f}{\partial \Delta g} + \frac{\partial f}{\partial K^y} \frac{\partial K^y}{\partial \Delta g} + \frac{\partial f}{\partial Q} \frac{\partial Q}{\partial \Delta g} - \hat{N}_{ij} \hat{\alpha}_{ij}^0 \right) \tag{2.130}$$

Inserting Eqs. (2.120, 2.121 and 2.128) into Eq. (2.119) yields

$$\frac{d\hat{\sigma}_{ij}^1}{d\kappa} = T_{ij}^2 + \frac{T^1}{Z} T_{ij}^3 + \left(\frac{2G}{Z} T_{ij}^3 \hat{N}_{kl} + \frac{\partial \hat{\sigma}_{ij}^1}{\partial \Delta \hat{\epsilon}_{kl}^{1/2}} \right) \frac{d\Delta \hat{\epsilon}_{kl}^{1/2}}{d\kappa} \tag{2.131}$$

with

$$\begin{aligned}
T_{ij}^2 &= \frac{\partial \hat{\sigma}_{ij}^1}{\partial \kappa} + \frac{\partial \hat{\sigma}_{ij}^1}{\partial Q} \frac{\partial Q}{\partial \kappa} + \frac{\partial \hat{\sigma}_{ij}^1}{\partial A} \frac{\partial A}{\partial \kappa} + \frac{\partial \hat{\sigma}_{ij}^1}{\partial A} \frac{\partial A}{\partial K^y} \frac{\partial K^y}{\partial \kappa} + \frac{\partial \hat{\sigma}_{ij}^1}{\partial A} \frac{\partial A}{\partial Q} \frac{\partial Q}{\partial \kappa} \\
&\quad + \frac{\partial \hat{\sigma}_{ij}^1}{\partial \hat{\sigma}_{kl}^0} \frac{d\hat{\sigma}_{kl}^0}{d\kappa} + \frac{\partial \hat{\sigma}_{ij}^1}{\partial \hat{\alpha}_{kl}^0} \frac{d\hat{\alpha}_{kl}^0}{d\kappa} + \frac{\partial \hat{\sigma}_{ij}^1}{\partial \lambda} \frac{d\lambda}{d\kappa} + \frac{\partial \hat{\sigma}_{ij}^1}{\partial A} \frac{\partial A}{\partial K^y} \frac{\partial K^y}{\partial s^0} \frac{ds^0}{d\kappa} + \left(\frac{\partial \hat{\sigma}_{ij}^1}{\partial G} + \frac{\partial \hat{\sigma}_{ij}^1}{\partial A} \frac{\partial A}{\partial G} \right) \frac{dG}{d\kappa} \tag{2.132}
\end{aligned}$$

and

$$T_{ij}^3 = \frac{\partial \hat{\sigma}_{ij}^1}{\partial Q} \frac{\partial Q}{\partial \Delta g} + \frac{\partial \hat{\sigma}_{ij}^1}{\partial A} \left(\frac{\partial A}{\partial K^y} \frac{\partial K^y}{\partial \Delta g} + \frac{\partial A}{\partial Q} \frac{\partial Q}{\partial \Delta g} + \frac{\partial A}{\partial \Delta g} \right) \quad (2.133)$$

Using Eq. (2.128), the update of the derivative of the plastic arc length with respect to the material parameter is

$$\frac{ds^1}{d\kappa} = \frac{ds^0}{d\kappa} + \sqrt{\frac{2}{3}} \frac{d\Delta g}{d\kappa} \quad (2.134)$$

and, using Eqs. (2.121 and 2.122) together with Eq. (2.128), the update of the derivative of the rotation-neutralized back-stress with respect to the material parameter is

$$\frac{d\hat{\alpha}_{ij}^1}{d\kappa} = \frac{\partial \hat{\alpha}_{ij}^1}{\partial \kappa} + \frac{\partial \hat{\alpha}_{ij}^1}{\partial \hat{\sigma}_{kl}^0} \frac{d\hat{\sigma}_{kl}^0}{d\kappa} + \frac{\partial \hat{\alpha}_{ij}^1}{\partial \hat{\alpha}_{kl}^0} \frac{d\hat{\alpha}_{kl}^0}{d\kappa} + \frac{\partial \hat{\alpha}_{ij}^1}{\partial Q} \frac{dQ}{d\kappa} + \frac{\partial \hat{\alpha}_{ij}^1}{\partial K^y} \frac{dK^y}{d\kappa} \quad (2.135)$$

The equations above have been developed for a single free material parameter. In the case of several free material parameters, the equations remain valid, with most of the calculations to be performed once for each free material parameter

It can be seen from Eqs. (2.128 and 2.131), that the derivative of the strain increment with respect to the material parameter is required for updating the gradient of the state variables. This still unknown gradient can be determined as described below.

2.3.4 Determination of the Gradients of the kinematic variables

Starting from the basic equation of non-linear finite element analysis

$$r_i^A = f_i^{A,int} - f_i^{A,ext} = 0 \quad (2.136)$$

which, in the discretized form gives

$$r_i^A = \int_{\Omega} \frac{\partial N^A}{\partial x_j} \sigma_{ij} d\Omega - f_i^{A,ext} = 0 \quad (2.137)$$

For simplicity, we assume that the external force f^{ext} is independent of the solution. As Eq. (2.136) is fulfilled independently of the material parameters, the derivative of Eq. (2.137) with respect to a material parameter κ yields

$$\frac{d}{d\kappa} \left(\int_{\Omega} \frac{\partial N^A}{\partial x_j} \sigma_{ij} d\Omega \right) = 0 \quad (2.138)$$

In the undeformed configuration, Eq. (2.138) gives

$$\int_{\Omega_0} \frac{\partial N^A}{\partial X_m} \frac{d}{d\kappa} (F_{mj}^{-1} \sigma_{ij} J d\Omega_0) = 0 \quad (2.139)$$

which can be expanded into

$$\int_{\Omega_0} \frac{\partial N^A}{\partial X_m} \left(\frac{dF_{mj}^{-1}}{d\kappa} \sigma_{ij} J + F_{mj}^{-1} \frac{d\sigma_{ij}}{d\kappa} J + F_{mj}^{-1} \sigma_{ij} \frac{dJ}{d\kappa} \right) d\Omega_0 = 0 \quad (2.140)$$

Using the fact that the constitutive equation is formulated in rotation-neutralized coordinates, with

$$\sigma_{ij} = R_{ik} \hat{\sigma}_{kl} R_{jl} \quad (2.141)$$

and regrouping Eq. (2.140) gives

$$\begin{aligned} & \int_{\Omega_0} \frac{\partial N^A}{\partial X_m} \left(\frac{dF_{mj}^{-1}}{d\kappa} \sigma_{ij} J + F_{mj}^{-1} \sigma_{ij} \frac{dJ}{d\kappa} \right) d\Omega_0 \\ & + \int_{\Omega} \frac{\partial N^A}{\partial x_j} \left(\frac{dR_{ik}}{d\kappa} \hat{\sigma}_{kl} R_{jl} + R_{ik} \frac{d\hat{\sigma}_{kl}}{d\kappa} R_{jl} + R_{ik} \hat{\sigma}_{kl} \frac{dR_{jl}}{d\kappa} \right) d\Omega = 0 \end{aligned} \quad (2.142)$$

It can be shown that the derivatives of kinematic quantities with respect to a material parameter have the same structure as time derivatives of these quantities [2.14]. The identities presented in [2.15, 2.16] then read

$$\frac{dR_{ij}}{d\kappa} = G_{ijmn}{}^{\kappa} l_{mn} \quad (2.143)$$

$$\frac{d\Delta \hat{\epsilon}_{ij}^{1/2}}{d\kappa} = T_{ijm}{}^{\kappa} l_{m} \quad (2.144)$$

$$\frac{dJ}{d\kappa} = J \delta_{mn}{}^{\kappa} l_{mn} \quad (2.145)$$

$$\frac{dF_{mj}^{-1}}{d\kappa} = -F_{ml}^{-1}{}^{\kappa} l_{lj} \quad (2.146)$$

with

$${}^{\kappa} l_{mn} = \frac{\partial}{\partial x_n} \frac{dx_m}{d\kappa} \quad (2.147)$$

and

$$T_{ijkl}^d = R_{ri}^{1/2} \bar{M}_{rskl} R_{sj}^{1/2} + \Delta \hat{\epsilon}_{rs}^{1/2} (R_{ri}^{1/2} \bar{G}_{sjkl} + R_{sj}^{1/2} \bar{G}_{rikl}) \quad (2.148)$$

The tensor M is defined as [2.15]

$$\bar{M}_{ijkl} = \frac{1}{2} \left(\frac{\partial x_i^0}{\partial x_k^{1/2}} \frac{\partial x_j^l}{\partial x_j^{1/2}} + \frac{\partial x_j^0}{\partial x_k^{1/2}} \frac{\partial x_i^l}{\partial x_i^{1/2}} \right) \quad (2.149)$$

The tensors involved into the derivatives of the rotation tensor are calculated as [2.15]

$$G_{ijkl} = (R_{ir} U_{js} - R_{is} U_{jr})^{-1} (R_{kr} F_{ls} - R_{ks} F_{lr}) \quad (2.150)$$

$$\bar{G}_{ijkl} = \frac{1}{2} G_{ijkm}^{1/2} \frac{\partial x_l^1}{\partial x_m^{1/2}} \quad (2.151)$$

Inserting Eqs. (2.143 -2.146) into Eq. (2.142) gives

$$\begin{aligned} & \int_{\Omega_0} \frac{\partial N^A}{\partial X_m} F_{mj}^{-1} (-\delta_{kj} \sigma_{il} + \delta_{kl} \sigma_{ij})^{\kappa} I_{kl} J d\Omega_0 \\ & + \int_{\Omega} \frac{\partial N^A}{\partial x_j} \left(G_{ikmn}^{\kappa} I_{mn} \hat{\sigma}_{kl} R_{jl} + R_{ik} \frac{d\hat{\sigma}_{kl}}{d\kappa} R_{jl} + R_{ik} \hat{\sigma}_{kl} G_{jlmn}^{\kappa} I_{mn} \right) d\Omega = 0 \end{aligned} \quad (2.152)$$

which can be regrouped into

$$\begin{aligned} & \int_{\Omega} \frac{\partial N^A}{\partial x_j} (-\delta_{mj} \sigma_{in} + \delta_{mn} \sigma_{ij} + G_{ikmn} \hat{\sigma}_{kl} R_{jl} + R_{ik} \hat{\sigma}_{kl} G_{jlmn})^{\kappa} I_{mn} d\Omega \\ & + \int_{\Omega} \frac{\partial N^A}{\partial x_j} R_{ik} \frac{d\hat{\sigma}_{kl}}{d\kappa} R_{jl} d\Omega = 0 \end{aligned} \quad (2.153)$$

Introducing Eq. (2.131) together with Eq. (2.144) into Eq. (2.153) gives

$$\int_{\Omega} \frac{\partial N^A}{\partial x_j} L_{ijmm}^{\kappa} I_{mn} d\Omega + f_i^A = 0 \quad (2.154)$$

with

$$\begin{aligned} L_{ijmm}^{\kappa} &= -\delta_{mj} \sigma_{in} + \delta_{mn} \sigma_{ij} + G_{ikmn} \hat{\sigma}_{kl} R_{jl} + R_{ik} \hat{\sigma}_{kl} G_{jlmn} \\ & + R_{ik} \left(\frac{2G}{Z} T_{kl}^3 \hat{N}_{pq} + \frac{\partial \hat{\sigma}_{kl}^1}{\partial \Delta \hat{\epsilon}_{pq}^{1/2}} \right) T_{pqmm}^d R_{jl} \end{aligned} \quad (2.155)$$

and

$$f_i^A = \int_{\Omega} \frac{\partial N^A}{\partial x_j} R_{ik} \left(T_{kl}^2 + \frac{T_{kl}^1}{Z} T_{kl}^3 \right) R_{jl} d\Omega \quad (2.156)$$

Through the discretization

$$\kappa_{l_{mn}} = \frac{\partial N^B}{\partial x_n} \frac{dx_m^B}{d\kappa} \quad (2.157)$$

Eq. (2.154) becomes

$$\int_{\Omega} \frac{\partial N^A}{\partial x_j} \kappa_{L_{ijmn}} \frac{\partial N^B}{\partial x_n} d\Omega \frac{dx_m^B}{d\kappa} + \kappa_{f_i^A} = 0 \quad (2.158)$$

rewritten as

$$K_{im}^{AB} \kappa_{x_m^B} + \kappa_{f_i^A} = 0 \quad (2.159)$$

This equation, established and summed up for all pairs of nodes belonging to a common element, gives the global set of linear equations, which after solving gives the unknowns $\kappa_{x_m^B}$. Substituting Eqs. (2.144 and 2.157) into Eqs. (2.128 and 2.131), the rotation-neutralized Cauchy stress and the consistency parameter gradients can be calculated from the nodal gradient $\kappa_{x_m^B}$.

$$\frac{d\hat{\sigma}_{ij}^1}{d\kappa} = T_{ij}^2 + \frac{T^1}{Z} T_{ij}^3 + \left(\frac{2G}{Z} T_{ij}^3 \hat{N}_{kl} + \frac{\partial \hat{\sigma}_{ij}^1}{\partial \Delta \hat{\epsilon}_{kl}^{1/2}} \right) T_{klmn}^d \frac{\partial N^B}{\partial x_n} \frac{dx_m^B}{d\kappa} \quad (2.160)$$

$$\frac{d\Delta}{d\kappa} = \frac{1}{Z} \left(T^1 + 2G \hat{N}_{ij} T_{ijkl}^d \frac{\partial N^B}{\partial x_l} \frac{dx_k^B}{d\kappa} \right) \quad (2.161)$$

The gradient of the arc length and of the back-stress can be calculated using Eqs. (2.134 and 2.135) respectively after introducing Eq. (2.161) into Eqs. (2.120-2.122).

2.3.5 Procedure for the gradient calculation

The gradient calculation involves the update of the derivatives of the rotation-neutralized Cauchy stress and back-stress and of the plastic arc length with respect to the material parameter. In practice, this is done in three stages, at the end of each time increment, after convergence of the state variable update:

Calculation of the pseudo stiffness matrix and pseudo load vector from Eq. (2.159). It should be noted that the pseudo stiffness matrix is independent of the free material parameters, whereas the pseudo load vector has to be calculated for each free material parameter.

Solution of Eq. (2.159) for each free material parameter to obtain the unknowns.

Backsubstitution of the unknowns into Eqs. (2.131, 2.134 and 2.135) to obtain the updated derivatives at the end of the increment.

For the update procedure of the derivatives, the derivatives of the state at the beginning of the first increment, i.e. at time $t=0$, have to be known. As the state variables at time $t=0$ are nothing else than the boundary conditions of the boundary value problem, which are independent of the material parameters, the derivatives of the state variables at time $t=0$ are zero:

$$\frac{d\hat{\alpha}_{ij}^0}{d\kappa}\Big|_{t=0} = \frac{d\hat{\sigma}_{kl}^0}{d\kappa}\Big|_{t=0} = \frac{ds^0}{d\kappa}\Big|_{t=0} = 0 \quad (2.162)$$

In the present study, the material parameters are determined from a uniaxial stress-strain curve including loading and unloading, which is necessary for obtaining a unique solution [2.17]. In this case, the error function is defined as the sum of squared differences between experimental and computed stress. Assuming that the experiment is displacement driven, the independent variable is the total strain. The error function Ξ is based on the stress.

$$\Xi = \sum_{k=1}^N \left[\bar{\sigma}(\epsilon_t^k) - \sigma(\epsilon_t^k) \right]^2 \quad (2.163)$$

and the material parameters κ_i . The gradient of the error function is given as

$$\frac{d\Xi}{d\kappa_i} = -2 \sum_{k=1}^N \left[\bar{\sigma}(\epsilon_t^k) - \sigma(\epsilon_t^k) \right] \frac{d\sigma(\epsilon_t^k)}{d\kappa_i} \quad (2.164)$$

For using the Gauss-Newton optimisation method, the Hessian matrix is approximated as

$$\tilde{H}_{ij} = 2 \sum_{k=1}^N \frac{d\sigma(\epsilon_t^k)}{d\kappa_i} \frac{d\sigma(\epsilon_t^k)}{d\kappa_j} \quad (2.165)$$

From Eqs. (2.164 and 2.165) it can be seen that the gradient has to be evaluated at each available data point, i.e. for each value of total strain. As Eqs. (2.164 and 2.165) involve the Cauchy stress in global coordinates, the gradient of the rotation-neutralized Cauchy stress has to be transformed into global coordinates using

$$\frac{d\sigma_{ij}}{d\kappa} = \left(G_{ikmn} \hat{\sigma}_{kl} R_{jl} + R_{ik} \hat{\sigma}_{kl} G_{jlmn} \right) \kappa_{lm} + R_{ik} \frac{d\hat{\sigma}_{kl}}{d\kappa} R_{jl} \quad (2.166)$$

In case the experiment records the load, the total load can be computed by adding the nodal forces of all nodes located on a specific reaction surface Γ_{react} , using Eq. (2.137). In the absence of external nodal forces, this yields.

$$R_i^{\text{tot}} = \sum r_i^A = \sum \int_{\Omega} \frac{\partial N^A}{\partial x_j} \sigma_{ij} d\Omega \quad \forall A \in \Gamma_{\text{react}} \quad (2.167)$$

The magnitude of the load is then

$$R^{tot} = \left\| R_i^{tot} \right\| \quad (2.168)$$

The derivative with respect to the material parameter of the load becomes

$$\frac{dR_i^{tot}}{d\kappa} = \sum^A \int_{\Omega} \frac{\partial N^A}{\partial x_j} \frac{d\sigma_{ij}}{d\kappa} d\Omega \quad \forall A \in \Gamma_{react} \quad (2.169)$$

In the two-dimensional case, the derivative of the magnitude of the reaction force with respect to the material parameter is

$$\frac{dR^{tot}}{d\kappa} = \frac{1}{R^{tot}} \left(\frac{dR_x^{tot}}{d\kappa} + \frac{dR_y^{tot}}{d\kappa} \right) \quad (2.170)$$

In Eqs. (2.163 -2.165), the stress is replaced by the load magnitude, which gives

$$\Xi = \sum_{k=1}^N \left[\bar{R}^{tot}(\varepsilon_t^k) - R^{tot}(\varepsilon_t^k) \right]^2 \quad (2.171)$$

$$\frac{d\Xi}{d\kappa_i} = -2 \sum_{k=1}^N \left[\bar{R}^{tot}(\varepsilon_t^k) - R^{tot}(\varepsilon_t^k) \right] \frac{dR^{tot}(\varepsilon_t^k)}{d\kappa_i} \quad (2.172)$$

$$\tilde{H}_{ij} = 2 \sum_{k=1}^N \frac{dR^{tot}(\varepsilon_t^k)}{d\kappa_i} \frac{dR^{tot}(\varepsilon_t^k)}{d\kappa_j} \quad (2.173)$$

2.3.6 Numerical example

In order to validate the computational material parameter identification routine, a reidentification problem has been treated. In this problem case, a simulation is carried out with known material parameters, and the characteristic stress-strain or load displacement curve is used as an artificial experimental data set. In order to assess the validity of the rotation-neutralized formulation, a rotating-stretching bar is treated. In this case, a rigid body rotation is superposed to the elongation of a bar. It should be noted that because of the imposition of the boundary conditions, the bar is supposed to be laterally constrained. In the example treated, the bar is rotated clockwise by 90 degrees during loading, and rotated back to the initial position during unloading, as shown in Fig. 2.1.

The rotating-stretching bar is described by the deformation gradient

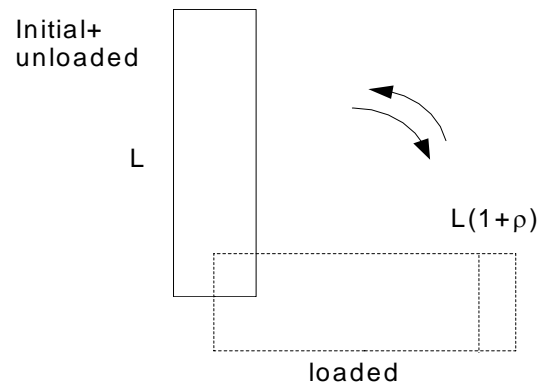


Fig. 2.1 Schematic of the rotating-stretching bar problem.

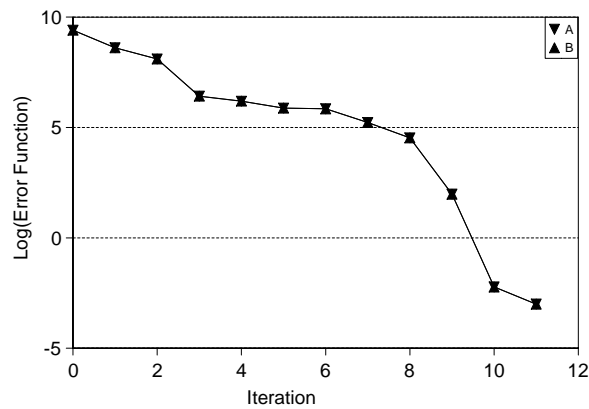


Fig. 2.2 Error function over iteration number for the rotating-stretching bar problem.

$$F = \begin{pmatrix} \cos\left(\frac{\pi}{2}t\right) & -(1+\rho t)\sin\left(\frac{\pi}{2}t\right) & 0 \\ \sin\left(\frac{\pi}{2}t\right) & (1+\rho t)\cos\left(\frac{\pi}{2}t\right) & 0 \\ 0 & 0 & 1 \end{pmatrix} \quad \text{with } 0 \leq t \leq 1 \quad (2.174)$$

Where ρ is the amount of stretch applied to the bar in its axial direction. The same load can be applied easily without rigid body rotation. Two computations have been performed: one with and one without rigid body rotation. It was found that convergence occurred after the same number of iterations. The error function had roughly the same values, with differences being due to the calculation of the

Table 2.15 Material parameters used in the artificial experiment, the initial guess and the values obtained through the optimisation routine.

<i>Material Parameters</i>	<i>Artificial Experiment</i>	<i>Initial guess</i>	<i>Rotating- Stretching Bar</i>	<i>Stretching Bar</i>
$\sigma^{y,0}$	370	500	369,9995	369,9995
R	24000	10000	24001,5365	24000,0549
β	90	200	90,0057	90,0001
H_{kin}	6500	10000	6500,4579	6500,0550
H_{iso}	170	100	170,0122	170,0017
E	200000	150000	200012,3402	200000,0025
Iterations	-	-	11	11

rotation-neutralized strain increment. The development of the error function over the iteration is shown in Fig. 2.2. The model parameters used in the calculation of the artificial experimental data, the initial guess and the material parameters obtained for the calculation with and without rigid body rotation are shown in Table 2.15. From the close fit of the data and the identical number of iterations, it can be concluded that the rotation-neutralized formulation is valid for finite strain analysis.

2.3.7 Annex

In this study, the constitutive equations with isotropic hypoelasticity and plasticity with non-linear isotropic and kinematic hardening have 7 material parameters. However, as in tensile testing, the impact of the Poisson's ratio on the tress-strain curve is small, this material parameter is fixed to $\nu=0.3$, which is a typical value for metals. The free material parameters are put in vector form:

$$\kappa = (\sigma^{y,0}, R, \beta, H_{kin}, H_{nl}, E) \quad (2.175)$$

It should be noted that the finite element program uses, for the exponent of the kinematic hardening law

$$H_{nl} = \sqrt{\frac{2}{3}}b \quad (2.176)$$

Therefore, the derivatives with respect to H_{nl} have to be converted to the derivatives with respect to b using

$$\frac{\partial}{\partial b} = \frac{\partial}{\partial H_{nl}} \frac{\partial H_{nl}}{\partial b} = \sqrt{\frac{2}{3}} \frac{\partial}{\partial H_{nl}} \quad (2.177)$$

For the partial derivatives with respect to the material parameters, only non-zero derivatives are explicitly given in the following section.

Partial derivatives of the non-linear yield stress

$$\frac{\partial K^y}{\partial \sigma^{y,0}} = \sqrt{\frac{2}{3}} \quad (2.178)$$

$$\frac{\partial K^y}{\partial R} = \sqrt{\frac{2}{3}} \frac{1 - \exp(-\beta s^l)}{\beta} \quad (2.179)$$

$$\frac{\partial K^y}{\partial \beta} = \sqrt{\frac{2}{3}} R \frac{(1 + \beta s^l) \exp(-\beta s^l) - 1}{\beta^2} \quad (2.180)$$

$$\frac{\partial K^y}{\partial \Delta g} = \frac{2}{3} R \exp(-\beta s^l) \quad (2.181)$$

$$\frac{\partial K^y}{\partial s^0} = \sqrt{\frac{2}{3}} R \exp(-\beta s^l) \quad (2.182)$$

Partial derivatives of the yield function

$$\frac{\partial f}{\partial H_{kin}} = -\frac{1-Q}{H_{nl}} \quad (2.183)$$

$$\frac{\partial f}{\partial H_{nl}} = \frac{H_{kin}(1-Q)}{H_{nl}^2} \quad (2.184)$$

$$\frac{\partial f}{\partial G} = -2\Delta g \quad (2.185)$$

$$\frac{\partial f}{\partial Q} = \frac{H_{kin}}{H_{nl}} \quad (2.186)$$

$$\frac{\partial f}{\partial \Delta g} = -2G \quad (2.187)$$

$$\frac{\partial f}{\partial K^y} = -1 \quad (2.188)$$

Total derivatives of G

$$\frac{dG}{dE} = \frac{1}{2(1+\nu)} \quad (2.189)$$

Total derivatives of λ

$$\frac{d\lambda}{dE} = \frac{\nu}{(1+\nu)(1-2\nu)} \quad (2.190)$$

Partial derivatives of Q

$$\frac{\partial Q}{\partial H_{nl}} = -Q\Delta\Delta \quad (2.191)$$

$$\frac{\partial Q}{\partial \Delta g} = -H_{nl}Q \quad (2.192)$$

Partial derivatives of A

$$\frac{\partial A}{\partial \Delta g} = \frac{2GH_{nl}}{H_{nl}K^y + H_{kin}(1-Q)} \quad (2.193)$$

$$g n_i n_i = g = (x_i^P - x_i^A) n_i - (x_i^{P'} - x_i^A) n_i = (x_i^P - x_i^A) n_i - R \quad (2.194)$$

$$f_i^C = -K^C g n_i \quad (2.195)$$

$$L_{ik}^{C,P} = -K^C \left(\delta_{ik} \frac{g}{\|x^P - x^A\|} + n_i n_k \frac{R}{\|x^P - x^A\|} \right) \quad (2.196)$$

$$\lim_{g \rightarrow 0} \|x^P - x^A\| = R \quad (2.197)$$

$$L_{ik}^{C,P} = -K^C n_i n_k \quad (2.198)$$

Partial derivatives of the updated rotation-neutralized Cauchy stress

$$\dot{f}_i^C = -K^C (\dot{g} n_i + g \dot{n}_i) \quad (2.199)$$

$$g n_i = x_i^P - x_i^{P'} = (x_i^P - x_i^A) - (x_i^{P'} - x_i^A) \quad (2.200)$$

$$\frac{\partial \hat{\sigma}_{ij}^1}{\partial \Delta \hat{\epsilon}_{kl}^{1/2}} = \frac{1}{1+A} \left(2G I_{ijkl} + \left[\lambda + \frac{A}{3} (2G + 3\lambda) \right] \delta_{ij} \delta_{kl} \right) \quad (2.201)$$

$$\frac{\partial \hat{\sigma}_{ij}^1}{\partial \lambda} = \delta_{ij} \Delta \hat{\epsilon}_{mm} \quad (2.202)$$

$$\frac{\partial \hat{\sigma}_{ij}^1}{\partial G} = \frac{1}{1+A} \left(2\Delta \hat{\epsilon}_{ij}^{1/2} + \frac{2A}{3} \delta_{ij} \Delta \hat{\epsilon}_{mm}^{1/2} \right) \quad (2.203)$$

$$\dot{n}_i = \frac{\dot{x}_i - \dot{x}_k n_k n_i}{\|x^P - x^A\|} \quad (2.204)$$

$$\dot{f}_i^C = -K^C \left[\delta_{ik} + \frac{R}{\|x^P - x^A\|} (n_i n_k - \delta_{ik}) \right] \dot{x}_k \quad (2.205)$$

$$\dot{g} = \dot{x}_k n_k \quad (2.206)$$

Partial derivatives of the updated rotation-neutralized back-stress

$$t_i(\xi) = \frac{\sum_{A=1}^{N_E} x_i^A \partial \frac{N^A}{\partial \xi}}{\left\| \sum_{A=1}^{N_E} x_i^A \partial \frac{N^A}{\partial \xi} \right\|} = \frac{x_i^A \partial \frac{N^A}{\partial \xi}}{\left\| x_i^A \partial \frac{N^A}{\partial \xi} \right\|} \quad (2.207)$$

$$x_i^P - x_i^{P'} = g n_i \quad (2.208)$$

$$x_i^A - x_i^{P'} = (x_i^P - x_i^{P'}) + (x_i^A - x_i^P) \quad (2.209)$$

$$g n_i = (x_i^A - x_i^{P'}) - (x_i^A - x_i^P) \quad (2.210)$$

$$g n_i n_i = g = ((x_i^A - x_i^{P'}) - (x_i^A - x_i^P)) n_i \quad (2.211)$$

$$g = (x_i^P - x_i^A) n_i \quad (2.212)$$

2.4 Implementation of rigid contact

The modelling of indentation experiments of non-linear materials requires the ability to perform a contact analysis using the finite element method. In the case of contact, the boundary conditions under the active indenter surface cannot be prescribed using displacement boundary conditions. In the case of rigid contact, the displacement of the rigid contact surface, called the master surface, leads to a penetration of the contact surface and the solid body. This penetration is iteratively reduced applying loads at the active contact surface. Three methods exist for contact modelling:

1. Penalty Method
2. Lagrange Method
3. Augmented Lagrange Method

Whereas the Lagrange method is difficult to apply because of the changing contact status (open and contact) during the iterative steps, the augmented Lagrange Method, which consists of a penalty step followed by one or several Lagrange iterations, circumvents this problem. However, this method was discarded because of the high number of iterations resulting from the multiple iteration steps per increment. The method used is the penalty method, stabilized by an adaptive descent scheme, which enables the use of a higher contact stiffness necessary for acceptable levels of penetration. Both the penalty method and the adaptive descent scheme will be presented in the following section.

In the context of the CASSEM project, only two-dimensional, e.g. axisymmetric, rigid contact is considered. Contact elements, which are in fact pseudo-elements laid over the solid elements, can be subdivided into three classes:

1. Node-to-node contact elements
2. Node-to-surface elements
3. Surface-to-surface elements

Node-to-node contact elements are not appropriate in this project, because they use a fixed normal direction of the contact. Both the other methods have been implemented.

2.4.1 Contact modelling

The penalty method

In our case, only contact between one deformable and a rigid body is considered. In addition to that, the contact is assumed to be friction-free. Without interaction, the movement of the two bodies produces interpenetration. For a given point P at the surface of the deformable body, a point P' on the surface of the rigid body can be determined in a way to minimize the distance pp'. P' is called the closest point projection of P on the rigid surface. The distance of PP', called the gap g, is the local amount of penetration between the two bodies. The gap g is defined in such a way that for a positive gap g, the two bodies are not in contact, i.e. no overlap, and for negative g, the bodies are overlapping and henceforth in contact.

In the penalty method, this gap is reduced by applying a force at the point P of the deformable body, defined by

$$f_i^C = -K^C g n_i \quad (2.213)$$

The constant K^C is called the normal contact stiffness and the normal to the rigid surface in the projected point is given by n. The nodal force f^c has for effect to reduce the magnitude of the gap. In case of friction, a similar relationship can be deduced for the tangential, e.g. frictional force. More details on contact and friction modelling can be found in [2.18]. The penalty method can be derived from the Lagrange multiplier method, where the Lagrange multiplier, which is the force needed to make the gap vanish exactly, is replaced by the force calculated by Eq. (2.213), which has for a consequence that the gap is not reduced to zero, but a small gap value persists. Generally speaking, the higher the normal contact stiffness, the smaller the gap. However, convergence is harder or impossible to obtain for higher values of normal stiffness.

The main task of contact modelling consists of calculating the gap magnitude g, the normal to the rigid surface, n, and to calculate the contact part of the tangent of the Newton-Raphson iterative scheme. The tangent is calculated from the material time derivative of Eq. (2.213).

$$\dot{f}_i^C = -K^C (\dot{g} n_i + g \dot{n}_i) \quad (2.214)$$

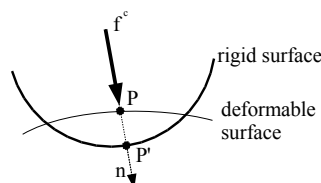


Fig. 2.3 Sketch of contact entities.

2.4.2 Spherical/cylindrical node-to-surface contact

The location of the centre of the rigid sphere/cylinder, A, is known, as well as the radius, R. As P' is the normal projection of the point P on the rigid spherical/cylindrical surface, the outward normal n is given as

$$n_i = \frac{x_i^P - x_i^A}{\|x_i^P - x_i^A\|} \quad (2.215)$$

Multiplying the relationship

$$g n_i = x_i^P - x_i^{P'} = (x_i^P - x_i^A) - (x_i^{P'} - x_i^A) \quad (2.216)$$

with the normal vector gives

$$g n_i n_i = g = (x_i^P - x_i^A) n_i - (x_i^{P'} - x_i^A) n_i = (x_i^P - x_i^A) n_i - R \quad (2.217)$$

Inserting Eq. (2.215) into Eq. (2.217) yields, after some simplifications

$$g = \|x_i^P - x_i^A\| - R \quad (2.218)$$

It should be noted that in fact two projections of the point P on the rigid surface exist: one with minimal and one with maximal distance. In order to make sure that Eq. (2.218) gives the closest point projection, it should be taken care to define increment sizes with a displacement smaller than the sphere/cylinder radius.

With the gap rate

$$\dot{g} = \dot{x}_k n_k \quad (2.219)$$

and the material time derivative of the normal vector

$$\dot{n}_i = \frac{\dot{x}_i - \dot{x}_k n_k n_i}{\|x^P - x^A\|} \quad (2.220)$$

Eq. (2.214) becomes

$$\dot{f}_i^C = -K^C \left[\delta_{ik} + \frac{R}{\|x^P - x^A\|} (n_i n_k - \delta_{ik}) \right] \dot{x}_k \quad (2.221)$$

As the velocities are nodal values, the stiffness matrix can be rearranged to

$$L_{ik}^{C,P} = -K^C \left(\delta_{ik} \frac{g}{\|x^P - x^A\|} + n_i n_k \frac{R}{\|x^P - x^A\|} \right) \quad (2.222)$$

During the iteration,

$$\lim_{g \rightarrow 0} \|x^P - x^A\| = R \quad (2.223)$$

and Eq. (2.222) can tends towards a simplified form of contact tangent matrix for the Newton Raphson scheme

$$L_{ik}^{C,P} = -K^C n_i n_k \quad (2.224)$$

This form is used because it has better convergence characteristics.

2.4.3 Conical/wedge-like node-to-surface contact

The contact normal direction, defined as the outer normal of the rigid surface, is predefined by the opening angle of the cone/wedge surface, as stated in the model definition file. The location of the tip of the cone/wedge, A, is also known. From geometrical considerations, it follows that

$$x_i^P - x_i^{P'} = g n_i \quad (2.225)$$

and

$$x_i^A - x_i^{P'} = (x_i^P - x_i^{P'}) + (x_i^A - x_i^P) \quad (2.226)$$

Eqs. (2.225 and 2.226) can be combined to

$$g n_i = (x_i^A - x_i^{P'}) - (x_i^A - x_i^P) \quad (2.227)$$

Performing a scalar product with the normal vector n yields

$$g n_i n_i = g = ((x_i^A - x_i^{P'}) - (x_i^A - x_i^P)) n_i \quad (2.228)$$

Because of normality, the first term vanishes, giving the gap g at point P as

$$g = (x_i^P - x_i^A) n_i \quad (2.229)$$

With the material time derivatives

$$\dot{g} = \dot{x}_k n_k \quad (2.230)$$

and the material time derivative of the normal vector

$$\dot{n}_i = 0 \quad (2.231)$$

Eq. (2.214) becomes

$$f_i^C = -K^C n_i n_k \dot{x}_k \quad (2.232)$$

and the exact tangent matrix is the same as the simplified tangent for the case of spherical/cylindrical contact, Eq. (2.224).

2.4.4 Spherical/cylindrical surface-to-surface contact

Nodal force and stiffness calculation

In the case of the surface-to-surface contact elements, the contact pressure is distributed over the element edge. This means that the normal direction is defined by the deformable body, not by the rigid contact body. The nodal forces and stiffness matrix are calculated through a numerical integration at integration points, which implies that contact detection is also performed at the integration points. This method relies on Gaussian quadrature. In case of Newton-Kotes nodal integration, contact detection is performed at the nodes. However, in our context, we stick to Gaussian integration, with one of the major advantages being the uniqueness of the surface normals at the Gauss points as opposed to the nodes.

With the number of nodes per contact element, N_E , the tangent vector to the element edge at the location ξ is calculated as

$$t_i(\xi) = \frac{\sum_{A=1}^{N_E} x_i^A \frac{\partial N^A}{\partial \xi}}{\left\| \sum_{A=1}^{N_E} x_i^A \frac{\partial N^A}{\partial \xi} \right\|} = \frac{x_i^A \frac{\partial N^A}{\partial \xi}}{\left\| x_i^A \frac{\partial N^A}{\partial \xi} \right\|} \quad (2.233)$$

and the normal vector is derived from the tangent vector, with the permutation symbol ε_{ijk} , as

$$n_x = t_y \quad n_y = -t_x \Leftrightarrow n_i = \varepsilon_{ij3} t_j \quad (2.234)$$

With the normal vector defined by the deformable body, the gap is calculated as

$$g = (x_i^P - x_i^A) n_i - \sqrt{(x_i^P - x_i^A) n_i - (x_i^P - x_i^A)(x_i^P - x_i^A) + R^2} \quad (2.235)$$

The nodal force calculation is performed as

$$f_i^{C,A} = -K^C \sum_{B=1}^{N_{Nodes}} \int_{\partial\Omega} N^B g n_i d\partial\Omega \quad (2.236)$$

It should be noted that the actual summation is only performed over the non-zero shape functions for the node A. The time derivative of Eq. (2.15), neglecting the change of integration domain, gives

$$\dot{f}_i^{C,A} = -K^C \sum_{B=1}^{N_{Nodes}} \int_{\partial\Omega} N^B (\dot{g} n_i + g \dot{n}_i) d\partial\Omega \quad (2.237)$$

with

$$\dot{n}_i = \frac{\varepsilon_{ij3} (\delta_{jk} - t_j t_k) \frac{\partial N^A}{\partial \xi}}{\left\| \mathbf{x}^A \frac{\partial N^A}{\partial \xi} \right\|} \dot{x}_k = \frac{\varepsilon_{ik3} - n_i t_k}{\left\| \mathbf{x}^A \frac{\partial N^A}{\partial \xi} \right\|} \frac{\partial N^A}{\partial \xi} \dot{x}_k \quad (2.238)$$

and

$$\dot{g} = \frac{(\Delta x_i^{AP} - g n_i) N^A \dot{x}_i}{\sqrt{\Delta x_m^{AP} n_m - \Delta x_m^{AP} \Delta x_m^{AP} + R^2}} - g \frac{\Delta x_i^{AP} \dot{n}_i}{\sqrt{\Delta x_m^{AP} n_m - \Delta x_m^{AP} \Delta x_m^{AP} + R^2}} \quad (2.239)$$

using the notation

$$\Delta x_i^{AP} = x_i^P - x_i^A \quad (2.240)$$

The tangent matrix is calculated as

$$K_{ij}^{C,AB} = -2\pi K^C \sum_{A,B=1}^{N_{Nodes}} \int_{\partial\Omega} n_i N^A \left[\frac{(\Delta x_j^{AP} - g n_j) N^B - g (\varepsilon_{jk3} \Delta x_k^{AP} - t_j \Delta x_k^{AP} n_k) \frac{\partial N^B}{\partial s}}{\sqrt{\Delta x_m^{AP} n_m - \Delta x_m^{AP} \Delta x_m^{AP} + R^2}} \right] r ds \quad (2.241)$$

Two-noded element

For the two-noded elements, the interpolation along the element length is performed through the linear shape functions with the variable ξ

$$N^1 = \frac{1-\xi}{2} \quad \text{and} \quad N^2 = \frac{1+\xi}{2} \quad (2.242)$$

The integration is performed in the current configuration using two integration points.

Three-noded element

For the three-noded elements, the interpolation along the element length is performed through the quadratic shape functions with the variable ξ

$$N^1 = \xi \frac{1-\xi}{2}, \quad N^2 = 1-\xi^2 \quad \text{and} \quad N^3 = \xi \frac{1+\xi}{2} \quad (2.243)$$

For the numerical integration, three integration points are used. However, integration can also be performed using two integration points, but this to be less stable.

2.4.5 Implementation of adaptive descent

The purpose of adaptive descent is to stabilize the Newton-Raphson iterative process in case of convergence difficulties. The adaptive descent scheme works as follows [2.19]:

The stiffness matrix of the first iteration of the increment, K_0 , is stored. If the residual of the iterative calculation step increases, the current stiffness K_n is replaced by the stiffness matrix K_n^* of the following form

$$K_n^* = \phi K_0 + (1-\phi)K_n \quad (2.244)$$

with $\phi=1$, and the iterative step is repeated. After three iterations with decreasing residual, the parameter ϕ is multiplied by 0.25. For the following iterations, ϕ is set to 1 if the residual increases or multiplied by 0.25 if the residual decreases. If ϕ is less than 0.0156, ϕ is set to zero.

It was found that adaptive descent works fine with the node-to-surface elements. However, with surface-to-surface elements, no improvement in convergence behaviour was found.

2.4.6 Contact definition

General description

The contact definitions are introduced into the input file after the definition of the boundary conditions. There are five possible definitions. All definitions are in lower-case letters. The first line states one of the five contact definition types. For 'nocon', i.e. the absence of any contact elements, this is the only required input line. For the other for contact definition types, the next line states the number of contact elements, N_{con} . The next line contains the eight contact parameters. The next N_{con} lines contain the node definitions of the contact elements. It should be noted that only one contact surface can be defined. In a two-dimensional analysis with a wedge-like contact surface, i.e. under plane strain conditions, the wedge tip should be located on the vertical symmetry line ($x=0$).

Nocon

No contact elements present.

Nosur

Rigid spherical or cylindrical node-to-surface contact, depending on the model definition flag axi/psn. The first two parameters define the x and y coordinates of the sphere or cylinder centre. The third and fourth parameters define the maximum horizontal and vertical displacement of the contact surface. The fifth

parameter defines the sphere or cylinder radius. The sixth parameter defines the normal interface contact stiffness. The seventh and eighth parameters are blank parameters.

The next lines contain one node number, which defines the slave node of the solid body to be penetrated by the contact surface.

Ncone

Rigid conical or wedge-like node-to-surface contact, depending on the model definition flag *axi/psn*. The first two parameters define the x and y coordinates of the cone or wedge tip. The third and fourth parameters define the maximum horizontal and vertical displacement of the contact surface. The fifth parameter defines the opening angle of the cone or wedge in degrees measured from the vertical direction. The sixth parameter defines the normal interface contact stiffness. The seventh and eighth parameters are blank parameters.

The next lines contain one node number, which defines the slave node of the solid body to be penetrated by the contact surface.

Ssur2

Two-noded surface-to-surface spherical/cylindrical contact element. The first two parameters define the x and y coordinates of the sphere or cylinder centre. The third and fourth parameters define the maximum horizontal and vertical displacement of the contact surface. The fifth parameter defines the sphere or cylinder radius. The sixth parameter defines the normal interface contact stiffness. The seventh and eighth parameters are blank parameters.

The next lines contain two node numbers, which define the element edge of the element of the solid body to be penetrated by the contact surface. The outward normal of the solid body points to the left if moving from the first to the second node.

Ssur3

Three-noded surface-to-surface spherical/cylindrical contact element. The first two parameters define the x and y coordinates of the sphere or cylinder centre. The third and fourth parameters define the maximum horizontal and vertical displacement of the contact surface. The fifth parameter defines the sphere or cylinder radius. The sixth parameter defines the normal interface contact stiffness. The seventh and eighth parameters are blank parameters.

The next lines contain three node numbers, which define the element edge of the element of the solid body to be penetrated by the contact surface. The outward normal of the solid body points to the left if moving from the first to the third node. The second node is the mid-side node and has to coincide with the mid-side node of the underlying solid element.

2.4.7 Adaptive descent

Adaptive descent is switched on and off through the fifth parameter of the third line in the model definition file:

'adp' switches on adaptive descent.

'nad' switches off adaptive descent.

2.4.8 Further changes

The input file was modified in such a way that the material definitions are now performed after the definition of the contact elements. The most important change however has been done in the program itself. The program has been split in two parts. The first part, called MEESCHTER, controls the overall calculations, reads in the geometric definitions, defines the material parameters and chooses the number of load steps and increments per load step.

The finite element calculation is performed in a subroutine, which performs the calculation of a full load step and returns the contact body displacement together with the total indentation force, calculated by summing up the vertical nodal contact forces. For the time being, this works only with the node-to-surface contact elements. A value quantifying the average gap of the contact elements is also provided to access the quality of the numerical contact results.

The advantage is that for the CASSEM project, numerical indentation experiments can be performed easier, using a subroutine for the calculations, which can be called for both the neural networks-based method and for the optimisation method. A further improvement may consist of performing the geometry input in a separate subroutine, which can then be called by the main control program.

2.4.9 Conclusions

Efforts were focussed on node-to-surface elements because surface-to-surface elements do not improve their convergence with the use of the adaptive descent scheme.

2.5 Nanoindentation test

Nanoindentation, also known as instrumented indentation testing, is a form of mechanical testing developed over the past two decades and based on the hardness tests principle. An indenter is driven into and withdrawn from a material, and the applied load and the resulting displacement are continuously recorded. This technique is used to measure mechanical properties of surfaces on thin depths (from hundreds of nanometers to micrometers). It is useful to analyse coating or thin films, which cannot be tested with conventional methods (tensile tests, hardness, etc.). It can also be used to analyse areas located at specific positions of a bulk material, with a position precision of one micrometer. The indentation equipment consists of four components:

- The force actuator: low loads can be obtained with different devices: electromagnetic with coil and magnet assembly, electrostatic using a capacitor with fixed and moved plates or piezoelectric.
- The column, mobile part of the equipment, is often made of materials with low coefficient of thermal expansion.
- The displacement sensor: the displacement can be measured with a capacitive sensor, a linear variable differential transformers (LVDTs) or laser interferometer.
- The pin or indenter: generally made of diamond, but it can also be in sapphire, tungsten carbide or hard steel. The indenter geometry can vary. The most frequently used is a Berkovich one, but Vickers or spherical indenters are also used.

2.5.1 Measurements

Mechanical properties as hardness and elastic modulus are given by the load-displacements curves measured with the apparatus (Fig. 2.4).

The most useful method is the Oliver and Pharr one. It's described below. It's supposed the unloading can be fit with the following load (P)-displacement (h) relationship:

$$P = B(h - h_f)^m \quad (2.245)$$

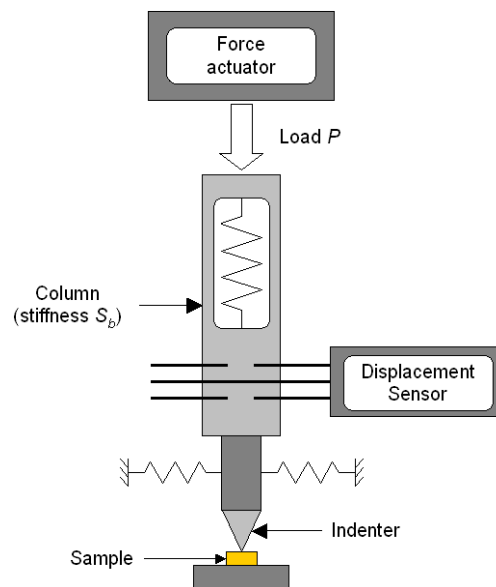


Fig 2.4 Schematic representation of a nanoindenter.

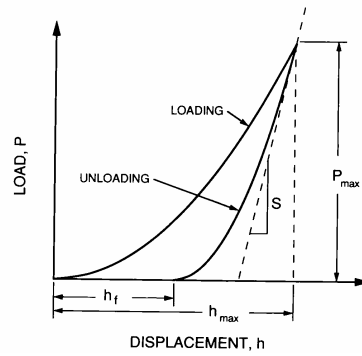


Fig 2.5 Schematic representation of a load-displacement curve recorded during an instrumented indentation test.

where B , m and h_f are determined by a least squares fitting procedure. By differentiating the Eq. (2.245) and evaluating the result at the maximum depth, h_{max} , the contact stiffness is obtained by:

$$S = \left(\frac{dP}{dh} \right)_{h_{max}} = mB(h_{max} - h_f)^{m-1} \quad (2.246)$$

The contact depth is then calculated:

$$h_c = h_{max} - \varepsilon \frac{P_{max}}{S} \quad (2.247)$$

where ε is a constant that depends on the indenter geometry. The projected contact area A is obtained by evaluating the indenter area function f at the depth h_c :

$$A = f(h_c) \quad (2.248)$$

For an ideal Berkovich indenter, $f(h) = 24.56h^2$, but for real indenters, this function is more complex and a calibration is needed. From these values, the hardness can be calculated:

$$H = \frac{P_{max}}{A} \quad (2.249)$$

and the reduced elastic modulus:

$$E_r = \frac{\sqrt{\pi}}{2\beta} \frac{S}{\sqrt{A}} \quad (2.250)$$

where ε is a constant that depends on the indenter geometry. The elastic modulus of the material is finally obtained:

$$E = (1 - \nu^2) \left[\frac{1}{E_r} - \frac{1 - \nu_i^2}{E_i} \right]^{-1} \quad (2.251)$$

where E_i and ν_i are, respectively, the elastic modulus and the Poisson's ratio of the indenter and ν the Poisson's ratio of the tested material.

2.5.2 Dynamic measurements

The Continuous Stiffness Measurement (CSM) is a technique in which stiffness is measured continuously during the loading of the indenter by imposing a small dynamic oscillation on the force (or displacement) signal and measuring the amplitude and phase of the corresponding displacement (or force) signal. It allows measuring the storage and loss moduli characterizing polymers. The oscillation amplitude is as low as the total displacement isn't affected.

With the continuous stiffness, the elastic modulus and the hardness can be continuously calculated.

2.5.3 Specifications

	XP	DCM
Maximum indentation depth	500 μm	15 μm
Displacement resolution	< 0.01 nm	0.2 pm
Maximum load	500 mN	10 mN
Load resolution	50 nN	1 nN

2.5.4 Channels

Contact Area $A(t) = f(h_c(t))$

$$\text{Contact Depth } h_c(t) = h(t) - \varepsilon \frac{P(t)}{S(t)}$$

Displacement Into Surface

$$h(t) = h_{brut}(t) - h_{brut}(t_S) - \delta \times \nu_{th}(t - t_S) - \frac{P_{brut}(t) - P_{brut}(t_S)}{S_b + \Delta S_b}$$

Frame Stiffness S_b

Frame Stiffness Correction ΔS_b

$$H(t) = \frac{P(t)}{A(t)}$$

Hardness

Harmonic Contact Damping ω

$$\text{Harmonic Contact Stiffness } S_{hc}(t) = \left[\frac{1}{S_h(t)} - \frac{1}{S_b(t) + \Delta S_b(t)} \right]^{-1}$$

Harmonic Displacement – Déplacement harmonique du CSM

Harmonic Frame Stiffness – $S_b(t)$

Harmonic Frame Stiffness Correction – $\Delta S_b(t)$

Harmonic Stiffness $h(t)$

Load vs Disp Slope – $\frac{dP}{dh}$

Modulus $E(t) = (1 - \nu^2) \left(\frac{1}{E_r(t)} - \frac{1 - \nu_i^2}{E_i} \right)^{-1}$

2.5.5 Formulas

Area Coefficient i $f(h) = \sum_{i=1}^9 A_i h^{1/2^{i-2}}$

Contact Area From Unload – $A = f(h_c)$

Contact Depth From Unload – $h_c = h_{\max} - \varepsilon \frac{P_{\max}}{S}$

Drift Correction – ν_{th} –

E Average Over Defined Range – $m(E) = \sum_{n=M}^N \frac{E_n}{N - M}$

H Average Over Defined Range – $m(H) = \sum_{n=M}^N \frac{H_n}{N - M}$

Hardness From Unload $H = \frac{P_{\max}}{A}$

Modulus From Unload $E = (1 - \nu^2) \left(\frac{1}{E_r} - \frac{1 - \nu_i^2}{E_i} \right)^{-1}$

Prescribed Loading Rate – \dot{P}/P

α

Reduced Modulus From Unload – $E_r = \frac{\sqrt{\pi}}{2\beta} \frac{S}{\sqrt{A}}$

Stiffness From Unload – $S = \left(\frac{dP}{dh} \right)_{h_{\max}} = mB(h_{\max} - h_f)^{m-1}$

3 Identification of electro-mechanical material properties

The objective of this work is to obtain the mechanical as well as electrical properties of composite actuators/sensors with embedded fibres made of piezoelectric material. The technique is based on the computation of effective properties on a so-called representative volume element. Based on the constituent material properties (electrical and mechanical) and the geometry (mainly the volume fraction of fibres), we derive simple analytical formulae assuming 2D plane stress hypothesis, and d_{31} type actuation.

3.1 Principle of the method

We are interested in the characterization of composite actuators / sensors with embedded piezoelectric fibres. One example of such is the Macro Fibre Composite (Fig. 3.1).

The developments are made for d_{31} type MFCs for which the polarization and the electric field are perpendicular to the plane of the MFC (Fig. 3.2).

The goal is to determine the equivalent homogeneous properties of the composite active layer made of epoxy and PZT. A representative volume element (RVE) is defined as represented in Fig. 3.3.

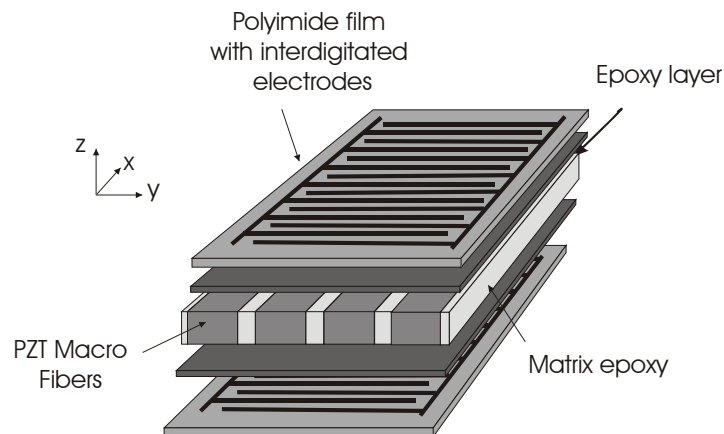


Fig. 3.1 Macro fibre composite.

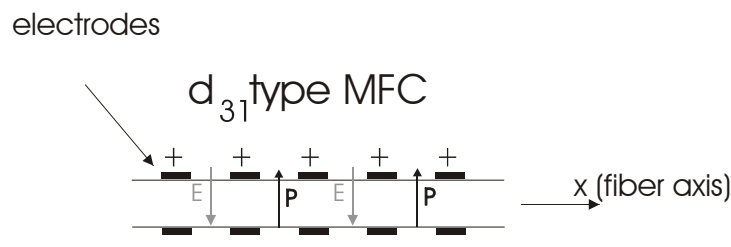


Fig. 3.2 Electric field and polarization for d_{31} type MFCs.

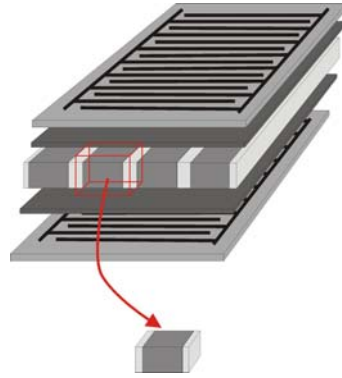


Fig. 3.3 Representative volume element (RVE) for the homogenisation of the active layer

3.2 Mixing rules for piezo fibres used in d_{31} mode

For the modelling, we consider that the actuator is a laminate. For each ply, we assume the plane stress hypothesis ($T_3, T_4, T_5 = 0$). The electric field is assumed to be in the z -direction ($E_2 = E_1 = 0$). In the standard IEEE notations for linear piezoelectricity, this leads to the following form of the constitutive equations:

$$\begin{Bmatrix} S_1 \\ S_2 \\ S_6 \\ D_3 \end{Bmatrix} = \begin{bmatrix} s_{11}^E & s_{21}^E & 0 & d_{31} \\ s_{21}^E & s_{22}^E & 0 & d_{32} \\ 0 & 0 & s_{66}^E & 0 \\ d_{31} & d_{32} & 0 & \varepsilon_{33}^T \end{bmatrix} \begin{Bmatrix} T_1 \\ T_2 \\ T_6 \\ E_3 \end{Bmatrix} \quad (3.1)$$

or alternatively:

$$\begin{Bmatrix} T_1 \\ T_2 \\ T_6 \\ D_3 \end{Bmatrix} = \begin{bmatrix} c_{11}^E & c_{21}^E & 0 & -e_{31} \\ c_{21}^E & c_{22}^E & 0 & -e_{32} \\ 0 & 0 & c_{66}^E & 0 \\ e_{31} & e_{32} & 0 & \varepsilon_{33}^S \end{bmatrix} \begin{Bmatrix} S_1 \\ S_2 \\ S_6 \\ E_3 \end{Bmatrix} \quad (3.2)$$

The objective is to replace the MFC represented in Fig. 3.1 by a multi-layer composite with homogeneous layers as shown in Fig. 3.4. The active layer is homogenized using a representative volume element (RVE, Fig. 3.3). The geometry of the RVE is given in Fig. 3.5.

The approach followed here is the Uniform Field Method (UFM, [3.1]). The principle is to assume that the different quantities (stress, strain, electric field and displacement), are homogeneous in each constituent. Here we denote with a

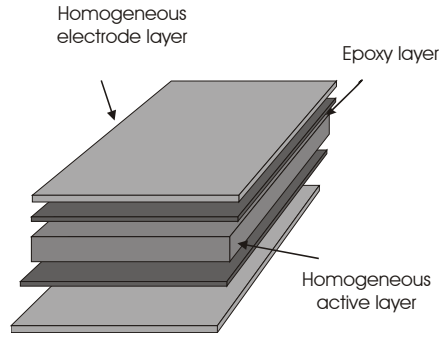


Fig. 3.4 Modelling of a MFC with homogeneous layers.

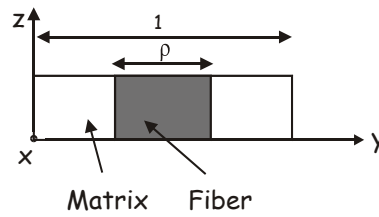


Fig. 3.5 Geometry of the representative volume element (RVE).

superscript p the quantities related to the fibre, and with a superscript m , the quantities related to the matrix. The mean quantity is denoted without superscript. For the geometry given in Fig. 3.5, the following assumptions are made:

$$S_1 = S_1^p = S_1^m \quad (3.3)$$

$$S_2 = \rho S_2^p + (1 - \rho) S_2^m \quad (3.4)$$

$$S_6 = \rho S_6^p + (1 - \rho) S_6^m \quad (3.5)$$

$$D_3 = \rho D_3^p + (1 - \rho) D_3^m \quad (3.6)$$

which means that S_1 is identical in the fibre and the matrix, and the mean quantity is therefore also equal. For the other quantities S_2 , S_6 and D_3 , the value in the fibre and the matrix are different, the mean value is given by a sum weighted by the volume fraction ρ .

For the dual variables, the following assumptions are made:

$$T_1 = \rho T_1^p + (1 - \rho) T_1^m \quad (3.7)$$

$$T_2 = T_2^p = T_2^m \quad (3.8)$$

$$T_6 = T_6^p = T_6^m \quad (3.9)$$

$$E_3 = E_3^p = E_3^m \quad (3.10)$$

The goal is to find the constitutive equations linking the mean values of S_1, S_2, S_6, D_3 to T_1, T_2, T_6, E_3 .

We use the constitutive equations in the form of (3.1):

$$\begin{Bmatrix} S_1 \\ S_2 \\ S_6 \\ D_3 \end{Bmatrix} = \begin{bmatrix} s_{11}^E & s_{21}^E & 0 & d_{31} \\ s_{21}^E & s_{22}^E & 0 & d_{32} \\ 0 & 0 & s_{66}^E & 0 \\ d_{31} & d_{32} & 0 & \varepsilon_{33}^T \end{bmatrix} \begin{Bmatrix} T_1 \\ T_2 \\ T_6 \\ E_3 \end{Bmatrix} \quad (3.11)$$

the procedure to find the homogeneous properties $s_{11}^E, s_{21}^E, s_{22}^E, s_{66}^E, d_{31}, d_{32}, \varepsilon_{33}^T$ is to rewrite the constitutive equations in terms of the fields which are identical in the fibre and the matrix, i.e, in this case : S_1, T_2, T_6, E_3 . This gives:

$$\begin{Bmatrix} T_1 \\ S_2 \\ S_6 \\ D_3 \end{Bmatrix} = \begin{bmatrix} \frac{1}{s_{11}^E} & -\frac{s_{21}^E}{s_{11}^E} & 0 & -\frac{d_{31}}{s_{11}^E} \\ \frac{s_{21}^E}{s_{11}^E} & s_{22}^E - \frac{(s_{21}^E)^2}{s_{11}^E} & 0 & d_{32} - d_{31} \frac{s_{21}^E}{s_{11}^E} \\ 0 & 0 & s_{66}^E & 0 \\ \frac{d_{31}}{s_{11}^E} & d_{32} - d_{31} \frac{s_{21}^E}{s_{11}^E} & 0 & \varepsilon_{33}^T - \frac{d_{31}^2}{s_{11}^E} \end{bmatrix} \begin{Bmatrix} S_1 \\ T_2 \\ T_6 \\ E_3 \end{Bmatrix} \quad (3.12)$$

for each of the quantities in the left hand side, we can write (for example for T_1):

$$T_1 = \rho T_1^p + (1 - \rho) T_1^m \quad (3.13)$$

Replacing T_1, T_1^p and T_1^m using Eq (3.12), and knowing that S_1, T_2, T_6, E_3 are identical in the fibre and the matrix, one gets:

$$\frac{1}{s_{11}^E} = \rho \frac{1}{s_{11}^{Ep}} + (1 - \rho) \frac{1}{s_{11}^{Em}} \quad (3.14)$$

$$\frac{s_{21}^E}{s_{11}^E} = \rho \frac{s_{21}^{Ep}}{s_{11}^{Ep}} + (1 - \rho) \frac{s_{21}^{Em}}{s_{11}^{Em}} \quad (3.15)$$

$$\frac{d_{31}^E}{s_{11}^E} = \rho \frac{d_{31}^{Ep}}{s_{11}^{Ep}} + (1 - \rho) \frac{d_{31}^{Em}}{s_{11}^{Em}} \quad (3.16)$$

Following the same reasoning, all the terms in the matrix of Eq (3.12) follow a linear mixing rule. Rearranging these expressions, we get:

$$s_{11}^E = \frac{s_{11}^{Ep} s_{11}^{Em}}{\rho s_{11}^{Em} + (1-\rho) s_{11}^{Ep}} \quad (3.17)$$

$$s_{21}^E = s_{11}^E \left(\rho \frac{s_{21}^{Ep}}{s_{11}^{Ep}} + (1-\rho) \frac{s_{21}^{Em}}{s_{11}^{Em}} \right) \quad (3.18)$$

$$d_{31}^E = s_{11}^E \left(\rho \frac{d_{31}^p}{s_{11}^{Ep}} + (1-\rho) \frac{d_{31}^m}{s_{11}^{Em}} \right) \quad (3.19)$$

$$s_{22}^E = \frac{(s_{21}^E)^2}{s_{11}^E} + \rho \left(s_{22}^{Ep} - \frac{(s_{21}^{Ep})^2}{s_{11}^{Ep}} \right) + (1-\rho) \left(s_{22}^{Em} - \frac{(s_{21}^{Em})^2}{s_{11}^{Em}} \right) \quad (3.20)$$

$$d_{32}^E = d_{31}^E \frac{s_{21}^E}{s_{11}^E} + \rho \left(d_{32}^p - d_{31}^p \frac{s_{12}^{Ep}}{s_{11}^{Ep}} \right) + (1-\rho) \left(d_{32}^m - d_{31}^m \frac{s_{12}^{Em}}{s_{11}^{Em}} \right) \quad (3.21)$$

$$\varepsilon_{33}^T = \frac{d_{31}^2}{s_{11}^E} + \rho \left(\varepsilon_{33}^{Tp} - \frac{(d_{31}^p)^2}{s_{11}^{Ep}} \right) + (1-\rho) \left(\varepsilon_{33}^{Tm} - \frac{(d_{31}^m)^2}{s_{11}^{Em}} \right) \quad (3.22)$$

$$s_{66}^E = \rho s_{66}^{Ep} + (1-\rho) s_{66}^{Em} \quad (3.23)$$

We can express these relationships in terms of the mechanical constants (electric field $E_3 = 0$) using the following equalities:

$$E_L = \frac{1}{s_{11}^E} \quad (3.24)$$

$$E_T = \frac{1}{s_{22}^E} \quad (3.25)$$

$$\nu_{LT} = -\frac{s_{21}^E}{s_{11}^E} \quad (3.26)$$

$$G_{LT} = \frac{1}{s_{66}^E} \quad (3.27)$$

where E_L denotes the longitudinal Young's modulus (in the fibre direction), E_T the transverse modulus, ν_{LT} is the in-plane Poisson's ration and G_{LT} is the in-plane shear modulus.

Substituting in (3.17-3.23) gives the classical mixing rules for E_L, ν_{LT} and G_{LT} [3.2]:

$$E_L = \rho E_L^p + (1-\rho) E_L^m \quad (3.28)$$

$$\nu_{LT} = \rho \nu_{LT}^p + (1-\rho) \nu_{LT}^m \quad (3.29)$$

$$\frac{1}{G_{LT}} = \frac{\rho}{G_{LT}^p} + \frac{1-\rho}{G_{LT}^m} \quad (3.30)$$

For the transverse modulus, we get:

$$\frac{1}{E_T} = \frac{\rho}{E_T^p} + \frac{1-\rho}{E_T^m} - \frac{(\nu_{LT})^2}{E_L} + \left(\rho \frac{(\nu_{LT}^p)^2}{E_L^p} + (1-\rho) \frac{(\nu_{LT}^m)^2}{E_L^m} \right) \quad (3.31)$$

if we assume $\nu_{LT}^p = \nu_{LT}^m$, we also get the classical mixing rules [3.2]:

$$\frac{1}{E_T} = \frac{\rho}{E_T^p} + \frac{1-\rho}{E_T^m} \quad (3.32)$$

For the piezoelectric constants, we have:

$$d_{31} = \frac{1}{E_L} \left(\rho d_{31p} E_L^p + (1-\rho) d_{31m} E_L^m \right) \quad (3.33)$$

$$d_{32} = -d_{31} \nu_{LT} + \rho \left(d_{32p} + d_{31p} \nu_{LT}^p \right) + (1-\rho) \left(d_{32m} + d_{31m} \nu_{LT}^m \right) \quad (3.34)$$

For a typical piezoelectric material (PZT), $d_{31} = d_{32}$ which leads to expressions identical to the mixing rules for thermal expansion coefficients [3.2, 3.3], d_{31} needs to be replaced by α for the analogy):

$$d_{31} = \frac{1}{E_L} \left(\rho d_{31p} E_L^p + (1-\rho) d_{31m} E_L^m \right) \quad (3.35)$$

$$d_{32} = -d_{31} \nu_{LT} + \rho d_{31p} (1 + \nu_{LT}^p) + (1-\rho) d_{31m} (1 + \nu_{LT}^m) \quad (3.36)$$

e_{31} and e_{32} are given by:

$$\{e_{31} e_{32} 0\} = \{d_{31} d_{32} 0\} \begin{bmatrix} \frac{E_L}{1-\nu_{LT}\nu_{TL}} & \frac{\nu_{LT}E_T}{1-\nu_{LT}\nu_{TL}} & 0 \\ \frac{\nu_{LT}E_T}{1-\nu_{LT}\nu_{TL}} & \frac{E_T}{1-\nu_{LT}\nu_{TL}} & 0 \\ 0 & 0 & G_{LT} \end{bmatrix} \quad (3.37)$$

ν_{TL} is given by:

$$\nu_{TL} = \frac{\nu_{LT} E_T}{E_L} \quad (3.38)$$

We get:

$$e_{31} = \frac{1}{1-\nu_{LT}\nu_{TL}} \left(E_L d_{31} + \nu_{LT} E_T d_{32} \right)$$

$$e_{32} = \frac{1}{1 - \nu_{LT} \nu_{TL}} (\nu_{LT} E_T d_{31} + E_T d_{32}) \quad (3.39)$$

3.3 Evolution of the homogenized properties as a function of the volume fraction of fibres

In order to illustrate the effect of the volume fraction ρ on the effective properties of the active layer, we take the following example:

- Matrix: epoxy ($E = 2.6 \text{ GPa}, \nu = 0.3, \varepsilon_{33r}^T = \frac{\varepsilon_{33}^T}{\varepsilon_0} = 4.25$)
- Fibres: PZT ($E = 54 \text{ GPa}, \nu = 0.31, d_{31} = d_{32} = -185 \cdot 10^{-12} \text{ m/V}, \varepsilon_{33r}^T = \frac{\varepsilon_{33}^T}{\varepsilon_0} = 1850$)

The results are shown in Fig. 3.6 and Fig. 3.7.

It is interesting to look at the evolution of the piezoelectric properties as a function of the volume fraction of fibres. d_{32} is close to linear, whereas d_{31} increases very rapidly and reaches a value comparable to PZT for $\rho = 0.5$ already. For this same

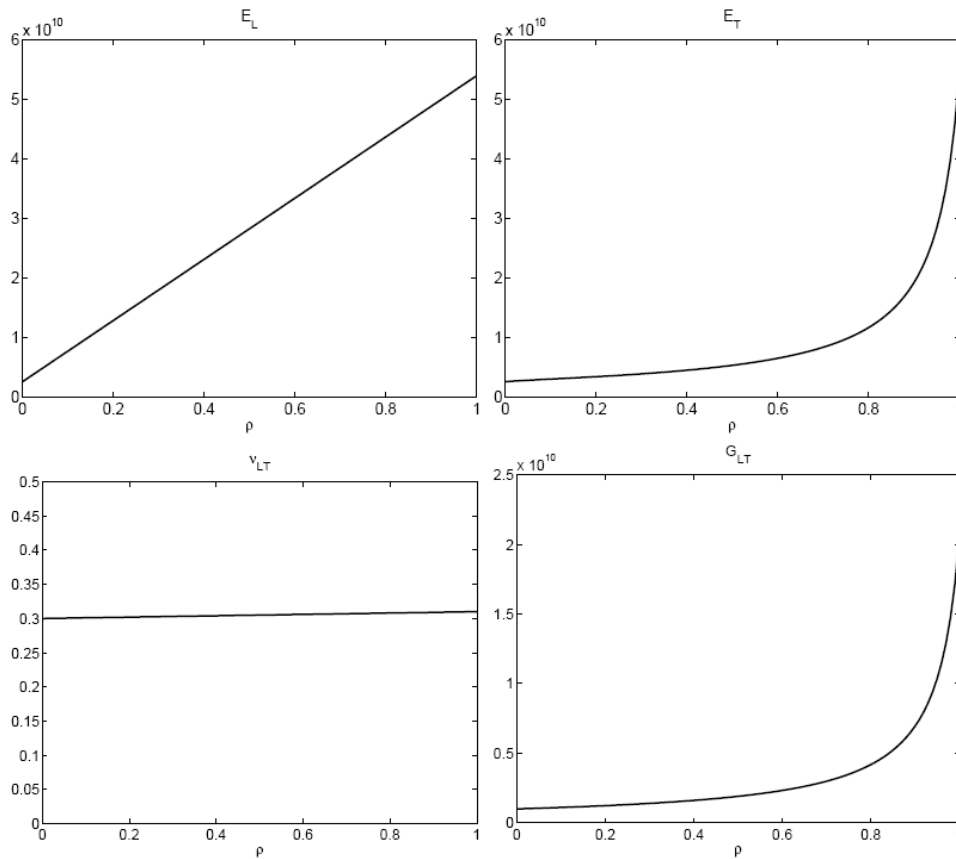


Fig. 3.6 Mechanical properties of the active layer as a function of the volume fraction of fibres.

value, d_{32} is only half of the value for PZT. e_{31} and e_{32} are important because they represent the equivalent in-plane forces of the actuator when a voltage is applied (e_{31} gives the force in the direction of the fibres, and e_{32} gives the force perpendicular). Looking at Eq. (3.39), we see that they are a function of d_{31}, d_{32} but also E_T, E_L and ν_{LT} . The curves show that e_{31} varies almost linearly with the volume fraction, while e_{32} is very small for low volume fractions ($\rho < 0.6$), and increases very rapidly for high volume fraction ($\rho > 0.8$). For low volume fractions, the actuator is almost unidirectional (force acting along the fibres only).

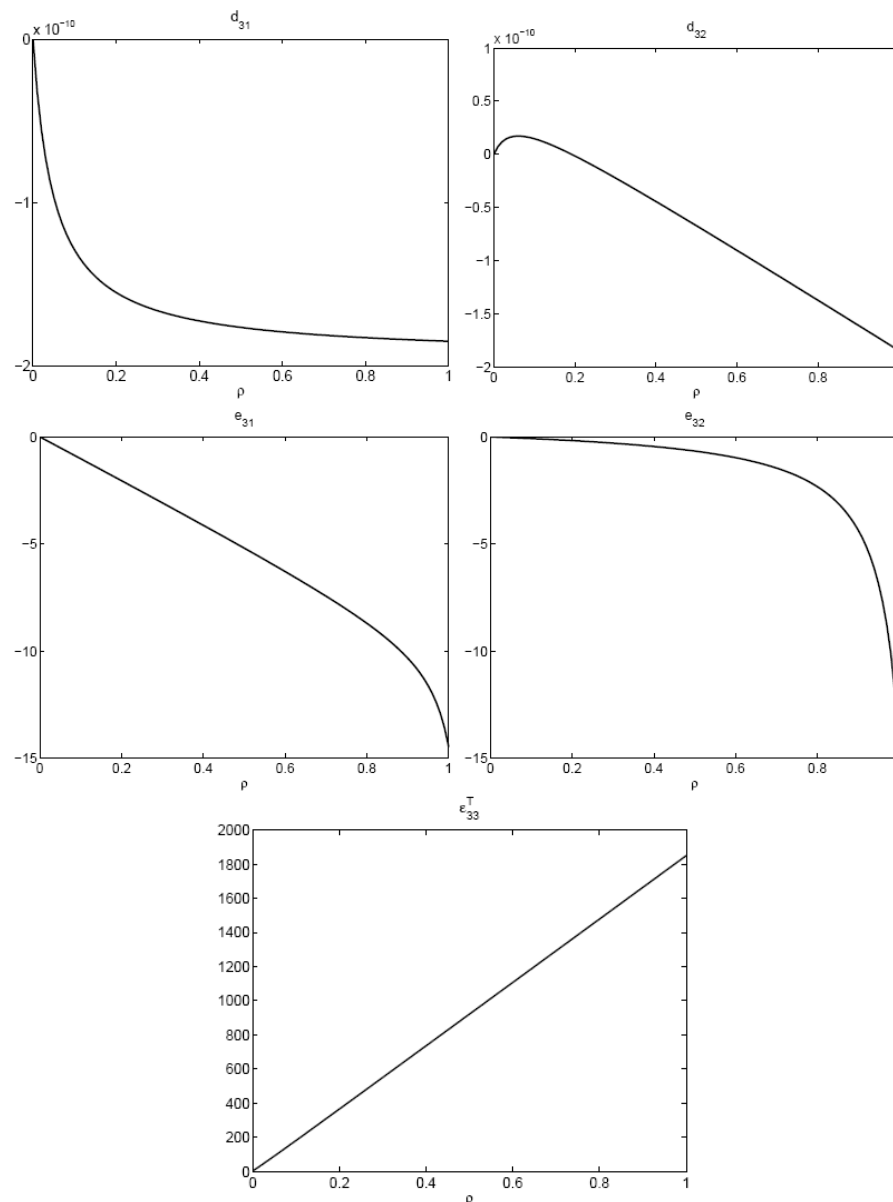


Fig. 3.7 Electrical properties of the active layer as a function of the volume fraction of fibres.

3.4 Homogenized properties of commercial MFC actuators

As a final result, we give the homogenized values for the MFC manufactured by Smart Materials [3.4] (Type P2). The geometry of the RVE is given in Fig. 3.8. The homogenized part is only the active part of thickness 180 microns.

The properties of the piezoelectric material (PZT 5A1 – Navy Type II) are given by the manufacturer (Ceramtec, Table 3.1). The properties of the epoxy are given by Smart-Material (the relative permittivity is found on the internet for a typical epoxy). The full material properties of the PZT are found from Table 3.1 using the following relationships:

$$s_{55}^E = \frac{1}{c_{55}^D(1-k_{15}^2)} \quad (3.40)$$

$$s_{12}^E = -s_{11}^E + \frac{2d_{31}^2}{k_p^2 \epsilon_{33}^T} \quad (3.41)$$

$$s_{66}^E = \frac{s_{11}^E - s_{12}^E}{2} \quad (3.42)$$

$$\epsilon_{11}^T = \frac{d_{15}^2}{s_{55}^E k_{15}^2} \quad (3.43)$$

We also assume $s_{44}^E = s_{55}^E$, $\epsilon_{22}^T = \epsilon_{11}^T$, and $\nu_{13} = 0.38$.

This gives us the full compliance matrix under constant electric field S_E . We can easily find the material properties given in Table 3.2 for the PZT-5A1. The material properties for epoxy are given in Table 3.3.

The homogeneous properties of the active layer are given in Table 3.4. The volume fraction is 0.8654 (see Fig. 3.8). The value of the capacitance of the active layer is computed using the following relationship:

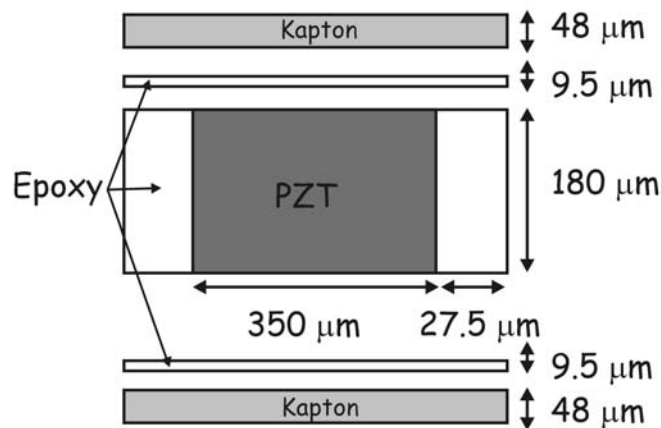


Fig. 3.8 Geometry of the RVE of a d_{31} MFC manufactured by Smart Material [3.4].

$$C = \Omega \frac{\epsilon_{33}^T}{h} \quad (3.44)$$

Where Ω is the area, and h is the thickness of the active layer (here 180 μm). The capacitance is computed for the different types of d_{31} MFCs manufactured by Smart-Material in Table 3.5. The value is compared to an approximate value given in the datasheet. The concordance is satisfactory. The MFC-types only differ in their size (area Ω).

Table 3.1 Properties of piezoelectric material (CeramTec datasheet).

Piezoceramic	Symbol	unit	SP4	5A1	5H2
DoD Standard 1376A (SH)			Type I	Type II	Type VI
Electrical Properties					
Permittivity /1kHz	$\epsilon_{33}^T/\epsilon_0$		1300	1850	3800
Dielectric dissipation factor/ 1kHz	$\tan \delta$		0.003	0.012	0.016
Curie temperature	T_c	$^{\circ}\text{C}$	325	335	215
Electromechanical Properties					
Coupling factors	k_p k_{31} k_{33} k_t k_{15}		0.57 0.31 0.68 0.50 0.65	0.62 0.33 0.72 0.48 0.74	0.65 0.38 0.74 0.51 0.73
Piezoelectric charge coefficients	d_{33} $-d_{31}$ d_{15}	10^{-12} C/N	310 130 455	440 185 560	680 275 770
Piezoelectric voltage coefficients	g_{33}	10^{-3} Vm/N	26.9	25.5	19
Frequency constants	N_p N_t N_1 N_3	kHz mm	2210 2000 1480 1340	2020 2030 1325 1250	1960 1885 1420 1290
Mechanical Properties					
compliance	S_{11}^E S_{33}^E	10^{-12} m ² /N	14.9 18.1	18.5 20.7	15.8 22.9
stiffness	C_{33}^D C_{55}^D	10^{10} N/m ²	15.9 4.8	15.7 6.5	15.2 6.1
Mechanical Quality Factor	Q_m		500	80	75

Table 3.2 Properties of piezoelectric material derived from CeramTec datasheet.

$E_1 = E_2$	54.05	GPa
E_3	48.31	GPa
$G_{23} = G_{31}$	14.70	GPa
G_{12}	38.27	GPa
ν_{12}	0.41	
$\nu_{23} = \nu_{13}$	0.38	
$d_{31} =$	-185	$10^{-12}C/N$
$d_{32} =$	-185	$10^{-12}C/N$
$d_{33} =$	440	$10^{-12}C/N$
$\varepsilon_{11}^T =$	1902	(relative)
$\varepsilon_{22}^T =$	1902	(relative)
$\varepsilon_{33}^T =$	1850	(relative)

Table 3.3 Properties of the epoxy.

E	2.9	GPa
ν	0.3	
$\varepsilon^T =$	4	(relative)

Table 3.4 Homogenized properties for Smart-Material MFCs (d_{31} type).

E_L	47.11	GPa
E_T	16.88	GPa
G_{LT}	6.93	GPa
ν_{LT}	0.40	
$d_{31} =$	-183	$10^{-12}C/N$
$d_{32} =$	-153	$10^{-12}C/N$
$\varepsilon_{33}^T =$	1597	(relative)

Table 3.5 Comparison of Capacitance (computed) with approximate values given in the datasheet.

MFC-Type	Computed capacitance (nF)	Datasheet capacitance (nF)
M8528 P2	187	171
M8507 P2	47	45
M8503 P2	20	17
M2814 P2	30	26
M2807 P2	15	12

3.5 Validation on an experimental setup

The homogeneous properties obtained here will be used in a validation exercise. It consists in a cylindrical composite boom equipped with M8528 P2 actuators / sensors (Fig. 3.9). The validation will be described in D4 “Full report on the new theoretical and finite element models for non-linear vibration analysis and their validation”.

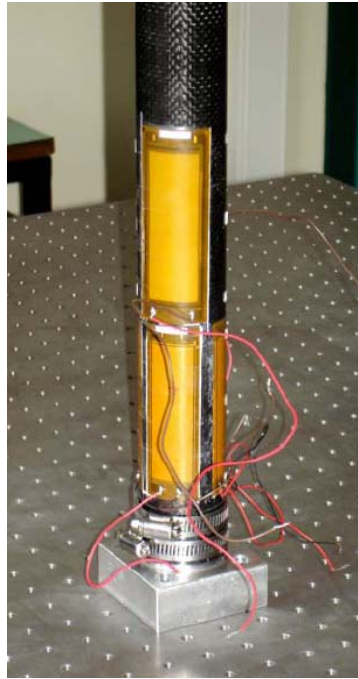


Fig. 3.9 Experimental validation setup.

4 Inverse identification technique

An inverse identification technique based on vibration tests is developed to characterise advanced composite material properties. To minimise the error functional between experimentally measured and numerically obtained dynamic characteristics, the gradient based optimisation (direct) and optimisation based on the planning of experiments and response surface technique (non-direct) have been applied in the identification procedures.

The inverse identification technique developed has been successfully applied to characterise orthotropic elastic material properties of laminated plates, hysteretic material properties of laminated plates, viscoelastic material properties of damping polymers used as a core material in the sandwich panels and piezoelectric material properties.

4.1 Direct optimisation technique

A non-destructive inverse method for estimation of material parameters of laminated active plates with surface bonded piezoelectric sensors and actuators was developed.

A finite element higher-order equivalent single layer numerical model which includes the piezoelectric effect [4.1] is used. The estimation of the material parameters is made by adjusting the response of the numerical model to the experimental response of the structure, consisting in a set of free vibration natural frequencies and modal loss factors. Several techniques for the estimation of mechanical properties of structures have already been presented by several authors. An assessment of the different approaches to the identification of mechanical properties based on free vibration response methods and optimisation techniques in laminated plates are presented in [4.2]. Some methods that also use natural frequencies of vibration for estimation of elastic constants in composite material structures are based on surface response methods [4.3] and model updating techniques [4.4]. Another class of inverse methods combines wave propagation measurements with optimisation techniques and, more recently, with genetic algorithms [4.5,4.6]. Artificial neural networks were also used to solve this type of problems, based on wave propagation measurements [4.7] and also natural frequencies of free vibration for identification of elastic and piezoelectric parameters [4.8,4.9].

As for the simultaneous identification of elastic and piezoelectric parameters in active structures using frequency response measurements, some methods have been presented [4.1, 4.8-4.11].

This work is a generalization of a gradient-based identification technique, which was originally developed for multi-material laminated structures [4.12-4.14], and includes simultaneous identification of both elastic and piezoelectric properties [4.1,4.8,4.9], as well material loss factors. The effect of the adhesive interfaces is studied with the aid of identification simulations where the experiment is substituted by 3D finite element dynamic reference solutions, based upon commercial software. The results of this study are used to gain some insight to the

results of a real identification, based on experimental natural frequencies of free vibration. Identification of damping properties, based on a hysteretic damping model using the complex eigenvalue approach is also performed, where experimental data for this case was taken from the literature.

4.1.1 Numerical model

The numerical model used is a higher order finite element laminated plate model with cubic expansion of the in-plane displacements in the thickness coordinate and constant transverse displacement through the thickness, as shown in Eq. (4.1) for the laminated plate of Fig. 4.1:

$$\begin{aligned} u(x, y, z, t) &= u_0(x, y, t) + z\theta_x(x, y, t) + z^2u_0^*(x, y, t) + z^3\theta_x^*(x, y, t) \\ v(x, y, z, t) &= v_0(x, y, t) + z\theta_y(x, y, t) + z^2v_0^*(x, y, t) + z^3\theta_y^*(x, y, t) \\ w(x, y, z, t) &= w_0(x, y, t) \end{aligned} \quad (4.1)$$

In Eq. (4.1), u_0 , v_0 and w_0 are the in-plane displacements in the x , y , and z directions, t is the time variable and θ_x and θ_y are the rotations of normals to the mid-plane about the y -axis (anticlockwise) and x -axis (clockwise), respectively. The functions u_0^* , v_0^* , θ_x^* and θ_y^* are higher order terms in the Taylor series expansion, defined also in the mid-plane of the plate.

Full details regarding the model development and implementation for dynamics can be found in [4.15], while its extension to account for the piezoelectric effect is described in detail in [4.1].

For each lamina (Fig. 4.2) in the laminate, the 3D constitutive equations for the orthotropic piezoelectric material with thickness polarization are represented in Eq. (4.2), in the local principal material axes [4.16,4.17]

$$\begin{aligned} \begin{Bmatrix} \sigma_{11} \\ \sigma_{22} \\ \sigma_{33} \\ \sigma_{23} \\ \sigma_{13} \\ \sigma_{12} \end{Bmatrix} &= \begin{bmatrix} Q_{11} & Q_{12} & Q_{13} & 0 & 0 & 0 \\ Q_{12} & Q_{22} & Q_{23} & 0 & 0 & 0 \\ Q_{13} & Q_{23} & Q_{33} & 0 & 0 & 0 \\ 0 & 0 & 0 & Q_{44} & 0 & 0 \\ 0 & 0 & 0 & 0 & Q_{55} & 0 \\ 0 & 0 & 0 & 0 & 0 & Q_{66} \end{bmatrix}^E \begin{Bmatrix} \epsilon_{11} \\ \epsilon_{22} \\ \epsilon_{33} \\ \gamma_{23} \\ \gamma_{13} \\ \gamma_{12} \end{Bmatrix} - \begin{bmatrix} 0 & 0 & e_{31} \\ 0 & 0 & e_{32} \\ 0 & 0 & e_{33} \\ 0 & e_{24} & 0 \\ e_{15} & 0 & 0 \\ 0 & 0 & 0 \end{bmatrix} \begin{Bmatrix} E_1 \\ E_2 \\ E_3 \end{Bmatrix} \\ \begin{Bmatrix} D_1 \\ D_2 \\ D_3 \end{Bmatrix} &= \begin{bmatrix} 0 & 0 & 0 & 0 & e_{15} & 0 \\ 0 & 0 & 0 & e_{24} & 0 & 0 \\ e_{31} & e_{32} & e_{33} & 0 & 0 & 0 \end{bmatrix} \begin{Bmatrix} \epsilon_{11} \\ \epsilon_{22} \\ \epsilon_{33} \\ \gamma_{23} \\ \gamma_{13} \\ \gamma_{12} \end{Bmatrix} + \begin{bmatrix} \epsilon_{11} & 0 & 0 \\ 0 & \epsilon_{22} & 0 \\ 0 & 0 & \epsilon_{33} \end{bmatrix}^S \begin{Bmatrix} E_1 \\ E_2 \\ E_3 \end{Bmatrix} \end{aligned} \quad (4.2)$$

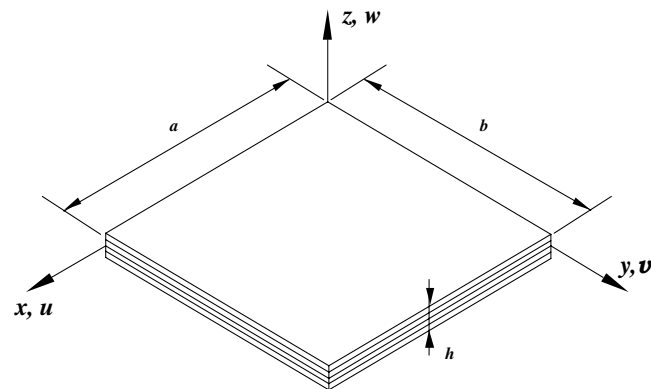


Fig. 4.1 Laminated plate in global reference system.

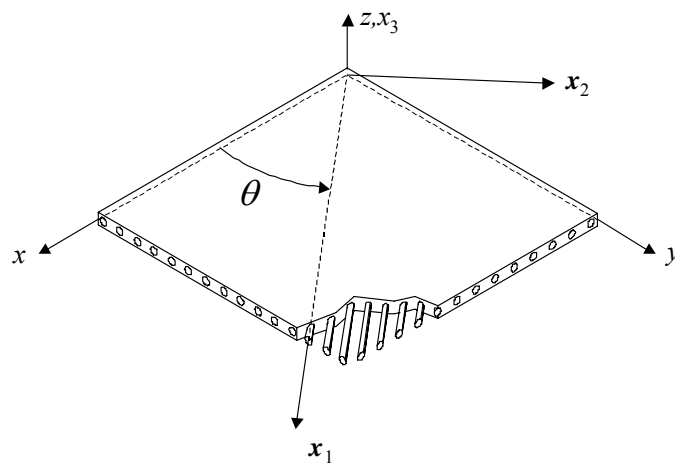


Fig. 4.2 Lamina in local coordinate system.

In the constitutive relation of Eq. (4.2), σ_{ij} are stress components, ε_{ij} and γ_{ij} are deformation components, e_{ij} are the piezoelectric coefficients, E_i and D_i are the electric field and electric displacement components, respectively, ε_{ij}^S are the dielectric coefficients measured at constant strain and Q_{ij}^E are the material stiffness coefficients, measured at constant electric field.

Imposing the plane stress condition ($\sigma_{33} = 0$), Eq. (4.2) is modified accordingly to obtain:

$$\begin{aligned}
\begin{Bmatrix} \sigma_{11} \\ \sigma_{22} \\ \sigma_{23} \\ \sigma_{13} \\ \sigma_{12} \end{Bmatrix} &= \begin{bmatrix} Q_{11}^* & Q_{12}^* & 0 & 0 & 0 \\ Q_{12}^* & Q_{22}^* & 0 & 0 & 0 \\ 0 & 0 & Q_{44} & 0 & 0 \\ 0 & 0 & 0 & Q_{55} & 0 \\ 0 & 0 & 0 & 0 & Q_{66} \end{bmatrix}^E \begin{Bmatrix} \varepsilon_{11} \\ \varepsilon_{22} \\ \gamma_{23} \\ \gamma_{13} \\ \gamma_{12} \end{Bmatrix} - \begin{bmatrix} 0 & 0 & e_{31}^* \\ 0 & 0 & e_{32}^* \\ 0 & e_{24} & 0 \\ e_{15} & 0 & 0 \\ 0 & 0 & 0 \end{bmatrix} \begin{Bmatrix} E_1 \\ E_2 \\ E_3 \end{Bmatrix} \\
\begin{Bmatrix} D_1 \\ D_2 \\ D_3 \end{Bmatrix} &= \begin{bmatrix} 0 & 0 & 0 & e_{15} & 0 \\ 0 & 0 & e_{24} & 0 & 0 \\ e_{31}^* & e_{32}^* & 0 & 0 & 0 \end{bmatrix} \begin{Bmatrix} \varepsilon_{11} \\ \varepsilon_{22} \\ \gamma_{23} \\ \gamma_{13} \\ \gamma_{12} \end{Bmatrix} + \begin{bmatrix} \epsilon_{11} & 0 & 0 \\ 0 & \epsilon_{22} & 0 \\ 0 & 0 & \epsilon_{33}^* \end{bmatrix}^S \begin{Bmatrix} E_1 \\ E_2 \\ E_3 \end{Bmatrix}
\end{aligned} \quad (4.3)$$

In Eq. (4.3), Q_{ij}^{*E} , e_{3i}^* and ϵ_{33}^{*S} are the modified stiffness, piezoelectric and dielectric coefficients due to the plane stress assumption:

$$\begin{aligned}
Q_{ij}^{*E} &= Q_{ij}^E - \frac{Q_{i3}^E Q_{j3}^E}{Q_{33}^E} \\
e_{3i}^* &= e_{3i} - e_{33} \frac{Q_{i3}^E}{Q_{33}^E} \quad i = 1..2 \\
\epsilon_{33}^{*S} &= \epsilon_{33}^S + \frac{e_{33}^2}{Q_{33}^E}
\end{aligned} \quad (4.4)$$

The plane stress coefficients Q_{ij}^{*E} in Eq. (4.3) can be expressed in terms of the non-dimensional material parameters of Eq. (4.5):

$$\mathbf{Q}^{*E} = \frac{E_1}{8\alpha_0} \begin{bmatrix} 8 & \alpha_4 - \alpha_3 & 0 & 0 & 0 \\ \alpha_4 - \alpha_3 & 8 - 2\alpha_2 & 0 & 0 & 0 \\ 0 & 0 & \alpha_8 - \alpha_9 & 0 & 0 \\ 0 & 0 & 0 & \alpha_8 + \alpha_9 & 0 \\ 0 & 0 & 0 & 0 & \frac{1}{2}(8 - \alpha_2 - 3\alpha_3 - \alpha_4) \end{bmatrix} \quad (4.5)$$

The non-dimensional parameters are defined in terms of the engineering constants as shown in Eq. (4.6), where $\alpha_0 = 1 - \nu_{12}^2 E_2/E_1$.

$$\begin{aligned}
\alpha_2 &= 4 - 4E_2/E_1 \\
\alpha_3 &= 1 + (1 - 2\nu_{12})E_2/E_1 - 4\alpha_0 G_{12}/E_1 \\
\alpha_4 &= 1 + (1 + 6\nu_{12})E_2/E_1 - 4\alpha_0 G_{12}/E_1 \\
\alpha_5 &= (8 - \alpha_2 - \alpha_3 - \alpha_4)/2 \\
\alpha_8 &= 4(G_{13} + G_{23})\alpha_0/E_1 \\
\alpha_9 &= 4(G_{13} - G_{23})\alpha_0/E_1
\end{aligned} \tag{4.6}$$

The engineering constants E_1 and E_2 in Eq. (4.6) are the Young's modulus in the principal material directions x_1 and x_2 , respectively (Fig. 4.2), while G_{12} , G_{13} and G_{23} are the transverse shear modulus in planes $x_1 - x_2$, $x_1 - x_3$ and $x_2 - x_3$, respectively and ν_{12} is the major Poisson's ratio. These engineering constants can be retrieved from the non-dimensional parameters using the following inverse relations:

$$\begin{aligned}
E_2/E_1 &= (4 - \alpha_2)/4 \\
G_{12}/E_1 &= (8 - \alpha_2 - 3\alpha_3 - \alpha_4)/(16\alpha_0) \\
\nu_{12} &= (\alpha_4 - \alpha_3)/(8 - 2\alpha_2) \\
G_{13}/E_1 &= (\alpha_8 + \alpha_9)/(8\alpha_0) \\
G_{23}/E_1 &= (\alpha_8 - \alpha_9)/(8\alpha_0) \\
\alpha_0 &= 1 - \frac{(\alpha_4 - \alpha_3)^2}{16(4 - \alpha_2)}
\end{aligned} \tag{4.7}$$

For the case of viscoelastic materials, the engineering constants are taken to be complex:

$$\begin{aligned}
E_1 &= E'_1 (1 + \eta_{E_1} i) \\
E_2 &= E'_2 (1 + \eta_{E_2} i) \\
G_{12} &= G'_{12} (1 + \eta_{G_{12}} i) \\
G_{13} &= G'_{13} (1 + \eta_{G_{13}} i) \\
G_{23} &= G'_{23} (1 + \eta_{G_{23}} i) \\
\nu_{12} &= \nu'_{12} (1 + \eta_{\nu_{12}} i)
\end{aligned} \tag{4.8}$$

where the prime (') quantities are storage moduli, η denotes material loss factors and $i = \sqrt{-1}$. It is worthwhile noting that in Eq. (4.8) both storage moduli and loss factors are, in general, frequency dependent. It is assumed that these quantities are constant over the frequency range of interest hence a hysteretic type of damping model was developed, which proved to be efficient.

Applying a rotational transformation from the principal material axes (x_1, x_2, x_3) to the global reference system (x, y, z) , one obtains the constitutive equations in this later coordinate system [4.1].

For a laminate made of several composite and piezoelectric material laminas, the constitutive equations are obtained after integration is carried out in the laminate thickness coordinate. The equations of motion for free vibration are then obtained using the finite element method through an eight noded serendipity plate element with the nine degrees of freedom per node, corresponding to the terms in the expansion of the displacement field in Eq. (4.1). As for the piezoelectric degrees of freedom, the electric field is assumed to be constant within each of the element's piezoelectric layers. With these considerations in mind, one arrives at the following global equilibrium equations through assembly of the element equations:

$$\begin{bmatrix} \mathbf{M}_{uu} & \mathbf{0} \\ \mathbf{0} & \mathbf{0} \end{bmatrix} \begin{Bmatrix} \ddot{\mathbf{u}} \\ \ddot{\boldsymbol{\phi}} \end{Bmatrix} + \begin{bmatrix} \mathbf{K}_{uu} & \mathbf{K}_{u\phi} \\ \mathbf{K}_{u\phi}^T & \mathbf{K}_{\phi\phi} \end{bmatrix} \begin{Bmatrix} \mathbf{u} \\ \boldsymbol{\phi} \end{Bmatrix} = \mathbf{0} \quad (4.9)$$

where \mathbf{u} , $\ddot{\mathbf{u}}$, $\boldsymbol{\phi}$ and $\ddot{\boldsymbol{\phi}}$ are mechanical degrees of freedom and corresponding accelerations, electric potential and corresponding second time derivatives, respectively. \mathbf{M}_{uu} and \mathbf{K}_{uu} are the mass and stiffness matrices, respectively, corresponding to purely mechanical behaviour, while $\mathbf{K}_{\phi\phi}$ is dielectric stiffness matrix and $\mathbf{K}_{u\phi}$ is the stiffness matrix that corresponds to the coupling between the mechanical and the piezoelectric effects.

The electric degrees of freedom are condensed and considering harmonic vibrations, one obtains the eigenvalue problem:

$$(\mathbf{K}^* - \lambda_n \mathbf{M}) \mathbf{u}_n = \mathbf{0} \quad (4.10)$$

where \mathbf{u}_n is the eigenvector corresponding to the eigenvalue λ_n and $\mathbf{K}^* = \mathbf{K}_{uu} - \mathbf{K}_{u\phi} \mathbf{K}_{\phi\phi}^{-1} \mathbf{K}_{u\phi}^T$ is the condensed stiffness matrix. In case of viscoelastic behaviour, the condensed stiffness matrix \mathbf{K}^* is complex, which in turn leads to complex eigenvectors \mathbf{u}_n and eigenvalues $\lambda_n = \omega_n^2 (1 + \eta_n i)$, where ω_n is the n^{th} natural frequency and η_n is the corresponding modal loss factor.

It is worthwhile noting that when electroded surfaces exist in a given patch or layer, equipotential conditions are imposed before condensing the electric degrees of freedom.

In order to minimize errors associated with modelling boundary conditions, we are only concerned with completely free plates, thus a shift is applied to the global stiffness matrix in order to ensure positive definiteness [4.18].

4.1.2 Gradient based optimisation

In this approach, the parameter estimation technique consists on minimising the difference between the response of the physical system and the finite element numerical model that simulates the system response as a function of the elastic and piezoelectric coefficients. The response consists of a set of natural frequencies of free vibration of the plate and corresponding modal loss factors, which are measured experimentally and then used to fit the corresponding response of the numerical model, thus determining the parameters for the best fit.

The error estimator used in this work is of weighted least squares type:

$$\Phi = \sum_{n=1}^I w_n^{(\omega)} \left(1 - \frac{\omega_n^2}{\tilde{\omega}_n^2} \right)^2 + \sum_{n=1}^I w_n^{(\eta)} \left(1 - \frac{\eta_n}{\tilde{\eta}_n} \right)^2 \quad (4.11)$$

where $\tilde{\omega}_n$ are the experimental eigenfrequencies, $w_n^{(\omega)}$ and $w_n^{(\eta)}$ are weights used to express the confidence level in each one of the experimental eigenfrequencies and modal loss factors, respectively, and I is the total number of modes used.

The problem is stated as the constrained minimization of the error estimator in Eq. (4.11), as follows:

$$\begin{aligned} \min \quad & \Phi(\mathbf{b}) \geq 0 \\ \text{s.t.} \quad & \mathbf{g}(\mathbf{b}) \leq \mathbf{0} \\ & \mathbf{b}^{\ell} \leq \mathbf{b} \leq \mathbf{b}^u \end{aligned} \quad (4.12)$$

Side constraints \mathbf{b}^{ℓ} and \mathbf{b}^u in Eq. (4.12) are applied to the design vector as well as additional constraints \mathbf{g} in order to ensure positive definiteness of the constitutive elastic matrices of all materials present in the structure.

In Eq. (4.12), \mathbf{b} is the vector of design variables:

$$\mathbf{b} = \left\{ \bar{\mathbf{a}}_1^T, \dots, \bar{\mathbf{a}}_m^T, \mathbf{b}_p^1, \dots, \mathbf{b}_p^{mp} \right\}^T \quad (4.13)$$

where m is the number of different materials and $mp \leq m$ is the number of different piezoelectric materials in the laminate. The first components of the design vector are the non-dimensional viscoelastic material constants, which for a particular material i can be written as:

$$\bar{\mathbf{a}}^i = \left\{ E_1^i / {}^0E_1^i, \alpha_2^i, \alpha_3^i, \alpha_4^i, \alpha_8^i, \alpha_9^i \right\}^T \quad (4.14)$$

where ${}^0E_1^i$ represents the initial estimate for E_1^i . The piezoelectric design variables for material i are expressed as:

$$\mathbf{b}_p^i = \{e_{31}^{*i}, e_{32}^{*i}\}^T \quad (4.15)$$

The components of the constraint vector for material i can be written in terms of the non-dimensional material parameters as:

$$\mathbf{g}^i \equiv \left\{ -\bar{\alpha}_1^i, \frac{\bar{\alpha}_2^i}{\bar{\alpha}_2^i - 4}, \frac{8 - \bar{\alpha}_2^i - 3\bar{\alpha}_3^i - \bar{\alpha}_4^i}{-16\bar{\alpha}_0^i}, \left| \frac{\bar{\alpha}_4^i - \bar{\alpha}_3^i}{8 - 2\bar{\alpha}_2^i} \right| - \sqrt{\frac{4}{4 - \bar{\alpha}_2^i}}, \frac{\bar{\alpha}_5^i - \bar{\alpha}_6^i}{-8\bar{\alpha}_0^i}, \frac{\bar{\alpha}_5^i + \bar{\alpha}_6^i}{-8\bar{\alpha}_0^i} \right\}^T \quad (4.16)$$

Since the design variables in Eq. (4.14) are complex quantities when viscoelastic material behaviour is envisaged, their real and imaginary parts are used as independent design variables in the minimization process. Regarding the constraint vector in Eq. (4.16), it is only meaningful for the case of purely elastic behaviour, i.e., it is only used for the estimation of the storage moduli.

The numerical optimisation technique integrates methods for unconstrained problems, based on Gauss-Newton algorithm with the Feasible Arc Interior Point Algorithm (FAIPA) for constrained optimisation [4.19,4.20], using analytical and semi-analytical sensitivities [4.1].

For the sensitivity calculations, one obtains the following expression for the derivative of the objective function with respect to the design variables:

$$\frac{\partial \Phi}{\partial \mathbf{b}} = -2 \sum_{n=1}^I \mathbf{w}_n^{(\omega)} \left(1 - \frac{\omega_n^2}{\tilde{\omega}_n^2} \right) \frac{1}{\tilde{\omega}_n^2} \frac{\partial \omega_n^2}{\partial \mathbf{b}} - 2 \sum_{n=1}^I \mathbf{w}_n^{(\eta)} \left(1 - \frac{\eta_n}{\tilde{\eta}_n} \right) \frac{1}{\tilde{\eta}_n} \frac{\partial \eta_n}{\partial \mathbf{b}} \quad (4.17)$$

where

$$\frac{\partial \eta_n}{\partial \mathbf{b}} = \frac{1}{\omega_n^2} \left(\frac{\partial \Im(\lambda_n)}{\partial \mathbf{b}} - \eta_n \frac{\partial \Re(\lambda_n)}{\partial \mathbf{b}} \right) \quad (4.18)$$

and, for the case where the mass matrix does not depend on the design variables:

$$\frac{\partial \lambda_n}{\partial \mathbf{b}} = \frac{\mathbf{u}_n^T \frac{\partial \mathbf{K}^*}{\partial \mathbf{b}} \mathbf{u}_n}{\mathbf{u}_n^T \mathbf{M} \mathbf{u}_n} \quad (4.19)$$

Due to the different order of magnitude of the sensitivities of the eigenfrequencies to different types of possible design variables (viscoelastic and piezoelectric), a three-phase identification procedure is suggested [4.1]. In the first stage (Phase I), only the viscoelastic parameters associated with the base composite laminate are identified. In Phase II the sensors and actuators are exteriorly bonded to the surfaces of the laminate and the second phase of the identification takes place for the estimation of the elastic parameters of the piezoelectric material, in closed circuit conditions (in order to obtain the stiffness parameters at constant electric

field). Finally, in Phase III estimation of only the piezoelectric parameters is conducted in open circuit.

It is worthwhile noting that the modified dielectric parameter ϵ_{33}^{*S} can be expressed in terms of the modified piezoelectric parameters, the elastic parameters and the dielectric coefficient measured at constant stress ϵ_{33}^T (obtainable from manufacturer data). In fact, using the conversion relation [4.21] between dielectric coefficients at constant stress and constant strain $\epsilon_{ij}^S = \epsilon_{ij}^T - e_{ik} Q_{kl}^{E^{-1}} e_{jl}$ together with the relations in Eq. (4.4), one arrives at the following expression:

$$\epsilon_{33}^{*S} = \epsilon_{33}^T + 2 \frac{e_{31}^* e_{32}^* \nu'_{12}}{E'_1} - \frac{e_{31}^{*2}}{E'_1} - \frac{e_{32}^{*2}}{E'_2} \quad (4.20)$$

Since we can either use the values of ϵ_{33}^T provided by manufacturers or obtain these values through capacitance measurements [4.22], no additional design variables are needed.

4.1.3 Piezo/elastic applications

With the purpose of validating the method for the identification of elastic and piezoelectric parameters and evaluating the effect of the adhesive interfaces between the piezoelectric material and the base structure, two identification simulations are presented. The results of these simulations are then compared with the results of a real identification, conducted on a similar structure.

The plate used in all situations is made of 12 layers of unidirectional T300 carbon fibres in epoxy resin, with stacking sequence $[0^\circ/90^\circ/+45^\circ/-45^\circ/0^\circ/90^\circ]_s$ and dimensions $279.0 \times 199.5 \times 1.6 \text{ mm}^3$. The plate is instrumented with 9 piezoelectric patches of dimensions $50 \times 30 \times 0.5 \text{ mm}^3$, glued to one of the outer surfaces, and 15 natural frequencies of free vibration are used in the identifications.

For the simulations the piezoelectric material is PZT-5J, whose properties are assumed to be known (extracted from material tables), and for the experimental identification PIC-151 is used. For this last material only some reference values provided by the manufacturer are known and will be used to check the identification results. In both cases surface electrodes are present.

4.1.3.1 Simulations

For the simulations, the experimental natural frequencies of free vibration are the natural frequencies obtained through a 3D numerical model [4.23] of both plate and patches. To model the plate, a hexahedral 20 noded solid finite element for laminates is used (SOLID191) and for the piezoelectric material a similar 20-node element, which includes the piezoelectric effect, is used (SOLID226). The reference 3D finite element model is shown in Fig. 4.3.

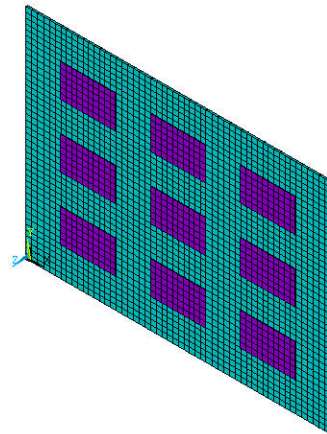


Fig. 4.3 ANSYS 3D finite element model.

For the numerical 2D identification model a 17×14 mesh is used and the results of the identification process are presented in Table 4.1. The natural frequencies produced by the 3D numerical model are presented in Table 4.2 along with residuals r_i obtained after identification. Residuals are defined in Eq. (4.18), where f_i and \tilde{f}_i are the natural frequencies [Hz] produced by the numerical model after identification and the corresponding experimental frequencies [Hz] (or, in the case of simulations, the ones produced by the 3D numerical model), respectively.

$$r_i = (\tilde{f}_i - f_i) / \tilde{f}_i \times 100 \quad (4.21)$$

Table 4.1 Identified properties for the simulations.

	Carbon T300		PZT-5J		
	Goal	Estimated	Goal	Estimated without glue	Estimated with glue
E'_1 [GPa]	125.0	124.9	61.7	61.5	63.5
E'_2 [GPa]	15.0	15.2	61.7	60.3	50.6
G'_{12} [GPa]	6.0	6.0	24.1	23.8	23.1
G'_{13} [GPa]	8.0	8.5	21.3	25.2	26.5
G'_{23} [GPa]	8.0	8.4	21.3	25.2	26.7
ν'_{12}	0.25	0.24	0.28	0.29	0.36
e_{31}^* [N/Vm]	—	—	-18.9	-18.5	-17.3
e_{32}^* [N/Vm]	—	—	-18.9	-18.6	-13.7
ϵ_{33}^T [10^{-9} F/m]	—	—	23.0	—	—
ρ [kg/m ³]	1600	—	7400	—	—

Table 4.2 Simulated natural frequencies and residuals obtained after identification.

i	Phase I		Phase II		Phase III		Phase II (glue)		Phase III (glue)	
	\tilde{f}_i [Hz]	r_i [%]	\tilde{f}_i [Hz]	r_i [%]	\tilde{f}_i [Hz]	r_i [%]	\tilde{f}_i [Hz]	r_i [%]	\tilde{f}_i [Hz]	r_i [%]
1	88.5	0.03	98.9	0.10	99.0	0.10	98.8	-0.11	98.9	-0.11
2	144.4	0.00	147.8	0.05	149.1	0.04	148.1	0.08	149.1	0.13
3	230.1	0.00	248.9	0.03	250.0	0.02	248.8	-0.02	249.6	-0.00
4	245.9	0.01	254.6	0.03	257.5	0.08	252.3	0.03	254.1	-0.01
5	301.2	0.01	320.6	0.00	322.1	0.02	319.1	-0.13	320.1	-0.17
6	404.2	-0.01	411.5	0.02	415.8	0.02	411.3	0.36	414.5	0.41
7	456.8	-0.01	493.8	-0.00	496.7	0.00	492.4	0.09	494.5	0.08
8	486.1	-0.01	515.5	-0.04	517.6	-0.04	514.8	0.00	516.4	0.01
9	673.7	0.02	698.1	-0.05	704.7	-0.01	691.8	0.00	696.1	-0.06
10	719.9	-0.03	754.9	-0.05	760.6	-0.03	749.5	0.00	753.3	-0.04
11	726.6	0.00	783.9	-0.07	787.2	-0.06	781.9	0.03	784.3	0.03
12	788.9	0.01	797.2	0.04	814.6	0.00	804.3	-0.34	818.4	-0.33
13	848.8	0.01	870.0	-0.01	883.3	-0.03	873.6	-0.08	884.5	-0.13
14	898.1	-0.02	936.7	-0.08	942.5	-0.05	931.5	0.02	935.1	0.03
15	1085.7	-0.02	1105.0	-0.06	1120.6	-0.06	1102.1	0.34	1114.3	0.30

A good agreement is sought between the identified parameters and the true ones, which is reflected in the low frequency residual levels.

To evaluate the effect of the adhesive interfaces in the identified properties, 0.1 mm thick interface layers were inserted in the 3D numerical model. For these layers, 20 noded hexahedral elements (SOLID95) were used, along with an isotropic material with properties $E=0.6$ GPa and $\nu=0.3$. The identified properties are presented in Table 4.1 and the natural frequencies produced by the 3D numerical model along with residuals after identification are presented in Table 4.2. It is worthwhile noting that the interface layers were not included in the 2D identification numerical model, as this model does not allow for the necessary strain discontinuities that arise in the interfaces and, in a practical situation, it is also difficult to determine the characteristics of the adhesive layers with sufficient accuracy.

Observing the results one can conclude that the identified properties are in fact affected by the insertion of these adhesive layers. The Young's modulus and the piezoelectric constants exhibit a noticeable asymmetric behaviour.

4.1.3.2 Experimental verification

In order to verify the applicability of the identification method and the validity of the simulation results, a T300 carbon fibre plate with the characteristics described before has been employed. The piezoelectric patches are of the same dimensions, but the material used in the experimental work is PIC-151, with NiCu *wrap-around* electrodes, as shown in Fig. 4.4. The patches were glued to the plate using commercially available cyanoacrylate glue. Fig. 4.4 also shows the elastic rubber band suspension of the plate, the Brüel & Kjær 8203 impact hammer and the Brüel & Kjær 4190 condenser microphone, used to excite and measure the response of the plate in free vibration. The frequency response functions were

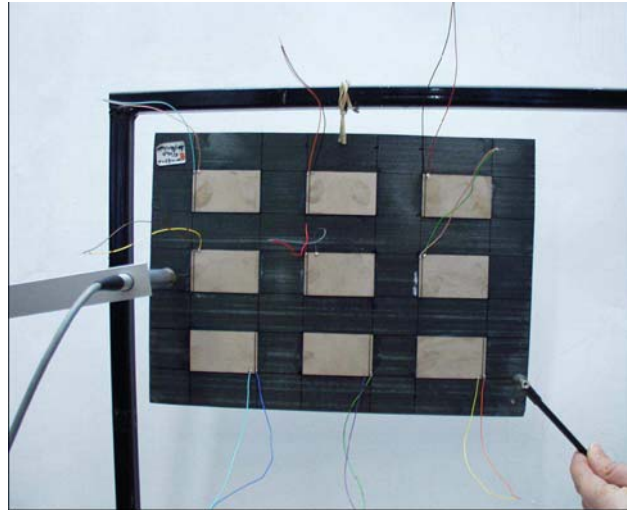


Fig. 4.4 Experimental setup.

obtained through the Brüel & Kjær 2148 spectrum analyser and were curve fitted in order to extract the undamped natural frequencies through ME'scope modal analysis software [4.24].

The identified properties are shown in Table 4.3, along with some available manufacturer (PI Ceramic) data for PIC-151, and experimental frequency results are presented in Table 4.4, along with residuals obtained after identification for each phase.

It is more frequent to find tabled piezoelectric properties in the form of charge coefficients d_{ij} . Using the conversion relation [4.21] between voltage and charge coefficients $d_{ij} = e_{ik} Q_{kj}^{E^{-1}}$ along with Eq. (4.3) we arrive at the following expression that allows for the calculation of these charge coefficients after all material properties have been identified:

$$\begin{aligned} d_{31} &= \frac{e_{31}^*}{E'_1} - \frac{e_{32}^* \nu'_{12}}{E'_1} \\ d_{32} &= \frac{e_{32}^*}{E'_2} - \frac{e_{31}^* \nu'_{12}}{E'_1} \end{aligned} \quad (4.22)$$

The experimental results confirm some of the observed tendencies in the simulations, namely the strong asymmetry exhibited by the Young's modulus and piezoelectric coefficients. However, values obtained for d_{ij} are not in complete disagreement with the values provided by the manufacturer, considering the effect of the glue interfaces.

Table 4.3 Identified properties for the experimental test case (measured values of ρ).

	Carbon T300	PIC 151	
	Estimated	PI Ceramic	Estimated
E'_1 [GPa]	123.9	66.7	56.5
E'_2 [GPa]	16.8	66.7	42.8
G'_{12} [GPa]	5.8	—	17.6
G'_{13} [GPa]	8.5	—	23.8
G'_{23} [GPa]	8.5	—	23.9
ν'_{12}	0.24	0.34	0.36
e^*_{31} [N/Vm]	—	—	-15.5
e^*_{32} [N/Vm]	—	—	-12.8
d_{31} [10^{-12} m/V]	—	-210	-194.5
d_{32} [10^{-12} m/V]	—	-210	-200.7
ϵ^T_{33} [10^{-9} F/m]	—	21.2	—
ρ [kg/m^3]	1610	8036	—

Table 4.4 Experimental natural frequencies and residuals obtained after identification.

i	Phase I		Phase II		Phase III	
	\tilde{f}_i [Hz]	r_i [%]	\tilde{f}_i [Hz]	r_i [%]	\tilde{f}_i [Hz]	r_i [%]
1	87.6	0.06	94.5	0.17	94.5	0.22
2	143.7	0.15	145.1	0.39	146.1	0.38
3	229.2	-0.26	241.9	-0.25	242.8	-0.26
4	247.0	-0.28	249.9	-0.42	251.8	-0.39
5	300.9	-0.20	312.3	-0.19	313.3	-0.20
6	403.8	-0.18	406.0	0.11	409.3	0.16
7	454.1	0.12	479.8	0.05	481.9	0.06
8	484.4	-0.22	503.3	-0.06	505.0	-0.05
9	673.0	0.24	680.7	0.31	684.8	0.39
10	716.3	-0.00	737.7	0.11	741.1	0.20
11	726.5	0.02	762.7	-0.14	765.2	-0.13
12	786.9	-0.02	784.3	-0.36	798.2	-0.37
13	842.1	0.40	851.5	0.18	861.9	0.25
14	896.1	-0.00	910.6	0.27	914.7	0.22
15	1079.7	0.16	1080.1	0.02	1093.2	-0.05

4.1.4 Viscoelastic Applications

In order to assess the capability of the present technique to estimate damping properties, namely the material loss factors, experimental data concerning the first six natural frequencies and modal loss factors of a CFRP 913C-TS plate with unidirectional 0° fibres was taken from [4.25]. The plate dimensions are

252×192×1.155 mm³ and experimentally measured properties obtained through direct methods are given in Table 4.5 along with the estimated parameters obtained by the present inverse technique. In Table 4.6 experimental natural frequencies and modal loss factors are presented along with the residuals obtained after identification.

To aid the interpretation of experimental results, two identification simulations are conducted, where the experimental natural frequencies and modal loss factors are substituted by the ones obtained through the present numerical model for a set of chosen material properties, which are shown in Tables 4.7 and 4.8, where identified results are presented using six and twelve complex natural frequencies.

It can be seen that parameter estimation with only six natural frequencies and corresponding modal loss factor is not recommended for this model, as we are trying to estimate twelve parameters with twelve experimental quantities. Since this is an ill-posed problem, it is usually recommended to use at least twice the experimental data values than the parameters needed to be estimated. Furthermore, the authors of [4.25] mention the use of an accelerometer in some particular situations [4.26]. It is not clear whether or not they used an accelerometer in this particular case. If so, some shift in some particular frequencies might have been produced by the modal mass of the accelerometer and thus leading to poor identification results, especially in Poisson's ratio, which is most sensitive to this effect.

Table 4.5 Identified properties for the experimental test case with damping.

	Direct Measurement [4.25]	Estimated
E'_1 [GPa]	110.0	111.5
E'_2 [GPa]	9.0	8.6
G'_{12} [GPa]	3.9	3.6
G'_{13} [GPa]	—	3.9
G'_{23} [GPa]	—	3.9
ν_{12}	0.34	0.61
η_{E_1} [%]	0.75	0.52
η_{E_2} [%]	5.95	5.47
$\eta_{G_{12}}$ [%]	6.79	8.54
$\eta_{G_{13}}$ [%]	—	85.17
$\eta_{G_{23}}$ [%]	—	99.41
$\eta_{\nu_{12}}$ [%]	—	0.00
ρ [kg/m ³]	1513	—

Also the present technique does not account for frequency dependent material parameters (hysteretic type damping) and, consequently, the estimated parameters can only be regarded as mean values for the frequency range of interest.

4.1.5 Conclusions

An inverse method for estimation of elastic and piezoelectric parameters has been presented along with some results that illustrate the effect of adhesive interfaces on the estimated properties.

Based on the results of the simulation with no adhesive interfaces, one can conclude that the present numerical model is rather accurate for relatively thin structures when compared with the 3D numerical models employed.

Table 4.6 Experimental natural frequencies, modal loss factors and residuals obtained after identification.

i	\tilde{f}_i [Hz]	r_{f_i} [%]	$\tilde{\eta}_i$ [%]	r_{η_i} [%]
1	39.2	0.42	8.33	1.45
2	76.4	0.40	5.36	1.99
3	111.8	-0.55	7.13	-1.31
4	161.9	0.24	0.67	0.22
5	178.6	-0.25	2.31	-0.99
6	215.5	-0.10	5.51	-1.51

Table 4.7 Identified properties for the simulation test cases with damping.

	Goal	Estimated	
		Using 12 frequencies	Using 6 frequencies
E'_1 [GPa]	110.0	110.0	110.4
E'_2 [GPa]	9.0	9.0	9.0
G'_{12} [GPa]	3.9	3.9	3.9
G'_{13} [GPa]	3.9	3.9	3.9
G'_{23} [GPa]	3.9	3.9	3.9
ν'_{12}	0.34	0.33	0.16
η_{E_1} [%]	0.75	0.75	0.77
η_{E_2} [%]	5.95	5.95	5.95
$\eta_{G_{12}}$ [%]	6.79	6.78	6.74
$\eta_{G_{13}}$ [%]	6.79	5.62	5.39
$\eta_{G_{23}}$ [%]	6.79	10.65	5.15
$\eta_{\nu_{12}}$ [%]	6.79	6.94	36.82
ρ [kg/m ³]	1513	—	—

Table 4.8 Natural frequencies, modal loss factors and residuals obtained after identification in the simulation test cases with damping.

i	\tilde{f}_i [Hz]	$\tilde{\eta}_i$ [%]	Using 12 frequencies		Using 6 frequencies	
			r_{f_i} [%]	r_{η_i} [%]	r_{f_i} [%]	r_{η_i} [%]
1	40.9	6.71	-0.01	-0.05	-0.01	-0.69
2	78.5	5.94	-0.01	0.00	-0.23	-0.34
3	114.3	6.38	-0.02	-0.02	-0.11	0.36
4	160.0	0.91	0.02	-0.00	-0.11	-0.26
5	179.0	2.06	0.03	0.06	0.12	0.73
6	217.7	6.09	-0.03	-0.07	-0.23	0.17
7	245.2	4.27	-0.02	-0.03		
8	249.4	6.20	-0.02	0.01		
9	370.3	5.54	-0.04	0.02		
10	426.1	6.08	-0.02	-0.09		
11	439.2	1.17	0.04	-0.03		
12	455.9	5.76	-0.03	0.18		

Results of the simulation including adhesive interfaces in the 3D numerical model allow us to conclude that the effect of these interfaces must not be disregarded in equivalent single layer 2D models and furthermore explain some tendencies observed in the experimental identification that was conducted. However, values obtained for d_{31} and d_{32} are not in disagreement with reference ones provided by the manufacturer, as they are affected by the adhesive interfaces.

The relatively low value obtained for Young's modulus E_1 , and not foreseen through the simulations, may be due to the properties of the particular glue that was used, to the possible thickness variation of the glue interfaces, to the small misalignments of the patches, among others. According to some numerical studies conducted by the authors, the effect of the *wrap-around* electrode configuration does not affect the natural frequencies in a noticeable way, when compared to the standard electrode configuration.

The identification of damping properties has been also attempted with a hysteretic damping model, although the experimental data was taken from the literature and the number of modes available was not clearly enough to conduct a reliable identification. However the trends present in the results show that the current procedure can in fact be used if enough experimental data is available.

As a final conclusion one can say that, in spite of the need for more identification tests, the presented numerical model along with the identified properties guaranties the best fit to the experimental data and frequency range under consideration. In this sense, this model can be used with confidence along with the identified parameters for analysis and control of the tested structure.

4.2 Non-direct optimisation technique

Due to great importance to define performance, reliability and safety requirements for advanced composite products and services, in the last three decades, a considerable effort has been devoted to the studies of their mechanical material properties and several different methods have been developed.

For many orthotropic sheet materials, a measurement method based on low-frequency vibration [4.14,4.27-4.35] is not only the simplest approach, it is also the only approach, which does not suffer from grave difficulties of principle, when the results are used to make predictions in the same range of frequencies. There are two other general methods might be used, static measurements [4.36-4.41] and ultrasonics [4.42-4.46], but neither is wholly appropriate for characterisation of mechanical material properties of advanced composites. The difficulties are most obvious, when it comes to the determination of damping "constants", since these would be expected to be frequency dependent. But even for the measurement of elastic constants there are major problems.

On this reason, Task 1.4 was devoted to the development of inverse technique based on vibration tests and characterisation of advanced composite material properties. It is necessary to note that non-direct optimisation methodology based on the planning of experiments and response surface technique has been applied in this case to decrease considerably the computational efforts.

4.2.1 Identification procedure

The basic idea of the identification technique developed is that simple mathematical models (response surfaces) are determined only by the finite element solutions in the reference points of the experimental design. The functional to be minimised describes the difference between the measured and numerically calculated parameters of the structural response. By minimising the functional, the identification parameters are obtained. A significant reduction in calculations of the identification functional can be achieved in comparison with the conventional methods of minimisation in this case.

The numerical-experimental procedure proposed in the present study consists of five stages presented in Fig. 4.5. In the first stage the physical or numerical experiments are carried out and dynamic parameters of structure are determined. In the second stage the plan of experiments should be developed in dependence on the number of design parameters (identified values) and number of experiments. Then the finite element analysis is performed in the reference points of experimental design and dynamic parameters of structure are calculated in the third stage. In the fourth stage the numerical data obtained by the finite element method are used to determine a simple functions using response surface method. An identification of the material properties is performed in the final stage minimising the error functional between experimental and numerical structural responses.

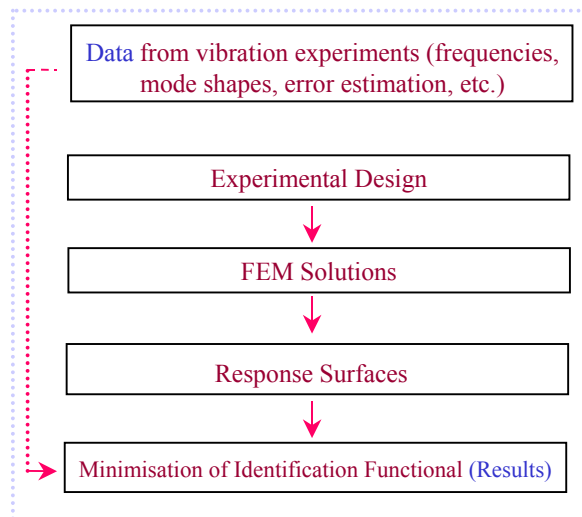


Fig. 4.5 Identification procedure.

4.2.2 Theoretical background

The inverse technique developed requires the following elements: experimental set-up, numerical model and material identification procedure.

4.2.2.1 Experimental set-up

Usually two experimental set-ups are used in the identification procedure. The first is based on the impulse technique and uses contact measurements by accelerometers (Fig. 4.6), the second is based on non-contact laser measurements (Fig. 4.7). In both cases the PCB impulse hammer or shaker or PZT materials glued to the investigated object are applied to produce excitations.

To identify material properties of advanced composites, different rectangular samples are prepared usually. In the present study 3 carbon/epoxy plates (two uni-directionally reinforced and one multi-directionally reinforced) and sandwich plate have been tested. Sandwich plate is made from aluminium external layers and adhesive viscoelastic layer used as a sandwich core. To verify the developed inverse technique, the aluminium plate has been tested also. To avoid additional mechanisms of energy dissipation in supporting constructions, the simply supported boundary conditions have been realised for homogeneous and laminated composite plates. In this case plates have been suspended using two thin threads.

In the present study the eigenfrequencies and corresponding eigenmodes of homogeneous aluminium plate have been determined using POLYTEC laser vibrometer operating on the Doppler principle and measuring back-scattered laser light from a vibrating structure to determine its vibration velocity and displacement. The dynamic characteristics of laminated composite plates have been extracted using ISI-SYS laser vibrograph (Fig. 4.7) operating on the interferometry and correlation principles and using the forced normal mode excitation method for vibration measurements.

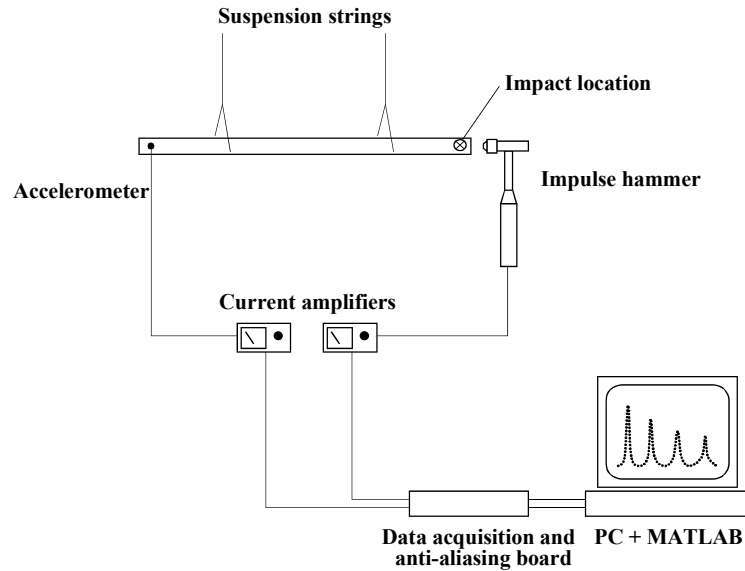


Fig. 4.6 Impulse technique.

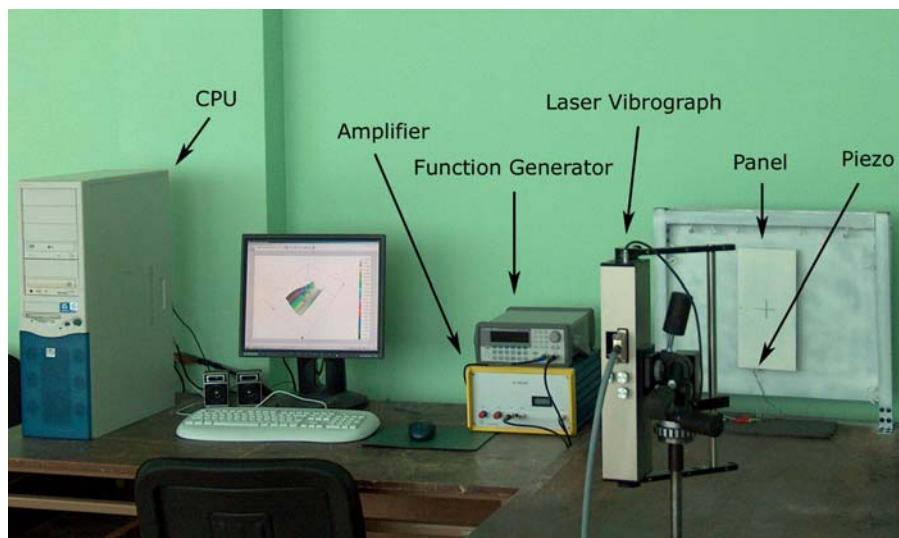


Fig. 4.7 ISI-SYS laser vibrograph.

4.2.2.2 Numerical model

In the present investigation, the finite element method is used for the modelling and dynamic analysis.

Finite element models

Finite element modelling is based on the first-order shear deformation theory including rotation around the normal. In this case the widely known expressions of displacements have the following form:

$$u = u_0 + z\gamma_x \quad , \quad v = v_0 + z\gamma_y \quad , \quad w = w_0 \quad (4.23)$$

where u_0, v_0, w_0 are the displacements in a reference plane, z is the coordinate of the point of interest from a reference plane, γ_x, γ_y are the rotations connected with the transverse shear deformations.

For sandwich composites this hypothesis is applied separately for each layer (Fig. 4.8). This case corresponds to the broken line model [4.47] and satisfies to the following displacement continuity conditions between the layers

$$\begin{aligned} u^{(1)} &= u^{(2)} \Big|_{z=z_1}, & u^{(2)} &= u^{(3)} \Big|_{z=z_2} \\ v^{(1)} &= v^{(2)} \Big|_{z=z_1}, & v^{(2)} &= v^{(3)} \Big|_{z=z_2} \\ w^{(1)} &= w^{(2)} \Big|_{z=z_1}, & w^{(2)} &= w^{(3)} \Big|_{z=z_2} \end{aligned} \quad (4.24)$$

where in the brackets, the numbers of layers are presented.

At the same time for laminated composite models this hypothesis is used already for the entire laminate (Fig. 4.9). In this case transverse shear stiffness is obtained by using the shear correction factors

$$Q_{ij} = k_i k_j \sum_{l=1}^n A_{ij}^l (z_l - z_{l-1}) \quad (4.25)$$

where A_{ij}^l is the stiffness matrix of l^{th} layer, and z_l, z_{l-1} are the upper and lower bounds of l^{th} layer. The shear correction coefficients can be calculated by different approaches [4.48].

Dynamic analysis

To describe the rheological behaviour of viscoelastic materials in the finite element models, the complex modulus representation [4.49] is used. It is necessary to note that the storage and loss moduli in this case are frequency- and temperature-dependent values.

The dynamic characteristics are extracted by the method of complex eigenvalues developed in the frames of CASSEM project (WP2, Task 2.2) and described in the deliverable D4 and in the paper [4.50]. Damped eigenfrequencies and corresponding loss factors in this case are determined from the free vibration analysis of a structure

$$[\mathbf{K}^*(\omega) - \omega^{*2} \mathbf{M}] \bar{\mathbf{X}}^* = 0 \quad (4.26)$$

where \mathbf{M} is the mass matrix of a structure, $\mathbf{K}^*(\omega) = \mathbf{K}(\omega) + i\mathbf{K}''(\omega)$ is the complex stiffness matrix of a structure, $\omega^* = \omega + i\omega''$ is the complex eigenfrequency. The real part ω represents the damped eigenfrequency of a

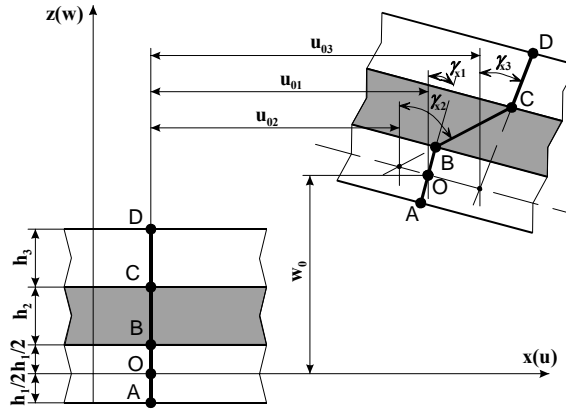


Fig. 4.8 Kinematic assumptions for a sandwich plate in ZX-plane.

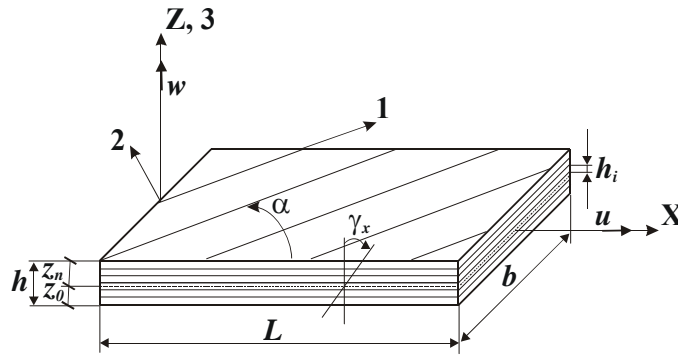


Fig. 4.9 Laminated composite beam.

structure and the imaginary part ω'' specifies the rate of decay of the dynamic process. The matrix $\mathbf{K}(\omega)$ is determined using the storage moduli $E(\omega)$ and $G(\omega)$, while $\mathbf{K}''(\omega)$ is found using the imaginary parts of the complex moduli $E''(\omega) = \eta_E(\omega)E(\omega)$ and $G''(\omega) = \eta_G(\omega)G(\omega)$, where $\eta_E(\omega)$ and $\eta_G(\omega)$ are the material loss factors.

Eq. (4.26) can be written as the non-linear generalised eigenvalue problem

$$\mathbf{K}^*(\omega)\bar{\mathbf{X}}^* = \lambda^*\mathbf{M}\bar{\mathbf{X}}^* \quad (4.27)$$

where $\lambda^* = \omega^{*2}$ is the complex eigenvalue and $\bar{\mathbf{X}}^*$ is the complex eigenvector. Solution of Eq. (4.27) starts with a constant frequency ($\omega = \text{const}$). Then at each step the linear generalised eigenvalue problem with $\mathbf{K}^*(\omega) = \text{const}$ is solved by the Lanczos method, which is programmed in a truncated version, where the generalised eigenvalue problem is transformed into a standard eigenvalue problem with a reduced order symmetric tridiagonal matrix. Orthogonal projection operations are employed with greater economy and elegance using elementary

reflection matrices. The iteration process terminates, when the following condition is satisfied

$$\frac{|\omega_{i+1} - \omega_i|}{\omega_i} * 100\% \leq \xi \quad (4.28)$$

where ξ is a desired precision and ω_{i+1} is the real part of eigenfrequency of a structure calculated from the linear generalised eigenvalue problem with the storage and loss moduli for the frequency ω_i , which was obtained from the same equation in the previous step. The modal loss factors of structure for each vibration mode are determined by the following relation

$$\eta_n = \frac{\lambda_n''}{\lambda_n} \quad (4.29)$$

This approach gives the possibility to preserve the frequency dependence of viscoelastic materials and to calculate structures with high damping. In the case, when the storage and loss moduli are constant values, we have to deal with so called the hysteretic damping model. If only the elastic behaviour is examined, the complex stiffness matrix is changed with the real stiffness matrix.

4.2.2.3 Material identification procedure

At the beginning the plan of experiments should be developed in dependence on the number of design parameters (identified values) and number of experiments.

Planning of experiments

Let us consider a criterion for elaboration of the plans of experiments independent on a mathematical model of the designing object or process. The initial information for elaboration of the plan is number of factors n and number of experiments k . The points of experiments in the domain of factors are distributed as regular as possible (Fig. 4.10). For this reason the following criterion is used

$$\Phi = \sum_{i=1}^k \sum_{j=i+1}^k \frac{1}{l_{ij}^2} \Rightarrow \min \quad (4.30)$$

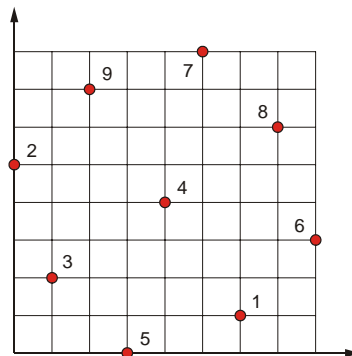


Fig. 4.10 2D design space.

where l_{ij} is the distance between the points having numbers i and j ($i \neq j$). Physically it is equal to the minimum of potential energy of repulsive forces for the points with unity mass if the magnitude of these repulsive forces is inversely proportional to the distance between the points.

For each number of factors n and number of experiments k it is possible to elaborate a plan of experiments. But it needs much computer time, therefore each plan of experiment is elaborated only once and it can be used for various designing cases. The plan of experiments is characterised by the matrix of plan B_{ij} . When the domain of factors is determined as $x_j \in [x_j^{\min}, x_j^{\max}]$, the points of experiments are calculated by the following expression

$$x_j^{(i)} = x_j^{\min} + \frac{1}{k-1} (x_j^{\max} - x_j^{\min}) (B_{ij} - 1), \quad i = 1, 2, \dots, k, \quad j = 1, 2, \dots, n \quad (4.31)$$

Then the numerical computations are carried out in these points and the dynamic characteristics obtained by the finite element method are used to determine a simple functions using response surface method.

Response surfaces

In the present approach a form of the equation of regression is unknown previously. There are two requirements for the equation of regression: accuracy and reliability. Accuracy is characterised as a minimum of standard deviation of the table data from the values given by the equation of regression. Increasing a number of terms in the equation of regression it is possible to obtain a complete agreement between the table data and values given by the equation of regression. However, it is necessary to note that prediction at the intervals between the table points can be not so good. For an improvement of prediction, it is necessary to decrease a distance between the points of experiments by increasing the number of experiments or by decreasing the domain of factors. Reliability of the equation of regression can be characterised by an affirmation that standard deviations for the table points and for any other points are approximately the same. Obviously the reliability is greater for a smaller number of terms of the equation of regression.

The equation of regression can be written in the following form

$$y = \sum_{i=1}^p A_i f_i(x_j) \quad (4.32)$$

where A_i are the coefficients of the equation of regression, $f_i(x_j)$ are the functions from the bank of simple functions $\theta_1, \theta_2, \dots, \theta_m$ which are assumed as,

$$\theta_m(x_j) = \prod_{i=1}^s x_j^{\xi_{mi}} \quad (4.33)$$

where ξ_{mi} is a positive or negative integer including zero. Synthesis of the equation from the bank of simple functions is carried out in two stages: selection of perspective functions from the bank and then step-by-step elimination of the selected functions.

On the first stage, all variants are tested with the least square method and the function, which leads to the minimum of the sum of deviations, is chosen for each variant. On the second stage, the elimination is carried out using the standard deviation

$$\sigma_0 = \sqrt{\frac{S}{k-p+1}}, \quad \sigma = \sqrt{\frac{1}{k-1} \sum_{i=1}^k \left(y_i - \frac{1}{k} \sum_{j=1}^k y_j \right)^2} \quad (4.34)$$

or correlation coefficient

$$c = \left(1 - \frac{\sigma}{\sigma_0} \right) * 100\% \quad (4.35)$$

where k is the number of experimental points, p is the number of selected perspective functions and S is the minimum sum of deviations. It is more convenient to characterise an accuracy of the equation of regression by the correlation coefficient (Fig. 4.11). If insignificant functions are eliminated from the equation of regression, a reduction of the correlation coefficient is negligible. If in the equation of regression only significant functions are presented, elimination of one of them leads to important decrease of the correlation coefficient.

Then an identification of viscoelastic material properties $E^*(\omega)$ and $G^*(\omega)$ is carried out minimising the error functional between experimental and numerical structural responses for each eigenmode

$$\Phi_i(\mathbf{X}) = \frac{(f_i^{\text{exp}} - f_i^{\text{FEM}})^2}{(f_i^{\text{exp}})^2} + \frac{(\eta_i^{\text{exp}} - \eta_i^{\text{FEM}})^2}{(\eta_i^{\text{exp}})^2} \Rightarrow \min \quad (4.36)$$

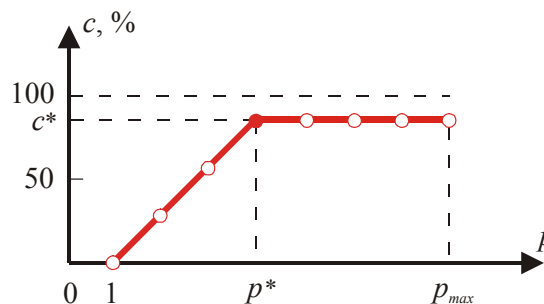


Fig. 4.11 Diagram of elimination for the correlation coefficient.

In this case we have an identified material properties for each eigenfrequency. After application of the curve fitting procedure the frequency-dependent viscoelastic material properties are easily obtained.

Non-linear optimisation

To minimise the error functional, the following constrained non-linear optimisation problem should be examined

$$\begin{aligned} \min \Phi(x); H_i(x) \geq 0; G_j(x) = 0 \\ i = 1, 2, \dots, I; j = 1, 2, \dots, J \end{aligned} \quad (4.37)$$

where I and J are the numbers of inequality and equality constraints. This problem is replaced to the unconstrained minimisation problem in which the constraints are taken into account with the penalty functions. New version of random search method is used for solving of the formulated optimisation problem.

4.2.3 Identification of material properties

Testing of the developed inverse technique based on vibration tests has been carried out identifying the material properties of homogeneous isotropic aluminium plate. Then the orthotropic material properties of 3 carbon/epoxy plates (two uni-directionally reinforced and one multi-directionally reinforced) and viscoelastic material properties of sandwich plate adhesive core have been identified.

4.2.3.1 Identification of isotropic material properties

Identification of isotropic material properties has been carried out for the aluminium plate (Fig. 4.12) with the density and geometrical parameters presented in Table 4.9. The eigenfrequencies have been measured by two experimental techniques: Pulse LabShop technique and POLYTEC laser vibrometer.

To describe the isotropic material properties only two material constants are necessary: E – modulus of elasticity and G – shear modulus. Shear modulus is taken instead of Poisson ratio ν to get approximately the close values for material constant borders (Table 4.10) used in the identification process. In this case an application of any scaling technique is not required.

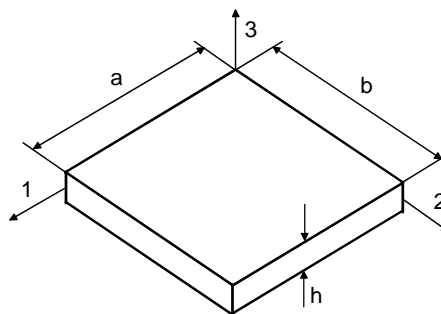


Fig. 4.12 Homogeneous plate.

Table 4.9 Geometric dimensions and density of aluminium plate.

Specimen	AL-SP1
a , mm	300
b , mm	300
h , mm	2.3
ρ , kg/m ³	2800

Table 4.10 Borders of identified parameters.

Parameters of identification	min	max
E , GPa	60	80
G , GPa	22	30

The plan of experiments has been produced for 2 design parameters and 35 experiments. Then finite element analysis has been performed in 35 experimental points and 17 first eigenfrequencies has been determined. Employing these numerical values, the approximating functions (response surfaces) for all eigenfrequencies, excluding coupled eigenfrequencies, were obtained. The error functional in this case can be written in the following form:

$$\Phi(\mathbf{X}) = \sum_{i=1}^9 \frac{(f_i^{\text{exp}} - f_i^{\text{FEM}})^2}{(f_i^{\text{exp}})^2} \Rightarrow \min \quad (4.38)$$

Minimising this functional, the elastic material constants have been obtained (Table 4.11). The results have been verified comparing the experimentally measured eigenfrequencies with the numerically obtained using the identified elastic properties. The residuals are calculated by the following expression

$$\Delta_i = \frac{|f_i^{\text{exp}} - f_i^{\text{FEM}}|}{f_i^{\text{exp}}} \times 100\% \quad (4.39)$$

Results of verification for the aluminium plate are given in Table 4.12. It is seen from this table that the eigenfrequencies calculated by the finite element method using the elastic properties obtained through identification procedure are in good agreement with the experimental results. The difference in terms of residuals is less than 1% in most cases. It is necessary to note that only eigenfrequencies located in the table cells coloured by grey pen have been taken into identification process.

Table 4.11 Material constants identified.

	E , GPa	G , GPa	ν
POLYTEC	70.45	26.29	0.34
Pulse LabShop	70.85	26.64	0.33

Table 4.12 Verification of eigenfrequencies (Hz)
using the identified parameters obtained.

Mode	POLYTEC			PULSE LabShop		
	EXP	FEM	Δ , %	EXP	FEM	Δ , %
1	83	82	1.20	83	83	0
2	118	120	1.69	120	120	0
3	154	153	0.65	154	153	0.65
4	212	214	0.94	214	215	0.47
5	215	214	0.47	216	215	0.46
6	379	382	0.79	381	382	0.26
7	384	382	0.52	383	382	0.26
8	390	392	0.51	394	394	0
9	428	426	0.47	428	428	0
10	486	482	0.82	485	482	0.62
11	636	652	2.52	649	654	0.77
12	655	652	0.46	657	654	0.46
13	734	729	0.68	721	730	1.25
14	761	768	0.92	764	767	0.39
15	818	819	0.12	808	820	1.49
16	825	819	0.73	821	820	0.12
17	948	946	0.21	953	949	0.42

4.2.3.2 Identification of orthotropic material properties

Identification of orthotropic material properties has been carried out for the 3 laminated carbon/epoxy plates (two uni-directionally reinforced made from the same material and one multi-directionally reinforced) (Fig. 4.13) with the density, layer stacking sequence and geometrical parameters presented in Table 4.13. Fibre volume content of these laminates is about 60%. The eigenfrequencies have been measured by ISI-SYS laser vibrograph.

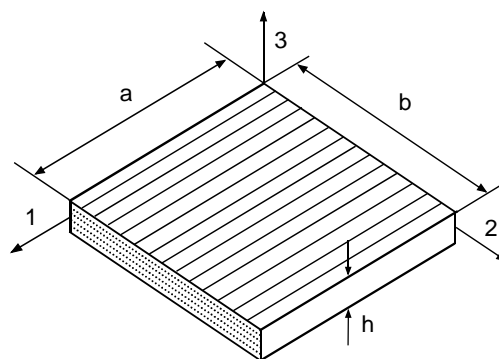


Fig. 4.13 Laminated composite plate.

Table 4.13 Geometric dimensions and density of laminated composite plates.

Specimen	LA-UD-SP1	LA-UD-SP2	LA-MD-SP1
$a=b$, mm	207.5	205	210
h , mm	2.0	2.0	2.0
ρ , kg/m ³	1535	1589	1619
lay-up	(0) ₁₆	(0) ₁₆	(0/90/45/-45) _{S2}

To describe the orthotropic material properties of a single layer in the laminated composite plate, five material constants are necessary: $E_1, E_2 = E_3$ – moduli of elasticity, $G_{12} = G_{13}, G_{23}$ – shear moduli and $\nu_{12} = \nu_{13}$ - Poisson ratio. Since the parameters with so different magnitude, like elastic moduli and Poisson ration, are taken for identification, some scaling operators should be carried out. In the paper [4.51] the scaling by longitudinal modulus E_1 was employed and in addition a fixed scaling factor was chosen. Similar scaling and reparametrisation was employed in [4.52], where additional scaling by the first experimental frequency allows reducing the number of unknown variables from five to four. Thus material parameters of a single layer can be expressed in terms of dimensionless variables [4.12]

$$\begin{aligned}
\alpha_2 &= 4 - 4(E_2 / E_1) \\
\alpha_3 &= 1 + (E_2 / E_1)(1 - 2\nu_{12}) - 4(G_{12} / E_1)\alpha_0 \\
\alpha_4 &= 1 + (E_2 / E_1)(1 + 6\nu_{12}) - 4(G_{12} / E_1)\alpha_0 \\
\alpha_5 &= 4(G_{23} + G_{12})\alpha_0 / E_1
\end{aligned} \tag{4.40}$$

where $\alpha_0 = 1 - \nu_{12}^2(E_2 / E_1)$. Now the vector of parameters to be identified is defined through dimensionless quantities $\mathbf{X} = [x_1, x_2, x_3, x_4] = [\alpha_2, \alpha_3, \alpha_4, \alpha_5]$.

Let the experimental eigenfrequencies are $\omega_1^{\text{exp}}, \omega_2^{\text{exp}}, \dots, \omega_N^{\text{exp}}$, where N is the number of measured eigenfrequencies. The value of N is taken usually between 7 and 15. The corresponding numerical eigenfrequencies for the set of material parameters α_i are $\omega_1^{\text{FEM}}, \omega_2^{\text{FEM}}, \dots, \omega_N^{\text{FEM}}$. Let us consider the scaling parameter C , which is chosen according the relation

$$C = \frac{\omega_1^{\text{exp}2}}{(E_1^0)\omega_1^{\text{FEM}2}} \tag{4.41}$$

where ω_1^{FEM} is the first numerical eigenfrequency calculated with the prior selected value of the longitudinal Young's modulus E_1^0 of the layer.

The plan of experiments has been produced for 4 design parameters and 35 experiments. The borders for the identified parameters are given in Table (4.14). Then finite element analysis has been performed in 35 experimental points and 17

Table 4.14 Borders of identified parameters.

Parameters of identification	LA-UD-SP1		LA-UD-SP2		LA-MD-SP1	
	min	max	min	max	min	max
E_1^0 , GPa	171		170		150	
$E_2 = E_3$, GPa	9.6	11.6	10.6	11.6	7.5	9.5
$G_{12} = G_{13}$, GPa	5.25	7.25	5.8	6.8	5.0	6.5
G_{23} , GPa	6.5	8.5	4.0	5.2	5.0	10.0
$\nu_{12} = \nu_{13}$	0.2	0.45	0.2	0.45	0.25	0.45

first eigenfrequencies has been determined for the uni-directional laminated plates and 40 first eigenfrequencies – for multi-directional laminated plate. Employing these numerical values, the approximating functions (response surfaces) for all eigenfrequencies were obtained. The error functional in this case can be written in the following form:

$$\Phi(\mathbf{X}) = \sum_{i=2}^N \frac{(\omega_i^{\text{exp}2} - C\omega_i^{\text{FEM}2})^2}{\omega_i^{\text{exp}4}} \Rightarrow \min \quad (4.42)$$

and solution should satisfied to the following constraints:

$$\begin{aligned}
g_1(\mathbf{x}) &= \alpha_2 > 0 \quad \text{or} \quad E_2/E_1 > 1 \\
g_2(\mathbf{x}) &= \frac{8 - \alpha_2 - 3\alpha_3 - \alpha_4}{16 \left\{ 1 - \left[\frac{\alpha_4 - \alpha_3}{8 - 2\alpha_2} \right]^2 \left(\frac{4 - \alpha_2}{4} \right) \right\}} > 0 \quad \text{or} \quad G_{12}/E_1 > 0 \\
g_3(\mathbf{x}) &= \frac{2\alpha_5 - 1/2(8 - \alpha_2 - 3\alpha_3 - \alpha_4)}{8 \left\{ 1 - \left[\frac{\alpha_4 - \alpha_3}{8 - 2\alpha_2} \right]^2 \left(\frac{4 - \alpha_2}{4} \right) \right\}} > 0 \quad \text{or} \quad G_{23}/E_1 > 0 \quad (4.43) \\
g_4(\mathbf{x}) &= -\frac{(\alpha_4 - \alpha_3)}{(8 - 2\alpha_2)} + \sqrt{\frac{4}{4 - \alpha_2}} > 0 \quad \text{or} \quad \sqrt{E_1/E_2} - |\nu_{12}| > 0 \\
\alpha_i^{\min} &\leq \alpha_i \leq \alpha_i^{\max}, \quad i = 2, 3, 4, 5
\end{aligned}$$

These constraints denote conditions of a positive definiteness of elasticity matrix.

It should be noted that the number of frequencies used for the identification is different for each specimen. The experimentally measured frequencies can be used for identification in any combination. A cross validation for all sample points was performed in such way to achieve a better approximation of the original function and to select the most important (most sensitive to elastic constants) and reliable frequencies. The results of identification after application of the following inverse relations

$$\begin{aligned}
\frac{E_2}{E_1} &= \frac{4 - \alpha_2}{4} \\
\frac{G_{12}}{E_1} &= \frac{8 - \alpha_2 - 3\alpha_3 - \alpha_4}{16\alpha_0} \\
\nu_{12} &= \frac{\alpha_4 - \alpha_3}{8 - 2\alpha_2} \\
\frac{G_{23}}{E_1} &= \frac{2\alpha_5 - 0.5(8 - \alpha_2 - 3\alpha_3 - \alpha_4)}{8\alpha_0}
\end{aligned} \tag{4.44}$$

are given in Table 4.15. After evaluation of these parameters the value of Young's modulus of the layer in the fibre direction E_1 can be easily obtained, since C and α_0 are known. The steps of this evaluation are shown below.

The eigenvalue problem for mode $\bar{\mathbf{X}}_1$ corresponding to the first experimental eigenfrequency ω_1^{exp} can be written in an equivalent form placing E_1 in evidence:

$$E_1 \hat{\mathbf{K}} \bar{\mathbf{X}}_1 = \omega_1^{\text{exp}2} \mathbf{M} \bar{\mathbf{X}}_1 \tag{4.45}$$

were $E_1 \hat{\mathbf{K}} = \mathbf{K}$ is the stiffness matrix. Taking into account the relation (4.41) this equation can be written as

$$CE_1^0 \hat{\mathbf{K}} \bar{\mathbf{X}}_1 = C \omega_1^{\text{FEM}2} \mathbf{M} \bar{\mathbf{X}}_1 \tag{4.46}$$

were $E_1 = CE_1^0$ and E_1^0 is the initial guess value given to the Young's modulus in the fibre direction of the layer and E_1 is the corresponding identified mechanical property.

The results have been verified comparing the experimentally measured eigenfrequencies with the numerically obtained using the identified elastic properties. The residuals are calculated by Eq. (4.39). Results of verification for laminated composite plates are given in Table 4.16. It is seen from this table that the eigenfrequencies calculated by the finite element method using the elastic

Table 4.15 Material constants identified.

Identified parameters	LA-UD-SP1	LA-UD-SP2	LA-MD-SP1
E_1 , GPa	171.05	171.37	153.17
$E_2 = E_3$, GPa	10.44	11.20	8.16
$G_{12} = G_{13}$, GPa	6.07	6.35	5.79
G_{23} , GPa	7.71	4.57	7.84
$\nu_{12} = \nu_{13}$	0.48	0.23	0.27

Table 4.16 Verification of eigenfrequencies (Hz)
using the identified parameters obtained.

Mode	LA-UD-SP1			LA-UD-SP2			LA-MD-SP1		
	EXP	FEM	Δ , %	EXP	FEM	Δ , %	EXP	FEM	Δ , %
1	97	97	0	98	98	0	164	164	0
2	124	124	0	127	127	0	257	269	4.67
3	237	234	1.27	238	237	0.42	326	322	1.23
4	341	342	0.29	350	350	0	421	433	2.85
5	458	454	0.87	458	460	0.44	453	450	0.66
6	503	503	0.00	496	496	0	-	786	-
7	541	539	0.37	533	533	0	797	792	0.63
8	653	650	0.46	649	648	0.15	848	847	0.12
9	-	-	-	-	-	-	904	899	0.55
10	-	-	-	-	-	-	1021	1003	1.76
11	-	-	-	858	857	0.12	1325	1309	1.21
12	-	-	-	-	-	-	-	1343	-
13	1168	1167	0.09	-	-	-	1530	1529	0.07
14	-	-	-	-	-	-	-	1661	-
15	1381	1377	0.29	1355	1359	0.30	1692	1668	1.42
16	1413	1408	0.35	1391	1390	0.07	1810	1777	1.82
17	1512	1503	0.60	1487	1487	0	1878	1906	1.49
18	-	-	-	-	-	-	-	2040	-
19	-	-	-	-	-	-	2175	2162	0.60
20	-	-	-	-	-	-	2534	2529	0.20
21	-	-	-	-	-	-	-	2636	-
22	-	-	-	-	-	-	2652	2658	0.23
23	-	-	-	-	-	-	2726	2718	0.29
24	-	-	-	-	-	-	2758	2744	0.51
25	-	-	-	-	-	-	2892	2851	1.42
26	-	-	-	-	-	-	-	3041	-
27	-	-	-	-	-	-	-	3198	-
28	-	-	-	-	-	-	3482	3506	0.69
29	-	-	-	-	-	-	-	3647	-
30	-	-	-	-	-	-	-	3763	-
31	-	-	-	-	-	-	3782	3799	0.45
32	-	-	-	-	-	-	-	3881	-
33	-	-	-	-	-	-	-	4054	-
34	-	-	-	-	-	-	-	4154	-
35	-	-	-	-	-	-	4320	4259	1.41
36	-	-	-	-	-	-	-	4512	-
37	-	-	-	-	-	-	-	4523	-
38	-	-	-	-	-	-	-	4577	-
39	-	-	-	-	-	-	4911	4884	0.55
40	-	-	-	-	-	-	-	5082	-

Table 4.17 Comparison of identified material properties with the results of static tests.

Material properties	LA-UD-SP1 and LA-UD-SP2		LA-MD-SP1	
	Static test	Identified	Static test	Identified
E_1 , GPa	176 (143)	171	168 (145)	153
$E_2 = E_3$, GPa	8.9 (9.6)	10.8	9.1 (8.9)	8.2
$G_{12} = G_{13}$, GPa	5.2	6.5	5.6	5.8
G_{23} , GPa	-	6.1	-	7.8
$\nu_{12} = \nu_{13}$	0.34	0.36	0.33	0.27

properties obtained through identification procedure are in good agreement with the experimental results even for the frequencies not used in identification process. The difference in terms of residuals is less than 2% in most cases. It is necessary to note that only eigenfrequencies located in the table cells coloured by grey pen have been taken into identification process.

In order to validate results obtained from identification, static tests have been carried out according to ASTM guidelines. Test results are presented in Table 4.17, where in the brackets the values obtained from static compression tests are given. In general satisfied agreement of the results is observed.

4.2.3.3 Identification of viscoelastic material properties

Identification of viscoelastic material properties has been carried out for the 3M viscoelastic damping polymer ISD-112 used as a core material in the sandwich panel (Fig. 4.14). The external layers made from aluminium 2024 T6 have the following properties: $E=64$ GPa, $\nu=0.32$, $\rho=2695 \cdot \text{Ns}^2/\text{m}^4$. This panel can be examined as a sandwich beam with width $b=0.05$ m, length $L=0.3$ m and thickness of layers $h_1=0.0012$ m, $h_2=0.0001016$ m, $h_3=0.0008$ m. The clamped boundary conditions are applied from one side of the beam (Fig. 4.15). Its dynamic characteristics (eigenfrequencies and corresponding loss factors) have been determined numerically using the complex eigenvalues method.

To describe the viscoelastic isotropic material properties only one material parameter is necessary: $E^*(\omega) = E(\omega) + iE''(\omega)$ - modulus of elasticity. However in this case, it is complex value consisting of storage $E(\omega)$ and loss $E''(\omega)$ parts, which are both frequency-dependent values. As known material parameters, Poisson ratio $\nu=0.49$ and density $\rho=1300 \cdot \text{Ns}^2/\text{m}^4$ are taken into consideration. The borders for the identified parameters are given in Table (4.18) to follow the material properties presented in Table (4.19) for the frequency range $f=0, \dots, 2000$ Hz and temperature 37.8°C .

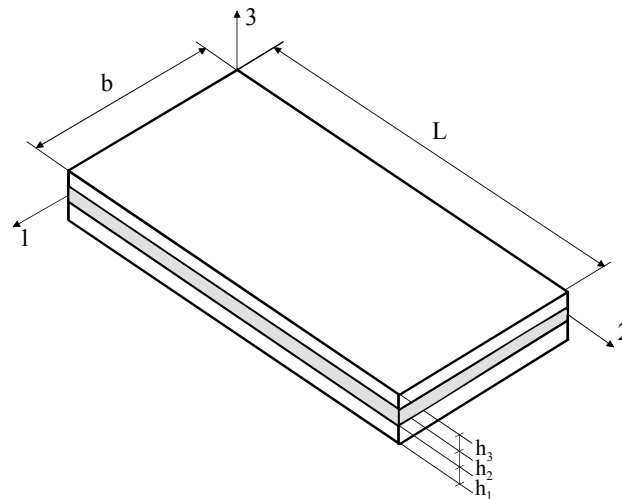


Fig. 4.14 Sandwich panel.

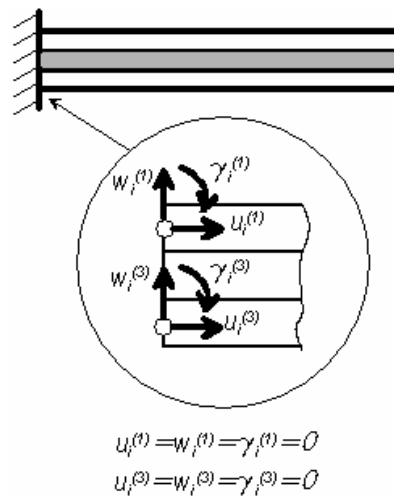


Fig. 4.15 Boundary conditions applied.

Table 4.18 Borders of identified parameters.

Parameters of identification	min	max
$E(\omega)$, MPa	0.596	5.960
$E''(\omega)$, MPa	0	7.228

Table 4.19 Borders of identified material properties.

Parameters of identification	min	max
G , MPa	0.2	2.0
η	0	1.4

The plan of experiments has been produced for 2 design parameters and 48 experiments (Fig. 4.16). Then finite element analysis has been performed in 48 experimental points and 8 first dynamic characteristics have been determined. Employing these numerical values, the approximating functions (response surfaces) for all eigenfrequencies (in Hz) and corresponding loss factors were obtained with the correlation coefficients higher than 90%:

$$c=93.90\%$$

$$f_1=18.6-1.28*z_2+1.13/z_1*z_2+0.0329/z_2^2+0.592*z_1*z_2+0.000742/z_1^3-0.923/z_1$$

where $z_1=0.0+0.168*E$
 $z_2=0.5+0.138*E''$

$$c=91.10\%$$

$$\eta_1=-0.115+0.246/z_1+0.102*z_2-0.13/z_1*z_2+0.000429/z_1^2-.091/z_2/z_1+0.0154/z_2^2$$

where $z_1=0.0+0.168*E$
 $z_2=0.5+0.138*E''$

$$c=95.20\%$$

$$f_2=95.9+7.14*z_1-14.6/z_1+0.234/z_1^2+10.8/z_1*z_2+2.18/z_2/z_1$$

where $z_1=0.0+0.168*E$
 $z_2=0.5+0.138*E''$

$$c=93.60\%$$

$$\eta_2=0.153-0.0558/z_2-0.0661*z_1+0.167/z_1-0.0864/z_2/z_1$$

where $z_1=0.0+0.168*E$
 $z_2=0.5+0.138*E''$

$$c=96.10\%$$

$$f_3=220+33.3*z_1-12.2/z_1+1.14/z_1^2+11.5/z_1*z_2^2-1.25/z_1^2*z_2$$

where $z_1=0.0+0.168*E$
 $z_2=0.5+0.138*E''$

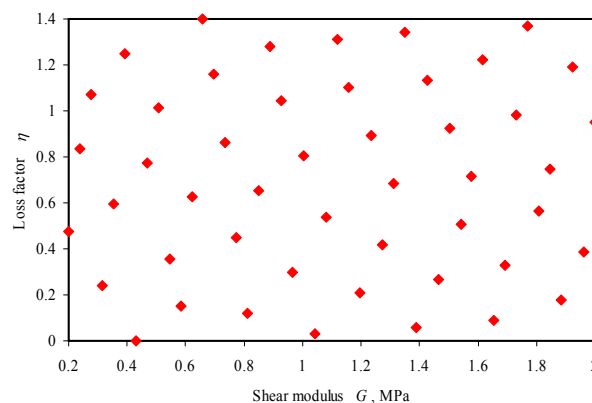


Fig. 4.16 Plan of experiments.

$$c=96.50\%$$

$$\eta_3=0.0452-0.188/z_2-0.325/z_2/z_1+0.66/z_1+0.079/z_2^2$$

$$\text{where } z_1=0.388+0.187*E \\ z_2=0.500+0.138*E''$$

$$c=97.90\%$$

$$f_4=262+107*z_1+110*z_2-8.27/z_1+24.3/z_2+0.443/z_1^2-52.3*z_1*z_2$$

$$\text{where } z_1=0.0+0.168*E \\ z_2=0.5+0.138*E''$$

$$c=96.60\%$$

$$\eta_4=-0.152+0.129*z_1-0.385/z_1-0.348*z_2+1.27/z_1*z_2-0.237/z_1^2*z_2^2$$

$$\text{where } z_1=0.388+0.187*E \\ z_2=0.500+0.138*E''$$

$$c=97.80\%$$

$$f_5=563+81.4*z_1-134/z_1+29/z_2/z_1+89.2/z_1*z_2$$

$$\text{where } z_1=0.388+0.187*E \\ z_2=0.500+0.138*E''$$

$$c=96.50\%$$

$$\eta_5=0.0927-0.0468/z_2-0.192/z_1+0.381/z_1*z_2$$

$$\text{where } z_1=0.388+0.187*E \\ z_2=0.500+0.138*E''$$

$$c=97.60\%$$

$$f_6=889+66.6*z_1+20.8*z_2-11*z_1^2+6.89*z_2^2$$

$$\text{where } z_1=-1.22+0.373*E \\ z_2=-1.00+0.277*E''$$

$$c=95.10\%$$

$$\eta_6=0.2+0.196*z_2-0.0585*z_1-0.0592*z_1*z_2$$

$$\text{where } z_1=-1.22+0.373*E \\ z_2=-1.00+0.277*E''$$

$$c=98.10\%$$

$$f_7=1200+72.6*z_1+18.6*z_2-8.91*z_1^2+7.04*z_2^2$$

$$\text{where } z_1=-1.22+0.373*E \\ z_2=-1.00+0.277*E''$$

$$c=97.50\%$$

$$\eta_7=-0.266+0.587*z_2-0.154*z_1+0.0815/z_2*z_1-0.119*z_2^2$$

$$\text{where } z_1=0.0+0.168*E \\ z_2=0.5+0.138*E''$$

$c=98.40\%$
 $f_8=1560+76.7*z_1+16.2*z_2-7.22*z_1^2+6.66*z_2^2$
 where $z_1=-1.22+0.373*E$
 $z_2=-1.00+0.277*E''$

$c=98.10\%$
 $\eta_8=-0.0952+0.276*z_2-0.0221/z_2+0.0176/z_2*z_1-0.0671*z_1*z_2$
 where $z_1=0.0+0.168*E$
 $z_2=0.5+0.138*E''$

The error functional in this case is determined for each eigenmode using Eq. (4.36). Minimising this functional, the material properties have been obtained for each eigenfrequency (Table 4.20 and Fig. 4.17). Then the curve fitting procedure is applied and the following shear modulus (in MPa) and loss factor as functions on frequency are obtained

$c=86.51\%$
 $G=2.783-1.023/z$
 where $z=0.394+0.0003736*f$

Table 4.20 Material properties identified for each eigenfrequency.

Mode n	G MPa	η
1	0.299	0.247
2	0.364	0.609
3	0.593	0.887
4	0.866	0.904
5	1.080	1.022
6	1.308	1.093
7	1.654	1.114
8	1.839	1.116

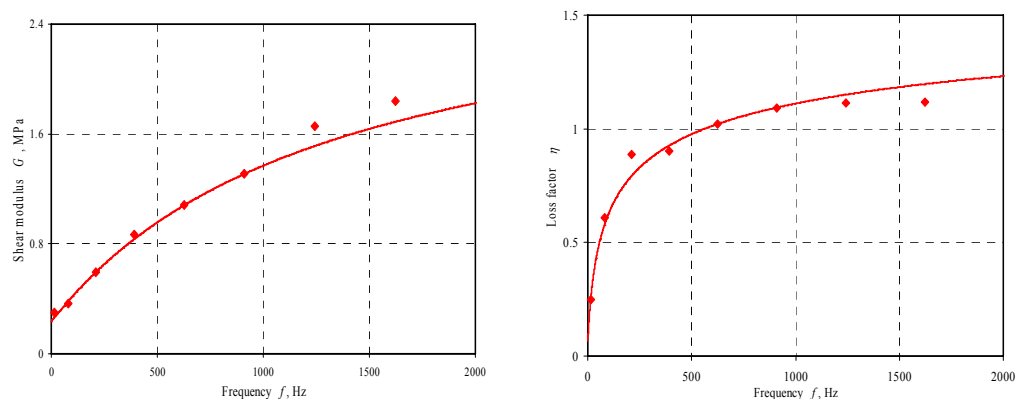


Fig. 4.17 Viscoelastic material properties identified.

$$c=89.88\%$$

$$\eta=1.683+0.001468/z-0.5274/z^{0.25}$$

$$\text{where } z=0.005+0.0006134*f$$

These dependencies are presented graphically in Fig. 4.17 with a line. To verify them, graphs from the literature [4.53] have been used. Fig. 4.18 shows a very good coincidence between identified and experimentally measured parameters.

The identified material properties have been verified comparing the results of numerical experiment and results obtained numerically by the complex eigenvalues method using the identified viscoelastic material properties. The residuals for damped eigenfrequencies have been calculated using Eq. (4.39), but for corresponding loss factors have been determined by the following expression

$$\Delta_i = \frac{|\eta_i^{\text{exp}} - \eta_i^{\text{FEM}}|}{\eta_i^{\text{exp}}} \times 100\% \quad (4.47)$$

Results of verification for the sandwich panel with the 3M viscoelastic damping polymer ISD-112 used as a core material are given in Tables 4.21 and 4.22. It is seen from these tables that the damped eigenfrequencies and corresponding loss factors calculated by the finite element method using the viscoelastic properties obtained through identification procedure are in very good agreement with the results of numerical experiment. The difference in terms of residuals for eigenfrequencies is less than 1% in most cases and for loss factors is less than 5% in most cases.

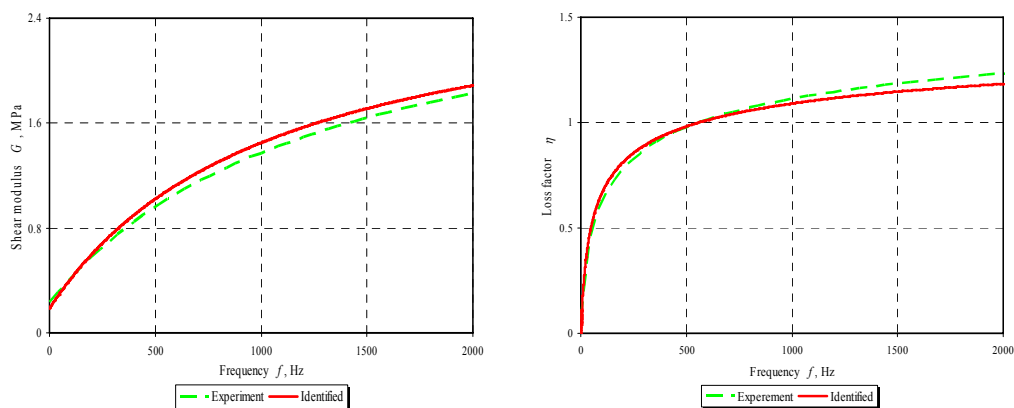


Fig. 4.18 Verification of viscoelastic material properties identified.

Table 4.21 Verification of eigenfrequencies (Hz) using the identified viscoelastic material properties.

Mode	EXP	FEM	Δ , %
1	16	16	0
2	80	80	0
3	210	212	0.95
4	391	395	1.02
5	625	631	0.96
6	908	915	0.77
7	1241	1247	0.48
8	1622	1628	0.37

Table 4.22 Verification of loss factors using the identified viscoelastic material properties.

Mode	EXP	FEM	Δ , %
1	0.055	0.058	5.45
2	0.156	0.164	5.13
3	0.206	0.214	3.88
4	0.223	0.227	3.59
5	0.223	0.230	3.14
6	0.216	0.220	1.85
7	0.205	0.206	0.49
8	0.191	0.190	0.52

4.2.4 Conclusions

The inverse technique using vibration tests has been developed to characterise advanced composite material properties. The non-direct optimisation methodology based on the planning of experiments and response surface technique to minimise the error functional has been applied in this case to decrease considerably the computational efforts. The technique developed has been successfully tested to characterise isotropic elastic material properties of homogeneous aluminium plates and successfully applied to characterise orthotropic elastic material properties of laminated plates and viscoelastic material properties of damping polymer ISD-112 used as a core material in the sandwich panels.

5 General conclusions

The following identification technique has been developed, tested and applied to characterise advanced composite material properties:

- The identification technique to characterise elastic and plastic material properties from indentation tests,
- The technique based on the computation of effective properties on a so-called representative volume element to characterise the mechanical as well as electrical properties of composite actuators/sensors with embedded fibres made of piezoelectric material,
- The inverse identification technique based on vibration tests to characterise elastic, hysteretic, viscoelastic and piezoelectric material properties.

The inverse technique developed potentially offers a lot of benefits as compared with many standard test procedures like tensile, bending, torsion and shear tests:

- The inverse technique uses a test specimen produced with the same technique as for the production of the construction in which the material is used. The geometry of the test specimen can be adapted to the production technique (plates, shells, arbitrary shapes, even real parts). In this way the test specimen used in an inverse technique has the same material properties as in the construction.
- The inverse technique requires simple and cheap test equipment than standard testing procedures, but remains fast and accurate. An inverse technique can thus be considered as a good alternative for standard testing, even in the case of simple material behaviour.
- The use of non-contact sensors allows an obtaining of the material data under more realistic operation conditions.
- The inverse technique based on experiment design is fast and provides simultaneously all the different material properties in the constitutive behaviour of the test specimens.
- The inverse technique is a non-destructive technique that enables many repeated tests on the same specimen.
- For some types of materials, like advanced composites, it is important to avoid introducing damage in the test specimen. The inverse technique provides more flexibility and less restriction in a choice of the test specimen geometry.
- The inverse technique procedure can be automated using PC based software and can be implemented with a user-friendly graphical interface that is very convenient for industrial applications.

After investigations carried out it can be concluded that only the in-plane mechanical properties are always evaluated without major discrepancies in laminated single-material plates. However, already for the laminated plates made from a few materials, considerable difficulties appear. The same can be said about laminated plates made from viscoelastic materials, when the storage and loss moduli are strongly dependent on frequency.

Identification of out-of-plane material properties playing considerable role in the analysis of thick laminated plates also requires additional investigations, since the plates tested in most studies are not thick enough for these moduli to be correctly identified.

Additional investigations require characterisation of viscoelastic adhesive material properties, damping polymers and foams, thermoplastic and woven composites, when material properties are strongly dependent from the technological process applied. In this case even structural components, instead of material samples, can be used in the inverse problem to characterize their material properties from vibration tests.

It is necessary to note also that dynamic characteristics determination especially for highly damped structures in the medium and high frequency ranges by an experimental technique does not give satisfied results and on this reason requires additional investigations.

References

- 2.1 R. Mahnken and E. Stein. A unified approach for parameter identification of inelastic material models in the frame of the finite element method. *Comput. Methods Appl. Mech. Engrg.*, 1996, 136, 225-258.
- 2.2 R. Mahnken and E. Stein The identification of parameters for visco-plastic models via finite-element methods and gradient methods. *Modelling Simul. Mater. Sci. Eng.*, 1994, 2, 597-616.
- 2.3 R. Mahnken and E. Stein. Parameter identification for viscoplastic models based on analytical derivatives of a least-squares functional and stability investigations. *Int. J. Plasticity*, 1996, 12, 451-479.
- 2.4 Visual Numerics, IMSL Math/Library, Vol. 1 and 2, 1997.
- 2.5 N. Huber and Ch. Tsakmakis. A Neural Network Tool for Identifying the Material Parameters of a Finite Deformation Viscoplasticity Model with Static Recovery, 2001.
- 2.6 MATLAB, The Language of Technical Computing, 2002.
- 2.7 R. Rikards, A. Chate and G. Gailis. Identification of elastic properties of laminates based on experiment design. *Int. J. Solids Structures*, 2001, 38, 5097-5115.
- 2.8 G. Rauchs. Parameter Identification from Uniaxial Testing Using Numerical Optimization, CRP Henri Tudor, 2003.
- 2.9 G. Rauchs. Material Parameter Identification Using an Optimization Method in Finite Element Modelling with Co-rotational Finite Strain Formulation, CRP Henri Tudor, 2003.
- 2.10 G. Rauchs. Parameter Identification from Uniaxial Testing Using Numerical Optimization, 2003.
- 2.11 G. Rauchs. Finite Element Implementation of Non-Linear Finite Strain, 2003.
- 2.12 G. Rauchs. Implementation of a Plasticity Model with Non-linear Kinematic and Isotropic Hardening into the in-House Finite Element Code, 2003.
- 2.13 F. Auricchio and R. L. Taylor. Two material models for cyclic plasticity: nonlinear kinematic hardening and generalized plasticity. *Int. J. Plasticity*, 1995, 11, 65-98.
- 2.14 R. Mahnken and E. Stein. Parameter identification for finite deformation elasto-plasticity in principal directions. *Comput. Methods Appl. Mech. Engrg.*, 1997, 147, 17-39.
- 2.15 J. Fish and K. Shek. Finite deformation plasticity based on the additive split of the rate of deformation and hyperelasticity. *Comput. Methods Appl. Mech. Engrg.*, 2000, 190, 75-93.
- 2.16 J. Fish and K. Shek. Computational aspects of incrementally objective algorithms for large deformation plasticity. *Int. J. Numer. Meth. Engng.*, 1999, 44, 839-851.
- 2.17 R. Mahnken and E. Stein. Parameter identification for viscoplastic models based on analytical derivatives of a least-squares functional and stability investigations. *Int. J. Plasticity*, 1996, 12, 451-479.
- 2.18 T. A. Laursen. Computational Contact and Impact Mechanics. Springer Verlag, 2002.
- 2.19 J. Fish and K. Shek. Computational aspects of incrementally objective algorithms for large deformation plasticity. *Int. J. Numer. Meth. Engng.*,

1999, 44, 839-851.

- 3.1 P. Tan and L. Tong. Micro-electromechanics models for piezoelectric-fiber-reinforced composite materials. *Composites Science and Technology*, 2001, 61, 759-769.
- 3.2 B. Agarwal and L. Broutman. Analysis and Performance of Fiber Composites. Second Edition, John Wiley & Sons, 1990.
- 3.3 R. A. Schapery. Thermal expansion coefficients of composite materials based on energy principles. *J. Compos. Mater.*, 1968, 2, 280-404.
- 3.4 Macro Fiber Composites, Smart Material Corp. <http://smart-material.com>

- 4.1 A. L. Araujo, C. M. M. Soares, J. Herskovits and P. Pedersen. Development of a finite element model for the identification of mechanical and piezoelectric properties through gradient optimisation and experimental vibration data. *Composite Structures*, 2002, 58, 307-318.
- 4.2 P. Pedersen. Identification techniques in composite laminates. – In: *Mechanics of Composite Materials and Structures* (Eds. C. A. M. Soares, C. M. M. Soares and M. J. M. Freitas), Kluwer Academic Publishers: Dordrecht, 1999, 443-452.
- 4.3 R. Rikards, H. Abramovich, T. Green, J. Auzins and A. Chate. Identification of elastic properties of composite laminates. *Mechanics of Advanced Materials and Structures*, 2003, 10, 335-352.
- 4.4 J. Cunha and J. Piranda. Application of model updating techniques in dynamics for the identification of elastic constants of composite materials. *Composites B*, 1999, 30, 79-85.
- 4.5 K. Balasubramaniam and N. S. Rao. Inversion of composite material elastic constants from ultrasonic bulk wave phase velocity data using genetic algorithms. *Composites B*, 1998, 29B, 171-180.
- 4.6 G. R. Lui, W. B. Ma and X. Han. An inverse procedure for determination of material constants of composite laminates using elastic waves. *Computer Methods in Applied Mechanics and Engineering*, 2002, 191, 3543-3554.
- 4.7 G. R. Lui, K. Y. Lam and X. Han. Determination of elastic constants of anisotropic laminated plates using elastic waves and a progressive neural network. *Journal of Sound and Vibration*, 2002, 252, 239-259.
- 4.8 A. L. Araujo, C. M. M. Soares, J. Herskovits and P. Pedersen. Parameter estimation in active plate structures using gradient optimisation and neural networks. *Inverse Problems in Science and Engineering*, 2006, 14(5), 483-493.
- 4.9 A. L. Araujo, H. M. R. Lopes, M. A. P. Vaz, C. M. M Soares, J. Herskovits and P. Pedersen. Parameter estimation in active plate structures. *Computers and Structures*, 2006, 84, 1471-1479.
- 4.10 T. Banks, R. C. Smith and Y. Wang. Smart Material Structures – Modelling, Estimation and Control, Masson: Paris, 1996.
- 4.11 H. T. Banks, R. C. Smith, D. E. Brown and V. L. Metcalf. The estimation of material and patch parameters in a PDE-based circular plate model. *Journal of Sound and Vibration*, 1997, 777-799.

- 4.12 C. M. M. Soares, M. J. M. Freitas, A. L. Araujo and P. Pedersen. Identification of material properties of composite plate specimens. *Composite Structures*, 1993, 25, 277-285.
- 4.13 A. L. Araujo, C. M. M. Soares and M. J. M. Freitas. Characterization of material parameters of composite plate specimens using optimisation and experimental vibrational data. *Composites B*, 1996, 27B, 185-191.
- 4.14 A. L. Araujo, C. M. M. Soares, M. J. M. Freitas, P. Pedersen and J. Herskovits. Combined numerical–experimental model for the identification of mechanical properties of laminated structures. *Composite Structures*, 2000, 50, 363-372.
- 4.15 J. S. Moita, C. M. M. Soares and C. A. M. Soares. Buckling and dynamic behaviour of laminated composite structures using a discrete higher order displacement model. *Computers and Structures*, 1999, 73, 407-423.
- 4.16 J. A. Mitchell and J. N. Reddy. A refined hybrid plate theory for composite laminates with piezoelectric lamina. *International Journal of Solids and Structures*, 1995, 32, 2345-2367.
- 4.17 J. N. Reddy. On laminated composite plates with integrated sensors and actuators. *Engineering Structures*, 1999, 21, 568-593.
- 4.18 O. C. Zienkiewicz. *The Finite Element Method in Engineering Science*, McGraw Hill: New York, 1971.
- 4.19 J. Herskovits. A feasible directions interior point technique for non-linear optimisation. *Journal of Optimisation Theory and Applications*, 1998, 99, 121-146.
- 4.20 J. Herskovits, V. Dubeux, C. M. M. Soares and A. L. Araujo. Interior point algorithms for non-linear least squares problems. *Inverse Problems in Science and Engineering*, 2004, 12, 211-223.
- 4.21 ANSI/IEEE Std 176-1987, IEEE standard on piezoelectricity, New York: Institute of Electrical and Electronics Engineers, 1998.
- 4.22 ASTM D150-98, Standard test methods for AC loss characteristics and permittivity (dielectric constant) of solid electrical insulation, American Society for Testing and Materials, 1998.
- 4.23 ANSYS 9.0 Reference Manual, ANSYS Inc., 2004.
- 4.24 ME'scope Version 4.0 Operating Manual, Vibrant Technology Inc., 1997.
- 4.25 M. R. Maheri and R. D. Adams. Modal vibration damping of anisotropic FRP laminates using the Rayleigh-Ritz energy minimization scheme. *Journal of Sound and Vibration*, 2003, 259(1), 17-29.
- 4.26 M. R. Maheri and R. D. Adams. Finite-element prediction of modal response of damped layered composite panels. *Composites Science and Technology*, 1995, 55, 13-23.
- 4.27 T. Saito, R. D. Parbery, S. Okuno and S. Kawano. Parameter identification for aluminum honeycomb sandwich panels based on orthotropic Timoshenko beam theory. *Journal of Sound and Vibration*, 1997, 208(2), 271-287.
- 4.28 T. Lekszycki, N. Olhoff and J. J. Pedersen. Modelling and identification of viscoelastic properties of vibrating sandwich beams. *Composite Structures*, 1992, 22, 15-31.

- 4.29 M. E. McIntyre and J. Woodhouse. On measuring the elastic and damping constants of orthotropic sheet materials. *Acta Metall*, 1988, 36(6), 1397-1416.
- 4.30 J. De Visscher, H. Sol, W. P. De Wilde and J. Vantomme. Identification of the damping properties of orthotropic composite materials using a mixed numerical experimental method. *Applied Composite Materials*, 1997, 4, 13-33.
- 4.31 G.-L. Qian, S. V. Hoa and X. Xiao. A vibration method for measuring mechanical properties of composite, theory and experiment. *Composite Structures*, 1997, 39(1-2), 31-38.
- 4.32 H. Sol, J. De Visscher and J. Vantomme. Measurement of complex moduli of composite materials and discussion of some results. - In: *Mechanical Identification of Composites* (Eds A. Vautrin and H. Sol), Elsevier Applied Science: London, New York, 1991, 16-29.
- 4.33 H. Sol, J. De Visscher and W. P. De Wilde. Identification of the viscoelastic material properties of orthotropic plates using a mixed numerical/experimental technique. - In: *Computational Methods and Experimental Measurements VI, Vol. 2: Stress Analysis* (Eds C. A. Brebbia and G. M. Carlomagno), Computational Mechanics Publications: Southampton, Boston, 1993, 131-142.
- 4.34 E. O. Ayorinde. Elastic constants of thick orthotropic composite plates. *Journal of Composite Materials*, 1995, 29, 1025-1035.
- 4.35 P. S. Frederiksen. Experimental procedure and results for the identification of elastic constants of thick orthotropic plates. *Journal of Composite Materials*, 1997, 31, 360-382.
- 4.36 R. F. S. Hearmon. *Introduction to Applied Anisotropic Elasticity*. Oxford Univ. Press, 1961.
- 4.37 B. Gommers, I. Verpoest and P. Van Houtte. Determination of the mechanical properties of composite materials by tensile tests. Part I: Elastic properties. *Journal of Composite Materials*, 1998, 32(4), 310-334.
- 4.38 D. R. Bland. *Theory of Linear Viscoelasticity*, Pergamon: London, 1960.
- 4.39 N. Distefano. On the identification problem in linear viscoelasticity. *ZAMM*, 1970, 50, 683-690.
- 4.40 N. Distefano and R. Todeschini. Modelling, identification and prediction of a class of nonlinear viscoelastic materials (I) and (II). *International Journal of Solids and Structures*, 1973, 9, 805-818, 1431-1438.
- 4.41 N. Distefano and R. Todeschini. On the identification of nonlinear viscoelastic characteristic of a class of polymeric materials. *ZAMM*, 1974, 54, 429-431.
- 4.42 L. Filipczynski, Z. Pawlowski and J. Wehr. *Ultrasonic Methods of Testing Materials*, Butterworths: London, 1966.
- 4.43 A. K. Mal, S.-S. Lih and Y. Bar-Cohen. Nondestructive characterization of the elastic constants of fiber reinforced composites. *AIAA*, 1993, 472-484.
- 4.44 Y. Okabe, N. Takeda and M. Sekiguchi. Macroscopic and microscopic elastic constant measurements of ceramic matrix composites using ultrasonic waves. *Journal of Composite Materials*, 1999, 33(18), 1743-1755.

- 4.45 S. Mistou and M. Karama. Determination of the elastic properties of composite materials by tensile testing and ultrasound measurement. *Journal of Composite Materials*, 2000, 34(20), 1696-1709.
- 4.46 Y. Chevalier. Experimental identification of complex stiffnesses of composite materials by ultrasonic wave propagation. - In: *Mechanical Identification of Composites* (Eds A. Vautrin and H. Sol), Elsevier Applied Science: London, New York, 1991, 67-74.
- 4.47 R. Rikards, A. Chate and E. Barkanov. Finite element analysis of damping the vibrations of laminated composites. *Computers & Structures*, 1993, 47, 1005-1015.
- 4.48 S. Vlachoutsis. Shear correction factors for plates and shells. *International Journal for Numerical Methods in Engineering*, 1992, 33, 1537-1552.
- 4.49 Y. M. Haddad. *Viscoelasticity of Engineering Materials*, Chapman & Hall: London, Glasgow, Weinheim, New York, Tokyo, Melbourne, Madras, 1995.
- 4.50 E. Barkanov, A. Chate, E. Skukis, O. Täger and H. Kolsters H. Finite element and experimental vibration analysis of viscoelastic composite structures. - In: *Computational Methods and Experimental Measurements XII* (Eds C. A. Brebbia and G. M. Carlomagno), WITpress: Southampton, Boston, 2005, 527-537.
- 4.51 P. S. Frederiksen. Numerical studies for the identification of elastic constants of thick orthotropic laminates. *European Journal of Mechanics, A-Solids*, 1997, 16, 117-140.
- 4.52 R. Rikards, A. Chate and G. Gailis. Identification of elastic properties of laminates based on experiment design. *International Journal of Solids and Structures*, 2001, 38, 5097-5115.
- 4.53 A. D. Nashif, D. I. G. Johnes and J. P. Henderson. *Vibration Damping*. John Wiley & Sons: New York, Chichester, Brisbane, Toronto, Singapore, 1985.